8. Ernst, V.: The digital pads of the tree frog, *Hyla cinerea*. 1. The epidermis. Tissue Cell **5**, 83–96 (1973)
9. Green, D.M.: Treefrog toe pads: comparative surface morphology using scanning electron microscopy. Can. J. Zool. **57**, 2033–2046 (1979)
10. Emerson, S.B., Diehl, D.: Toe pad morphology and mechanisms of sticking in frogs. Biol. J. Linn. Soc. **13**, 199–216 (1980)
11. Hanna, G., Barnes, W.J.P.: Adhesion and detachment of the toe pads of tree frogs. J. Exp. Biol. **155**, 103–125 (1991)
12. Smith, J.M., Barnes, W.J.P., Downie, J.R., Ruxton, G.D.: Structural correlates of increased adhesive efficiency with adult size in the toe pads of hylid tree frogs. J. Comp. Physiol. A **192**, 1193–1204 (2006)
13. Ghatak, A., Mahadevan, L., Chung, J.Y., Chaudhury, M.K., Shenoy, V.: Peeling from a biomimetically patterned thin elastic film. Proc. Roy. Soc. Lond. A **460**, 2725–2735 (2004)
14. Persson, B.N.J.: Wet adhesion with application to tree frog adhesive toe pads and tires. J. Phys. Cond. Matter **19**, 376110 (16 pp) (2007)
15. Scholz, I., Barnes, W.J.P., Smith, J.M., Baumgartner, W.: Ultrastructure and physical properties of an adhesive surface, the toe pad epithelium of the tree frog, *Litoria caerulea* White. J. Exp. Biol. **212**, 155–162 (2009)
16. Barnes, W.J.P., Perez Goodwyn, P., Nokhbatolfoghahai, M., Gorb, S.N.: Elastic modulus of tree frog adhesive toe pads. J. Comp. Physiol. A **197**, 969-978 (2011)
17. Samani, A., Zubovitz, J., Plewer, D.: Elastic moduli of normal and pathological human breast tissue: an inversion-technique-based investigation of 169 samples. Phys. Med. Biol. **52**, 1565–1576 (2007)
18. Vogel, S.: Comparative Biomechanics: Life's Physical World. Princeton University Press, Princeton (2003)
19. Perez Goodwyn, P., Peressadko, A., Schwarz, H., Kastne, V., Gorb, S.: Material structure, stiffness, and adhesion: why attachment pads of the grasshopper (*Tettigonia viridissima*) adhere more strongly than those of the locust (*Locusta migratoria*) (Insecta: Orthoptera). J. Comp. Physiol. A **192**, 1233–1243 (2006)
20. Barnes, W.J.P., Oines, C., Smith, J.M.: Whole animal measurements of shear and adhesive forces in adult tree frogs: insights into underlying mechanisms of adhesion obtained from studying the effects of size and scale. J. Comp. Physiol. A **192**, 1179–1191 (2006)
21. Smith, J.M., Barnes, W.J.P., Downie, J.R., Ruxton, G.D.: Adhesion and allometry from metamorphosis to maturation in hylid tree frogs – a sticky problem. J. Zool. **270**, 372–383 (2006)
22. Arzt, E., Gorb, S., Spolenak, R.: From micro to nano contacts in biological attachment devices. Proc. Natl. Acad. Sci. USA **100**, 10603–10606 (2003)
23. Autumn, K., Dittmore, A., Santos, D., Spenko, M., Cutkosky, M.: Frictional adhesion: a new angle on gecko attachment. J. Exp. Biol. **209**, 3569–3579 (2006)
24. Majumder, A., Ghatak, A., Sharmer, A.: Microfluidic adhesion induced by subsurface microstructures. Science **318**, 258–261 (2007)
25. Varenberg, M., Gorb, S.N.: Hexagonal surface micropattern for dry and wet friction. Adv. Mater. **21**, 483–486 (2009)
26. Varenberg, M., Gorb, S.N.: A beetle-inspired solution for underwater adhesion. J. R. Soc. Interface **5**, 383–385 (2008)
27. Barnes, W.J.P.: Tree frogs and tire technology. Tire Technol. Int. March 42–47 (1999)
28. Barnes, W.J.P., Smith, J., Oines, C., Mundl, R.: Bionics and wet grip. Tire Technol. Int. Dec. 56–60 (2002)
29. Vogel, M.J., Steen, P.H.: Capillary-based switchable adhesion, beetle inspired. Proc. Natl. Acad. Sci. USA **107**, 3377–3381 (2010)
30. Barnes, W.J.P., Pearman, J., Platter, J.: Application of peeling theory to tree frog adhesion, a biological system with biomimetic implications. Eur. Acad. Sci. E-Newsletter Sci. Technol. **1**(1), 1–2 (2008)

Adsorbate Adhesion

▶ Disjoining Pressure and Capillary Adhesion

Aerosol-Assisted Chemical Vapor Deposition (AACVD)

▶ Chemical Vapor Deposition (CVD)

AFM

▶ Robot-Based Automation on the Nanoscale

AFM Force Sensors

▶ AFM Probes

AFM in Liquids

Bart W. Hoogenboom
London Centre for Nanotechnology and Department of Physics and Astronomy, University College London, London, UK

Synonyms

Atomic force microscopy in liquids; Scanning force microscopy in liquids

Definition

Atomic force microscopy (AFM) in liquids is the application of AFM in liquid environment, i.e., in which both the surface under investigation and the scanning probe are immersed in liquid.

Overview and Definitions

AFM is a microscopy technique that can provide three-dimensional images of virtually any surface at nanometer-scale resolution. It relies on the force between a sharp probe and the surface, which is detected while scanning the probe over the sample. Unlike many other microscopy techniques at such a resolution, it can readily be applied in liquid environment.

An atomic force microscope consists of a sharp probe ("tip") mounted on a microfabricated cantilever beam and a mechanism ("scanner") to scan the tip over the surface at subnanometer resolution [1], see Fig. 1. Typically, an optical detection scheme is used to detect the deflection of the cantilever. Via the spring constant of the cantilever, the cantilever deflection can be translated to a force between tip and sample. For a rectangular lever, the spring constant is given by

$$k = \frac{Et^3 w}{4l^3}, \quad (1)$$

where E is the Young's modulus of the cantilever material (typically silicon or siliconnitride), and t, w, and l are its thickness, width, and length, respectively, which are in the micron range. Most cantilevers for AFM have spring constants between 0.01 and 100 N/m. In its most common mode of operation, the deflection of the cantilever (and thus the tip–sample force) is kept constant by adjusting the vertical position of the sample with respect to the tip.

In most instruments, the cantilever deflection is recorded via the position of a laser beam that is deflected from the cantilever. Images of the surfaces are acquired by line-by-line scanning the surface and tracing its surface contours on a false-color scale. For AFM in liquid, the surface and the cantilever are immersed in liquid. Typically, the minimum liquid volume is some tens of microliters, which can be either contained in a closed liquid cell, or in the shape of

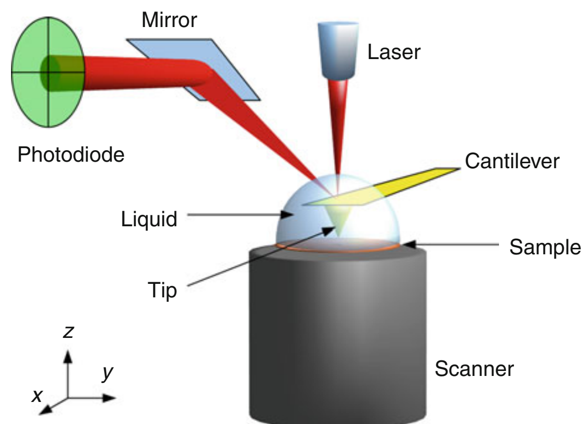

AFM in Liquids, Fig. 1 Schematic of AFM in liquid. A sharp tip is scanned across the sample surface while the tip–sample interaction is monitored via the deflection of the cantilever to which the tip is attached. The sample is mounted on a (usually piezoelectric) scanner for three-dimensional positioning with sub-nanometer accuracy. The sample, the tip, and the cantilever are immersed in liquid. The bending of the cantilever is usually detected via a laser beam deflected on a position-sensitive detector (4-quadrant photodiode)

a droplet that is formed by capillary forces between the sample surface and the cantilever holder. In principle, the liquid can be of arbitrary nature, though the optical deflection detection in most microscopes limit their use to liquids that are transparent for (near infra-) red light.

There are many possible imaging modes of AFM and their names are rather confusing. They are divided into static mode and a variety of dynamic modes in which the cantilever is oscillating [2]. The latter are of particular importance when the lateral (drag) forces on the sample need to be minimized, e.g., for imaging DNA molecules that are loosely bound to a flat surface. The most common modes of operation in liquid are static or contact mode and amplitude-modulation or tapping mode. In contact mode, the bending or deflection of the cantilever is used to detect the tip–sample force. In tapping mode, the cantilever is vertically oscillated above the sample, and the tip–sample interactions detected via the change (usually decrease) of amplitude of the cantilever oscillation. In variations along the same theme, the cantilever may be oscillated and tip–sample interactions are detected via changes in phase or resonance frequency of the cantilever [3]. An overview of the most relevant AFM modes in liquids is given in Table 1. Confusion may arise because the

AFM in Liquids, Table 1 Different modes of operation in AFM, with the parameter that is used to control the tip–sample distance while scanning over the surface

Mode of operation	Other common names	Control parameter
Static	Contact mode	Static deflection
Amplitude modulation (AM)	Tapping mode	Oscillation amplitude
	Intermittent contact AFM AC mode	
Frequency modulation (FM)	Non-contact (NC) AFM	Resonance frequency

commonly used terms contact, intermittent-contact, and non-contact often – but not always – refer to a mode of operation (as referred to in Table 1), and not necessarily to the actual contact (or lack of it) between the tip and the sample. As a particular example, FM ("non-contact") AFM in liquids is usually performed in the range of repulsive tip–sample interactions, with the tip in actual intermittent contact with the sample. In addition, if the amplitude is used to trace and control the tip–sample distance (i.e., tapping mode), the phase of the cantilever can be recorded simultaneously for phase imaging, which provides an additional means to measure tip–sample interactions. Or, in FM AFM, a frequency shift is used to trace elastic tip–sample interactions and control the tip–sample distance, while the oscillation amplitude can be kept constant by adjusting the cantilever drive signal. This cantilever drive signal then provides a simultaneous measure of the dissipative tip–sample interactions.

Physical and Chemical Principles

The spatial resolution of AFM critically depends on the sharpness of the tip and on the range of the tip–sample interactions. Ideally, only the very (nanometer-scale) end of the tip interacts with the surface, thus avoiding convolution effects due to interactions between the sample and the (micron-scale) bulk of the tip. The presence of long-range tip–sample forces is therefore decremental to the spatial resolution. On the other hand, the shorter the range of the tip–sample interaction, the more likely the tip is to enter in hard contact with the sample, which may damage the tip and/or the sample.

By immersing the tip and sample in liquid, it is not only possible to access scientifically and technologically interesting solid–liquid interfaces (including biological samples), but also to tune the tip–sample interactions by varying the ingredients of the liquid. In particular, the electrostatic sample interaction between the tip and a flat sample can be approximated by [4]:

$$F_{el} = g_\kappa \sigma_t \sigma_s e^{-\kappa z} + g_{2\kappa}\left(\sigma_t^2 + \sigma_s^2\right) e^{-2\kappa z}, \qquad (2)$$

where g_κ and $g_{2\kappa}$ are constants that depend on the tip geometry and the dielectric properties of the medium, σ_t and σ_s are the surface charges of the tip and the sample, respectively, z is the tip–sample distance, and κ^{-1} the Debye screening length [5],

$$\kappa^{-1} = \sqrt{\frac{\varepsilon_0 \varepsilon_b k_B T}{2e^2 I}}. \qquad (3)$$

In the latter, ε_0 is the permittivity of vacuum (8.854×10^{-23} F/m), ε_b the permittivity of the bulk solution (or the dielectric medium), k_B is the Boltzmann's constant (1.38×10^{-23} J/K), and T is the temperature in Kelvin. The parameter I is the ionic strength of the medium,

$$I = \frac{1}{2}\sum_i z_i^2 c_i. \qquad (4)$$

where z_i is the valence of ion i and c_i is its concentration. The Debye length is historically written as an inverse length (i.e., κ has units of m^{-1}). In typical biological buffers, the Debye length is between 1 and 10 nm.

In a chemically reactive medium, σ_t and σ_s are generally not zero. For typical tip terminations such as silicon oxide or silicon nitride in water, $\sigma_t < 0$ at neutral pH. As can be seen from Eq. 2, the strength of the electrostatic tip–sample interaction depends on σ_t and σ_s. These can be changed by adding or removing solutes that react with or bind to the tip and sample surfaces. In aqueous solutions, this is most readily achieved by changing the pH (i.e., adding H_3O^+ or OH^-). Moreover, the dielectric properties – and in particular the ionic strength (Eq. 4) – of the medium can be tuned to control the range of the electrostatic tip–sample interaction. This provides a significant advantage over AFM in gaseous mediums and vacuum environment, and is one of the reasons why the first true atomic resolution (see below) AFM images were

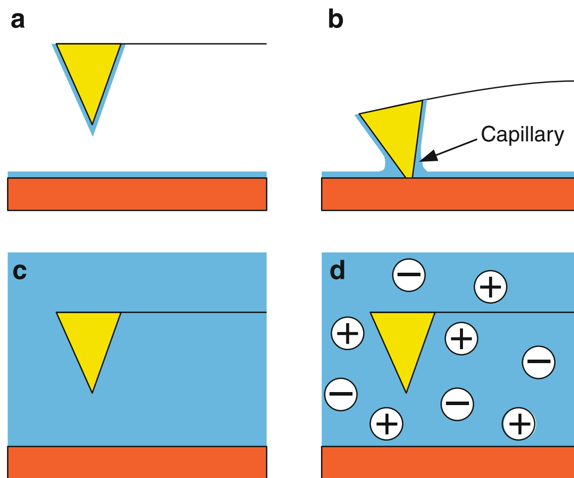

AFM in Liquids, Fig. 2 (**a**) Capillary forces for AFM in air arise due to the thin water layers that are usually present at both tip and sample under ambient conditions. (**b**) At small tip–sample distances, they pull the tip toward the surface to create a larger contact area and thus limit the lateral resolution. (**c**) In liquid environment, these capillary forces are absent. (**d**) Moreover, long-range electrostatic forces can be screened by ions in the liquid

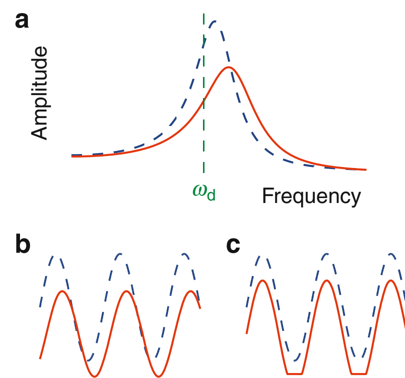

AFM in Liquids, Fig. 3 (**a**) Schematic resonance curve of a freely oscillating cantilever (*dashed, blue curve*), based on a model of a simple harmonic oscillator. In the presence of a (repulsive) elastic tip–sample force as well as dissipative tip–sample interactions, the resonance shifts to higher frequencies, broadens and decreases in amplitude (*red curve*). At a fixed driving frequency ω_d, such as in tapping mode, the effects of elastic or dissipative interactions will cause the amplitude to decrease or increase, depending on the choice of ω_d. (**b**) Sinusoidal oscillation of a cantilever above the surface (*dashed, blue*). Close to the sample, the oscillation amplitude decreases and changes phase (*red*). (**c**) For heavily damped cantilever oscillations ($Q \sim 1$), however, the harmonic-oscillator analysis is not valid any more. The tip–sample interaction will only affect the bottom part of the oscillation, where the tip is closest to the sample

obtained, in contact mode, in aqueous environment rather than in vacuum or air [6].

Compared to AFM in air, AFM in liquids has the additional advantage of preventing the capillary forces that arise from the humid coverage of both sample and tip under ambient conditions, as illustrated in Fig. 2. The capillary forces create a strong pull on the tip toward the sample at distances of many nanometers. On close approach, this results in a tip–sample contact area that covers many atoms at the surface, thus prohibiting high resolution. Under such conditions, AFM is likely to result in one of its most extensively documented artifacts: The apparent “atomic resolution” that results from the periodic interaction averaged over many atoms of tip and surface. This represents the atomic periodicity of the surface rather than individual atomic-scale features such as atomic defects (which are often used to demonstrate “true atomic resolution”).

Apart from electrostatic and capillary forces, AFM in liquids is also (and not exclusively) sensitive to atomic bonding forces and hard-core repulsion, van der Waals interactions, dissolution/solvation forces, and general dissipative interactions.

The latter are particularly important in the dynamic modes of AFM operation. To illustrate this, it is helpful to depict the cantilever resonance for different elastic and dissipative interactions, see Fig. 3.

A repulsive (elastic) tip–sample interaction increases the effective spring constant of the cantilever and thus increases its resonance frequency, shifting the whole resonance curve to the right. Any dissipative interaction reduces the sharpness of the resonance curve and the maximum of the curve. The quality factor Q is the most common measure for this sharpness, defined as $\omega_0/\Delta\omega$, where ω_0 is the natural frequency of the resonator and $\Delta\omega$ the width of the resonance curve at $1/\sqrt{2}\times$ its maximum amplitude. In tapping mode, the driving frequency is usually set just below the resonance frequency, such that both elastic and dissipative interactions cause the amplitude to decrease when the tip comes into contact with the sample. In FM AFM, the shift in the resonance frequency provides a direct measure of the elastic interaction, and the conversion to a force is straightforward when the amplitude of the oscillation is (kept) constant [7]. The dissipated energy can be deduced from the

energy that is required to maintain a fixed amplitude. Thus, tapping mode is sensitive to a mixture of elastic and dissipative tip–sample interactions, whereas FM AFM can track elastic and dissipative interactions separately (and simultaneously).

This analysis relies on the cantilever behaving as a simple harmonic oscillator, which is appropriate for $Q \gg 1$, typical for operation in vacuum ($Q \gtrsim 1000$) and air ($Q \gtrsim 100$). However, in liquid, viscous damping reduces Q to $\lesssim$ 10. In particular for softer cantilevers $k \lesssim 1\text{N/m}$, $Q \approx 1$, and the contact between tip and sample will prevent the cantilever from following a harmonic, sinusoidal oscillation. The cantilever oscillation will simply be topped off at the bottom of the oscillation, at the closest tip–sample approach. In this case, significant information on the tip–sample interaction will be contained in higher harmonics of the oscillation. The interpretation of cantilever oscillation in terms of tip–sample forces thus becomes considerably more complicated.

The low quality factor has another undesirable side effect for AFM operation that involves oscillating the cantilever. Cantilevers are usually driven by a small piezoelectric element that drives not only the cantilever itself, but also its (macroscopic) support chip and often the whole cantilever holder. In vacuum and air, the high Q singles out the cantilever resonance from other mechanical resonances in the instrument. In liquid, this is not the case any more, and a typical excitation spectrum contains a so-called forest of peaks, i.e., a convolution of the broad cantilever resonance with many sharp(er) mechanical resonances from the microscope, as illustrated in Fig. 4. Again, this complicates the interpretation of the cantilever behavior in terms of a simple harmonic oscillator. It also makes the choice of optimum driving frequency much less straightforward (usually, this is done by trial and error). Moreover, since this excitation spectrum depends on the macroscopic geometry of the fluid cell, it is much more dependent on drift than the cantilever alone. For these reasons, there are a number of alternative methods to only drive the microscopic cantilever (and no macroscopic parts), such as magnetic and optical actuation. In the former, the cantilever is coated with a magnetic material and driven by an AC magnetic field; in the latter, an AC-modulated actuation laser locally heats the metal-coated surface of cantilever, which acts as a bimetal and thus transduces laser power to cantilever deflection. These and other methods have the disadvantage of adding complexity to the instrument and eventually to the microfabricated cantilever itself.

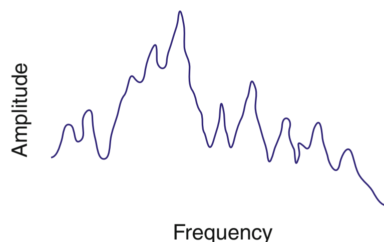

AFM in Liquids, Fig. 4 Excitation spectrum such as can be obtained for a cantilever in water that is actuated by piezoelectrically driving the cantilever holder rather than the cantilever alone. Note the contrast with the ideal resonance shape in Fig. 3a

These concerns can partly be addressed by so-called Q-control or self-oscillatory methods [8], in which the signal from the cantilever oscillation itself is phase-shifted, amplified, and added to the actuation signal. This positive feedback is very familiar in electronic oscillatory circuits. It causes any change to the oscillation to ring for a longer time, stretching its effect over many oscillations. As a result the effective Q of the cantilever oscillation is enhanced, and the cantilever is forced to follow a perfectly harmonic, sinusoidal oscillation. As for problems related to the forest of peaks in nonideal cantilever excitation, these are not resolved by Q control, since the positive feedback does not distinguish between the cantilever resonance and other mechanical resonances. Q control or self-oscillatory methods can be applied to each mode of operation (see Table 1), but for tapping mode has the side effect of slowing down the measurement: Changes in amplitude occur at a timescale of ~Q/ω_0, unlike changes in phase or resonance frequency, which are instantaneous. In FM AFM, the cantilever can even entirely be driven by its phase-shifted and amplified thermal noise.

Applications

AFM has been used to probe a vast amount of interfaces between (hard and soft) condensed matter and liquids. It is of particular importance for the study of surfaces that are instable or show distinctly different behavior when taken out of the liquid, and for the study

of dynamic processes that depend on an exchange of material (ions, macromolecules) between the surface and the liquid. AFM in liquids has been important for the study of, among others, crystal growth/dissolution, polymer science, and the behavior of liquids in confined geometries. The vast majority of its applications, however, lie in the life sciences [9]: For most biomolecular structures, aqueous solutions represent their natural environment. Their structures and functions are strongly dependent on the presence of water, a number of ions, and other macromolecules. The structure and function of biological samples can thus be studied at (sub)nanometer resolution while they are still "alive," and for varying liquid contents. The following represents some illustrative examples of the use of AFM in aqueous solutions on easily accessible samples, with a strong focus on biological applications.

Up to now, highest resolution AFM images in liquid have been obtained on atomically flat and inorganic surfaces, with calcite and muscovite mica as most common examples. On such surfaces, the lateral resolution can be less than an Ångström and the vertical resolution a few picometers. Though initially such resolution was only obtained in contact mode [6], more recently FM AFM has become popular as a method for atomic-resolution imaging that is significantly less susceptible to thermal drift. One of the key steps toward high-resolution imaging in liquids was the development of low-noise deflection sensors [10, 11]. This has brought the measurement noise down to the thermal noise of the cantilevers, even for stiff and heavily damped cantilevers in liquid. As a result, surfaces can now be stably measured with Ångström amplitudes of cantilever oscillation. This enhances the sensitivity to short-range forces and yields images such as depicted in Fig. 5. Because it is flat, hydrophilic, and easily cleaved, mica is one of the substrates of choice for adsorbing molecules in AFM experiments in aqueous solutions.

AFM has been successful in imaging DNA as well as DNA–protein complexes. DNA is routinely adsorbed on mica, where it is generally assumed to adopt a two-dimensional projection of its original three-dimensional configuration [13]. The rather flat geometry required for high-resolution AFM is a natural one for proteins that are embedded in a lipid membrane. In particular when two-dimensional crystals are available, such as for bacteriorhodopsin,

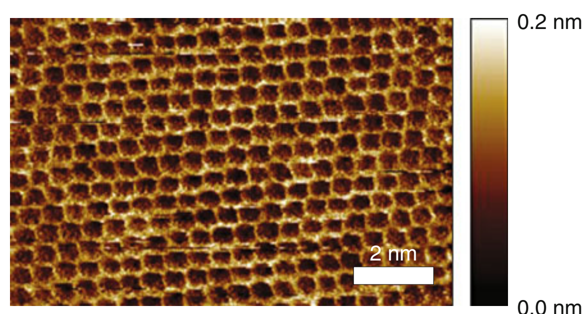

AFM in Liquids, Fig. 5 Atomic-resolution image of mica in (aqueous) buffer solution, obtained by FM AFM (Reproduced from [12], with permission)

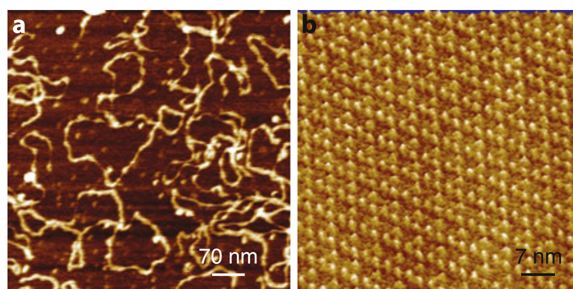

AFM in Liquids, Fig. 6 (**a**) Tapping-mode AFM image of DNA adsorbed on mica. Image courtesy Elliot Menter. (**b**) Two-dimensional crystal of the membrane protein bacteriorhodopsin, obtained by FM AFM on the extracellular side of the protein. Image courtesy Carl Leung

high-resolution images can readily be obtained in the various modes of AFM operation [14]. DNA and bacteriorhodopsin represent some of the most often imaged biomolecules by AFM in liquid (Fig. 6).

On a completely different scale, AFM can image objects as large as whole cells (Fig. 7). Due to thermal fluctuations, vibrations, and the overall softness of the cell, the spatial resolution is considerably lower than that obtained on flat surfaces or molecules directly adsorbed on a hard substrate. As, for cell imaging, alone, the advantage of AFM over optical techniques is therefore limited.

AFM can also be used to deliberately probe sample properties other than structure [15]. Single molecules that are tethered between the tip and the substrate can be deliberately stretched, unfolded, and allowed to refold at controlled load force [16], similar to optical-tweezers experiments. Using the same force

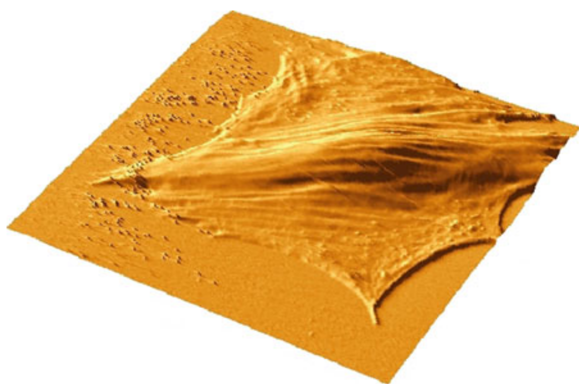

AFM in Liquids, Fig. 7 100 × 100 × 3 μm^3 contact-mode AFM topograph of an osteoblast (bone cell) adsorbed on a glass coverslip. Image courtesy Guillaume Charras

spectroscopy techniques, force–distance curves can be obtained on whole cells, yielding information about their local elasticity, or – when using chemically modified tips – local binding sites for specific ligands [17].

Finally, fast AFM methods [18] have improved the image rate from the typical frame per minute up to many frames per second. This gives direct access to the kinetics of molecular-scale processes at nanometer resolution.

Cross-References

- ▶ AFM
- ▶ AFM Probes
- ▶ AFM, Non-Contact Mode
- ▶ AFM, Tapping Mode
- ▶ Atomic Force Microscopy
- ▶ Force Modulation in Atomic Force Microscopy
- ▶ Friction Force Microscopy
- ▶ Imaging Human Body Down to Molecular Level
- ▶ Kelvin Probe Force Microscopy
- ▶ Magnetic Resonance Force Microscopy
- ▶ Mechanical Properties of Hierarchical Protein Materials
- ▶ Nanomedicine
- ▶ Nanotechnology
- ▶ Nanotribology
- ▶ Optical Tweezers
- ▶ Optomechanical Resonators
- ▶ Surface Forces Apparatus

References

1. Sarid, D.: Scanning Force Microscopy with Applications to Electric, Magnetic, and Atomic Forces, 2nd edn. Oxford University Press, Oxford (1994)
2. Garcia, R., Perez, R.: Dynamic atomic force microscopy methods. Surf. Sci. Rep. **47**, 197–301 (2002)
3. Giessibl, F.J.: Advances in atomic force microscopy. Rev. Mod. Phys. **75**, 949–983 (2003)
4. Butt, H.-J.: Electrostatic interaction in atomic force microscopy. Biophys. J. **60**, 777–785 (1991)
5. Israelachvili, J.N.: Intramolecular and Surface Forces, 3rd edn. Academic, Oxford (2011)
6. Ohnesorge, F., Binnig, G.: True atomic resolution by atomic force microscopy through repulsive and attractive forces. Science **260**, 1451–1456 (1993)
7. Sader, J.E., Jarvis, S.P.: Accurate formulas for interaction force and energy in frequency modulation force spectroscopy. Appl. Phys. Lett. **84**, 1801–1803 (2004)
8. Bhushan, B., Fuchs, H., Hosaka, S. (eds.): Applied Scanning Probe Methods, vol. I. Springer, Berlin/Heidelberg (2004)
9. Morris, V.J., Gunnig, A.P., Kirby, A.R.: Atomic Force Microscopy for Biologists. World Scientific, River Edge (1999)
10. Hoogenboom, B.W., Frederix, P.L.T.M., Yang, J.L., Martin, S., Pellmont, Y., Steinacher, M., Zäch, S., Langenbach, E., Heimbeck, H.-J., Engel, A., Hug, H.J.: A Fabry-Perot interferometer for micrometer-sized cantilevers. Appl. Phys. Lett. **86**, 074101 (2005)
11. Fukuma, T., Kimura, M., Kobayashi, K., Matsushige, K., Yamada, H.: Development of low noise cantilever deflection sensor for multienvironment frequency-modulation atomic force microscopy. Rev. Sci. Instrum. **76**, 053704 (2005)
12. Khan, Z., Leung, C., Tahir, B., Hoogenboom, B.W.: Digitally tunable, wide-band amplitude, phase, and frequency detection for atomic-resolution scanning force microscopy. Rev. Sci. Instrum. **81**, 073704 (2010)
13. Hansma, H.G.: Surface biology of DNA by atomic force microscopy. Annu. Rev. Phys. Chem. **52**, 71–92 (2001)
14. Müller, D.J., Engel, A.: Atomic force microscopy and spectroscopy of native membrane proteins. Nat. Protoc. **2**, 2191–2197 (2007)
15. Müller, D.J., Dufrêne, Y.F.: Atomic force microscopy as a multifunctional molecular toolbox in nanobiotechnology. Nat. Nanotechnol. **5**, 261–269 (2008)
16. Fisher, T.E., Marszalek, P.E., Fernandez, J.M.: Stretching single molecules into novel conformations using the atomic force microscope. Nat. Struct. Biol. **7**, 719–724 (2000)
17. Hinterdorfer, P., Dufrêne, Y.F.: Detection and localization of single molecular recognition events using atomic force microscopy. Nat. Method **3**, 347–355 (2006)
18. Yamamoto, D., Uchihashi, T., Kodera, N., Yamashita, H., Nishikori, S., Ogura, T., Shibata, M., Ando, T.: High-speed atomic force microscopy techniques for observing dynamic biomolecular processes. In: Walter, N.G. (ed.) Methods in Enzymology, vol. 475, pp. 541–564. Academic, Burlington (2010)

AFM Probes

Kenji Fukuzawa
Department of Micro System Engineering, Nagoya University, Nagoya, Chikusa-ku, Japan

Synonyms

AFM force sensors; AFM tips

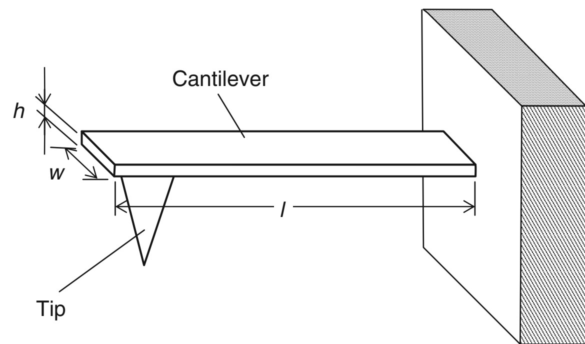

AFM Probes, Fig. 1 Schematic of a microcantilever probe

Definition

AFM probes are transducers that convert the interaction force with a sample surface into a deformation or a change of the vibrational state of the probe. Most probes consist of a sharp microtip and a force transducer. The former determines the lateral resolution of the AFM and the latter provides the force sensitivity.

Overview

A typical AFM probe consists of a sharp tip and a microcantilever, which plays the role of a force transducer. In this case, the interaction force between the tip and sample deflects the cantilever. The deflection can be detected by a displacement measurement method, such as an optical lever or interference techniques. Assuming that the deflection and the spring constant of the cantilever are Δz and k, respectively, the interaction force F is given by

$$F = k\Delta z. \tag{1}$$

In contact AFM mode, the probe height is controlled so that the probe deflection is constant, which means that the interaction force does not change during the probe scanning. Mapping the controlled height can thus provide the topography of the sample.

In the early days, a metal foil with a glued microparticle or sharpened metal wire was used as an AFM probe. Here, the particle or wire acted as a tip [1]. Improving the force sensitivity and reproducibility was not easy with those probes. Then, microfabricated cantilever probes were introduced [2]. These probes are made of silicon nitride or silicon and are produced by microfabrication techniques such as anisotropic chemical etching. Microfabricated probes enabled to improve the force sensitivity and expand the freedom of the probe design. They were also suitable for mass production. Therefore, microfabricated probes are the most common at present and various types of them are commercially available nowadays. Undoubtedly, the microfabricated probes have been playing an important role in AFM's becoming one of the most widely used methods in nanotechnology.

Probe Design

Since the specifications of the tip are rather limited by the fabrication method, the main part of the probe design is the force transducer, such as the rectangular micro cantilever sketched in Fig. 1. In addition to rectangular cantilevers, V-shaped cantilevers are widely used, especially in contact AFM mode. The force sensitivity of the probe should be high enough to detect weak interaction forces. From Eq. 1, the cantilever should convert a small force F into a large displacement Δz, which requires a small spring constant $k = F/\Delta z$. This means that higher sensitivity requires softer cantilevers. In addition to the force sensitivity, the robustness against mechanical disturbances from the environment should be considered. If the vibrations induced by the disturbances exceed the deflection due to the interaction force, the AFM signal is buried in the noise. The vibrations due to disturbances are amplified when the disturbance frequency is around the resonance frequency (natural frequency) of the probe. Since the disturbance frequencies are generally low, the resonance frequency

should be set at a high value, typically larger than about 10 kHz. If the force transducer of the probe is simplified as a point mass and spring system, the resonance frequency is given by

$$f_r = \frac{1}{2\pi}\sqrt{\frac{k}{m}}, \quad (2)$$

where m is the mass of the transducer. The sensitivity needs low values of k whereas the robustness against the environmental disturbances requires high values of f_r. This means that low values of m are required. Therefore, the force transducer of the probe should be soft and small. If a rectangle cantilever is chosen as a force transducer, it has to be thin and small. Microfabricated cantilevers meet this demand and, for this reason, they became standard probes for AFM.

The design details of a rectangular cantilever are considered below. If the length, width, and thickness of the cantilever are l, w, and h, respectively, the spring constant k is given by

$$k = \frac{Ewh^3}{4l^3}, \quad (3)$$

where E is the Young's modulus of the cantilever. It should be noted that the spring constant is proportional to $(h/l)^3$. This means that longer and thinner cantilevers can provide higher force sensitivity. The force F to be measured depends on the interaction between the tip and sample and the deflection Δz depends on the sensitivity of the displacement measurement method. Therefore, the spring constant k should be determined by considering the typical values of F and Δz for the targeted samples and the measurement system. On the other hand, the resonance frequency of a rectangular cantilever is given by

$$f_r = \frac{\lambda^2}{4\pi}\frac{h}{l^2}\sqrt{\frac{E}{3\rho}}, \quad (4)$$

where ρ is the density of the cantilever and λ is a constant that depends on the vibrational mode. For the first mode λ is about 1.875. It should be noted that the cantilever width is not included in Eq. 4. Since f_r is proportional to h/l^2, higher resonance frequencies f_r require shorter and thicker cantilevers. However, as described above, high sensitivity requires

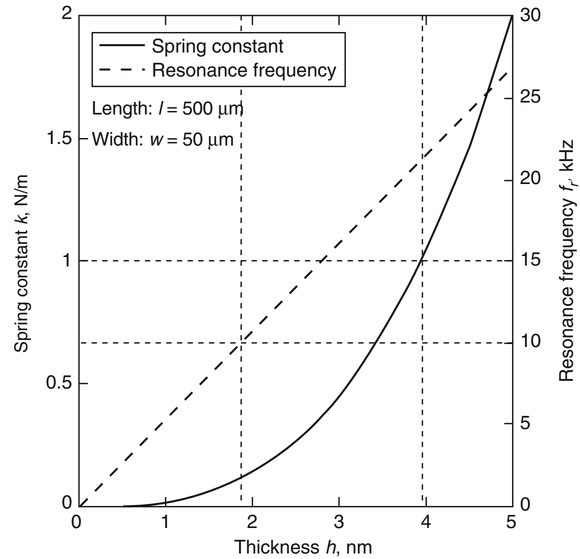

AFM Probes, Fig. 2 Thickness dependencies of the spring constant and resonance frequency of a microcantilever

opposite conditions. Thus, a balance between the spring constant and the resonance frequency has to be found in designing the probe. An example for contact mode cantilevers is shown in Fig. 2, where the thickness dependencies of the spring constant and resonance frequency are plotted using Eqs. 3 and 4 for a length $l = 500$ μm and a width $w = 50$ μm, respectively. If a spring constant of less than 1 N/m and a resonance frequency larger than 10 kHz are selected, the former curve requires a thickness of more than 1.9 μm and the latter curve requires a thickness of less than 4.0 μm. Therefore, a thickness in the overlapping range should be selected. A probe with these dimensions is not easy to fabricate by conventional machining and requires micromachining techniques.

Measurements of the spring constant k and resonance frequency f_r are important for converting the measured deflection signal into a force signal. The resonance frequency f_r can be measured by varying the drive frequency as it is routinely done in commercial AFM equipments. However, the accurate measurement of the spring constant k is not easy. An approximate value can be calculated from the dimensions of the cantilever using Eq. 3. An experimental method using the thermal fluctuation was presented in Ref. [3].

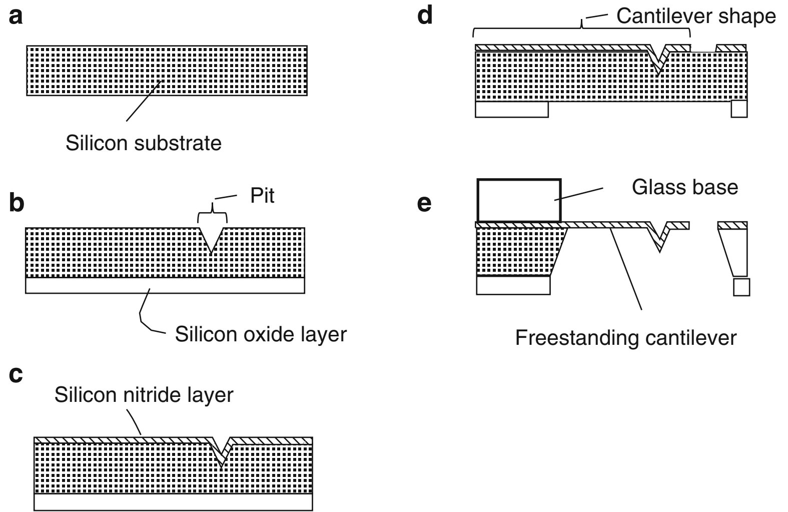

AFM Probes, Fig. 3 Fabrication process of a microfabricated probe: (**a**) silicon substrate, (**b**) formation of pit for a microtip, (**c**) deposition of silicon nitride layer, (**d**) patterning of cantilever, and (**e**) removal of substrate

Many types of AFMs using a vibrating cantilever have been developed, such as cyclic contact mode and non-contact mode AFMs. The probe vibrations can be induced using a quartz-oscillator. In this case, the resonance properties, especially the quality factor Q, are very important. The quality factor Q is defined as $Q = 1/2\zeta$, where ζ is the damping coefficient. A probe with a high Q is able to resonate effectively and its vibration is hard to damp. The minimum detectable force gradient in the frequency-modulation detection, which is widely used in highly sensitive AFMs such as non-contact AFMs and magnetic force microscopy, is given by

$$\left(\frac{\partial F}{\partial z}\right)_{\min} = \frac{2}{A}\sqrt{\frac{kk_{\mathrm{B}}TB}{\omega_{\mathrm{r}}Q}}, \tag{5}$$

where B, ω_{r}, and A are the measurement band width, resonance angular frequency, and vibration amplitude, respectively [4]. Higher force sensitivity requires a higher Q. Since the vibration damping of the probe is caused by the internal friction and by friction between the probe and environmental gas such as air, the quality factor Q usually depends on the probe structure and environment. Typical values of Q of silicon cantilevers are on the order of 10–100 in air whereas they can increase up to more than 10,000 in vacuum. A method to increase Q electronically was presented, where the deflection signal is fed back to the drive signal after the phase of the deflection signal is shifted by 90° [5].

Probe Fabrication

At present, most of the probes are fabricated by microfabrication techniques and various types of probes have been designed. Moreover, a considerable number of them are commercially available because microfabricated probes are suitable for mass production. The fabrication methods have also been improved, corresponding to a general improvement of the probe quality. Here, the fabrication methods for two typical types of probes are outlined. We will first address the probes made of silicon nitride. These probes are widely used in contact AFM mode. The fabrication process is shown in Fig. 3 [6]. In this method, a small pit that is formed in a silicon substrate by anisotropic wet etching is used as a mold. The silicon oxide layer is formed as an etching mask for the later substrate removal (Figs. 3a and b). A silicon nitride film is deposited onto the substrate and the cantilever is patterned by lithography. At this point, the cantilever with tip is shaped (Figs. 3c and d). By attachment of the glass base by anodic bonding and removal of the silicon substrate by wet etching,

a freestanding cantilever is obtained (Fig. 3e). Another type of probes are silicon cantilevers [7]. Silicon cantilevers are the most widely used probes in AFM and they are operated in various modes. By using the undercut etching of the underneath of a circular mask, a tip is formed. Then the cantilever is patterned. The substrate silicon is removed by wet etching with protection of the fabricated tip and cantilever. Sharpening the tip end can be achieved by thermal oxidation followed by oxide removal [6].

Future Directions for Research

In addition to standard silicon or silicon nitride cantilever probes, various types of probes have been recently introduced. In a piezoresistive probe a piezoresistive strain sensor is embedded with a silicon cantilever [8]. The embedded sensor detects the cantilever deflection and makes the detection system such as an optical lever unnecessary. This not only makes the setup compact but also provides easier operation in the special case of liquid or vacuum environments. Along the growth of microfabricated cantilever probes, probes that use a quartz-oscillator as a force transducer have also been developed. Various types of oscillators such as tuning fork or linear-extension resonators are used [9]. In many probes, a microtip is manually glued to the quartz-oscillator although the oscillator is microfabricated. Quartz-oscillator probes have advantages of high Q and large spring constant. The latter allows to avoid the jump-in of the probe. In addition, quartz-oscillator probes provide self-sensing as piezoresistive probes.

As stated above, the improvement of the probes is essential for the development of AFM. Recent advances in micro/nanomachining are promoting this improvement, which is expected to open up new applications of AFM.

Cross-References

- ▶ Atomic Force Microscopy
- ▶ Friction Force Microscopy
- ▶ MEMS
- ▶ Micromachining
- ▶ NEMS
- ▶ Scanning Probe Microscopy

References

1. Binnig, C., Quate, C.F., Gerber, Ch: Atomic force microscope. Phys. Rev. Lett. **56**(9), 930–933 (1986)
2. Binnig, G., Gerber, C., Stoll, E., Albrecht, T.R., Quate, C.F.: Atomic resolution with atomic force microscope. Europhys. Lett. **3**(12), 1281–1286 (1987)
3. Hutter, J.L., Bechhoefer, J.: Calibration of atomic-force microscope tips. Rev. Sci. Instrum. **64**(7), 1868–1873 (1993)
4. Albrecht, T.R., Grutter, P., Horne, D., Rugar, D.: Frequency modulation detection using high-Q cantilevers for enhanced force microscope sensitivity. J. Appl. Phys. **69**(2), 668–673 (1991)
5. Anczykowski, B., Cleveland, J.P., Krüger, D., Elings, V., Fuchs, H.: Analysis of the interaction mechanisms in dynamic mode SFM by means of experimental data and computer simulation. Appl. Phys. **A66**, S885–S889 (1998)
6. Albrecht, T.R., Akamine, S., Carver, T.E., Quate, C.F.: Microfabrication of cantilever styli for the atomic force microscope. J. Vac. Sci. Technol. **A8**, 3386–3396 (1990)
7. Wolter, O., Bayer, Th, Greschner, J.: Micromachined silicon sensors for scanning force microscopy. J. Vac. Sci. Technol. **B9**, 1353–1357 (1991)
8. Tortonese, M., Barrett, R.C., Quate, C.F.: Atomic resolution with an atomic force microscope using piezoresistive detection. Appl. Phys. Lett. **62**(8), 834–836 (1993)
9. Giessibl, F.J.: Atomic resolution on Si(111)-(7 × 7) by noncontact atomic force microscopy with a force sensor based on a quartz tuning fork. Appl. Phys. Lett. **76**(11), 1470–1472 (2000)

AFM Tips

▶ AFM Probes

AFM, Non-contact Mode

Hendrik Hölscher
Karlsruher Institut für Technologie (KIT), Institut für Mikrostrukturtechnik, Karlsruhe, Germany

Definition

The *noncontact atomic force microscopy* (NC-AFM) is a specific AFM technique primarily developed for

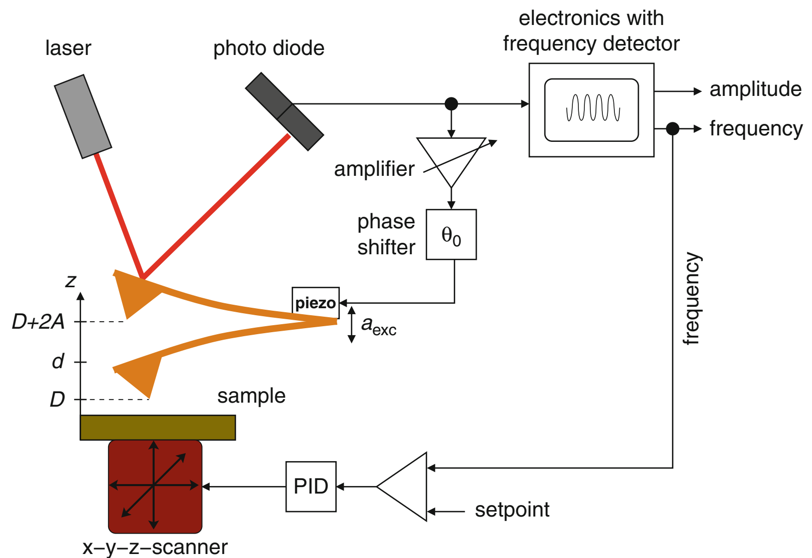

AFM, Non-contact Mode, Fig. 1 The schematic set-up of a dynamic force microscope based on the frequency modulation technique often used in UHV. A significant feature is the positive feedback of the self-driven cantilever. The detector signal is amplified and phase shifted before it is used to drive the piezo. The measured quantity is the frequency shift due to the tip-sample interaction, which serves as the feedback signal for the cantilever-sample distance

application in vacuum where standard AFM cantilevers made from silicon or silicon nitride exhibit very high quality factors Q, what makes the response of the system slow if driven in AM or tapping mode (▶ AFM, Tapping Mode). The technique to oscillate the cantilever also in high Q environments is called *frequency-modulation* (FM) mode. In contrast to the tapping or AM mode typically applied in air or liquids, this approach features a so-called self-driven oscillator, which uses the cantilever deflection itself as drive signal, thus ensuring that the cantilever instantaneously adapts to changes in the resonance frequency. The NC-AFM technique is the method of choice to obtain true atomic resolution on non-conduction surfaces with an atomic force microscope.

Overview

To obtain high resolution images with an atomic force microscope it is most important to prepare clean sample surfaces free from unwanted adsorbates. Therefore, these experiments are usually performed in ultra-high vacuum with pressures below 1×10^{-10} mbar. As a consequence most dynamic force microscope experiments in vacuum utilize the so-called *frequency modulation* (FM) detection scheme introduced by Albrecht et al. [1]. In this mode the cantilever is self-oscillated, in contrast to the AM- or tapping-mode (▶ AFM, Tapping Mode). The FM-technique enables the imaging of single point defects on clean sample surfaces in vacuum and its resolution is comparable with the scanning tunneling microscope, while not restricted to conducting surfaces [2–6]. In the years after the invention of the FM-technique the term *non-contact atomic force microscopy* (NC-AFM) was established, because it is commonly believed that a repulsive, destructive contact between tip and sample is prevented by this technique.

Set-Up of FM-AFM

In vacuum applications, the Q-factor of silicon cantilevers is in the range of 10,000–30 000. High Q-factors, however, limit the acquisition time (bandwidth) of a dynamic force microscopy, since the oscillation amplitude of the cantilever needs a long time to adjust. This problem is avoided by the FM-detection scheme based on the specific features of a self-driven oscillator.

The basic set-up of a dynamic force microscope utilizing this driving mechanism is schematically shown in Fig. 1. The movement of microfabricated cantilevers is typically measured with the laser beam deflection method or an interferometer. A self-detecting sensor like a tuning fork do not need an additional detection sensor. In any case the amplitude signal fed back into an amplifier with an *automatic gain control* (AGC) and is subsequently used to excite the piezo oscillating the cantilever. The time delay between the excitation signal and cantilever deflection

is adjusted by a time ("phase") shifter to a value of ≈ 90°, since this ensures an oscillation at resonance. Two different modes have been established: The *constant amplitude*-mode [1], where the oscillation amplitude A is kept at a constant value by the AGC, and the *constant excitation mode* [7], where the excitation amplitude is kept constant. In the following, however, only the constant amplitude mode is discussed.

The key feature of the described set-up is the positive feedback-loop which oscillates the cantilever always at its resonance frequency f [8]. The reason for this behavior is that the cantilever serves as the frequency determining element. This is in contrast to an external driving of the cantilever in tapping mode by a frequency generator (▶ AFM, Tapping Mode). If the cantilever oscillates near the sample surface, the tip-sample interaction alters its resonant frequency, which is then different from the eigenfrequency f_0 of the free cantilever. The actual value of the resonant frequency depends on the nearest tip-sample distance and the oscillation amplitude. The measured quantity is the *frequency shift* Δf, which is defined as the difference between both frequencies ($\Delta f := f - f_0$). For imaging the frequency shift Δf is used to control the cantilever sample distance. Thus, the frequency shift is constant and the acquired data represents planes of constant Δf, which can be related to the surface topography in many cases.

Origin of the Frequency Shift

Before presenting experimental results obtained in vacuum the origin of the frequency shift is analyzed in mode detail. A good insight into the cantilever dynamics is given by looking at the tip potential displayed in Fig. 2. If the cantilever is far away from the sample surface, the tip moves in a symmetric parabolic potential (dotted line), and its oscillation is harmonic. In such a case, the tip motion is sinusoidal and the resonance frequency is given by the eigenfrequency f_0 of the cantilever. If, however, the cantilever approaches the sample surface, the potential – which determines the tip oscillation – is modified to an effective potential V_{eff} (solid line) given by the sum of the parabolic potential and the tip-sample interaction potential V_{ts} (dashed line). This effective potential differs from the original parabolic potential and shows an asymmetric shape.

As a result of this modification of the tip potential the oscillation becomes anharmonic, and the resonance frequency of the cantilever depends now on the oscillation amplitude A. Since the effective potential experienced by the tip changes also with the nearest distance D, the frequency shift is a functional of both parameters ($\Rightarrow \Delta f := \Delta f(D, A)$).

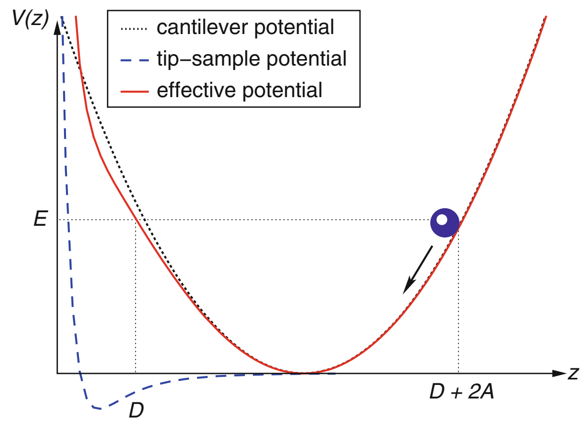

AFM, Non-contact Mode, Fig. 2 The frequency shift in dynamic force microscopy is caused by the tip-sample interaction potential (*dashed line*), which alters the harmonic cantilever potential (*dotted line*). Therefore, the tip moves in an anharmonic and asymmetric effective potential (*solid line*)

Figure 3 displays some experimental frequency shift versus distance curves for different oscillation amplitudes [9]. The obtained experimental frequency shift vs. distance curves show a behavior expected from the simple model explained above. All curves show a similar overall shape, but differ in magnitude in dependence of the oscillation amplitude and the nearest tip-sample distance. During the approach of the cantilever towards the sample surface, the frequency shift decreases and reaches a minimum. With a further reduction of the nearest tip-sample distance, the frequency shift increases again and becomes positive. For smaller oscillation amplitudes, the minimum of the $\Delta f(z)$-curves is deeper and the slope after the minimum is steeper than for larger amplitudes, i.e., the overall effect is larger for smaller amplitudes.

This can be explained by the simple potential model as well: A decrease of the amplitude A for a fixed nearest distance D moves the minimum of the effective potential closer to the sample surface. Therefore, the relative perturbation of the harmonic cantilever potential increases, which increases also the absolute value of the frequency shift.

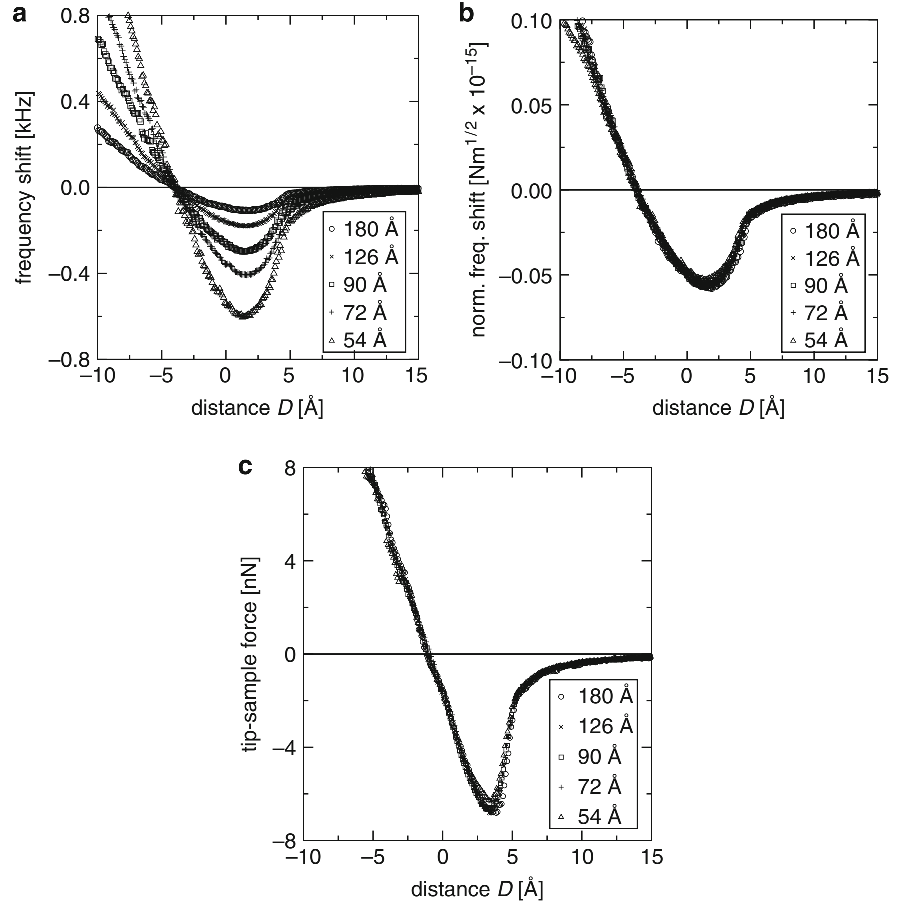

AFM, Non-contact Mode, Fig. 3 (**a**) Experimental frequency shift versus distance curves acquired with a silicon cantilever ($c_z = 38$ N/m; $f_0 = 171$ kHz) and a graphite sample for different amplitudes (54–180 Å) in UHV at low temperature ($T = 80$ K). (**b**) Transformation of all frequency shift curves shown in (**a**) to one universal curves using Eq. 6. The normalized frequency shift γ (D) is nearly identical for all amplitudes. (**c**) The tip-sample force calculated with the experimental data shown in (**a**) and (**b**) using the formula Eq. 7

Theory of FM-AFM

As already described in the previous subsection it is a specific feature of the FM-modulation technique that the cantilever is "self-driven" by a positive feedback loop. Due to this experimental set-up, the corresponding equation of motion is different from the case of the externally driven cantilever discussed for the tapping-mode. The external driving term has to be replaced in order to describe the self-driving mechanism correctly. Therefore, the equation of motion is given by

$$m\ddot{z}(t) + \frac{2\pi f_0 m}{Q}\dot{z}(t) + c_z(z(t) - d) + \underbrace{g c_z(z(t - t_0) - d)}_{driving} = F_{ts}[z(t), \dot{z}(t)]. \quad (1)$$

where $z := z(t)$ represents the position of the tip at the time t; c_z, m, and Q are the spring constant, the effective mass, and the quality factor of the cantilever, respectively. $F_{ts} = -(\partial V_{ts})/(\partial z)$ is the tip-sample interaction force. The last term on the left describes the active feedback of the system by the amplification of the displacement signal by the *gain factor* g measured at the retarded time $t - t_0$.

The frequency shift can be calculated from the above equation of motion with the ansatz

$$z(t) = d + A\cos(2\pi f t) \quad (2)$$

describing the stationary solutions of Eq. 1. Again, it is assumed that the cantilever oscillations are more or less sinusoidal and develop the tip-sample force F_{ts}

into a Fourier-series. As a result the following equation for the frequency shift is obtained

$$\Delta f = \frac{1}{\pi c_z A^2} \int_{d-A}^{d+A} (F_\downarrow + F_\uparrow) \frac{z-d}{\sqrt{A^2-(z-d)^2}} dz \quad (3)$$

and the energy dissipation

$$\Delta E = \left(g - \frac{1}{Q}\frac{f}{f_0} \right) \pi c_z A^2. \quad (4)$$

Since the amplitudes in FM-AFM are often considerably larger than the distance range of the tip-sample interaction, apply the "large amplitude approximation" [10, 11] can be applied. This yields the formula

$$\Delta f = \frac{1}{\sqrt{2}\pi} \frac{f_0}{c_z A^{3/2}} \int_D^{D+2A} \frac{F_{ts}(z)}{\sqrt{z-D}} dz \quad (5)$$

It is interesting to note that the integral in this equation is virtually independent of the oscillation amplitude. The experimental parameters (c_z, f_0, and A) appear as pre-factors. Consequently, it is possible to define the *normalized frequency shift* [10]

$$\gamma(z) := \frac{c_z A^{3/2}}{f_0} \Delta f(z) \quad (6)$$

This is a very useful quantity to compare experiments obtained with different amplitudes and cantilevers. The validity of Eq. 6 is nicely demonstrated by the application of this equation to the frequency shift curves already presented in Fig. 3a. As shown in Fig. 3b all curves obtained for different amplitudes result into one universal γ-curve, which depends only on the actual tip-sample distance D.

These equations help to calculate the frequency shift for a given tip-sample interaction law. The inverse problem, however, is even more interesting: *How can the tip-sample interaction be determined from frequency shift data?* Several solutions to this question have been presented by various authors and have lead to the *dynamic force spectroscopy* (DFS) technique, which is a direct extension of the FM-AFM mode [12].

Here the approach of Dürig [11] is presented, which is based on the inversion of the integral Eq. 5. It can be transformed to

$$F_{ts}(D) = \sqrt{2} \frac{c_z A^{3/2}}{f_0} \frac{\partial}{\partial D} \int_D^{\infty} \frac{\Delta f(z)}{\sqrt{z-D}} dz, \quad (7)$$

which allows a direct calculation of the tip-sample interaction force from the frequency shift versus distance curves.

An application of this formula to the experimental frequency shift curves already presented in Fig. 3a is shown in Fig. 3c. The obtained force curves are nearly identical although obtained with different oscillation amplitudes. Since the tip-sample interactions can be measured with high resolution, dynamic force spectroscopy opens a direct way to compare experiments with theoretical models and predictions.

Applications of FM-AFM

The excitement about the NC-AFM technique in ultrahigh vacuum was driven by the first results of Giessibl [13] who achieved to image the true atomic structure of the Si(111)-7 × 7-surface with this technique in 1995. In the same year Sugawara et al. [14] observed the motion of single atomic defects on InP with true atomic resolution. However, imaging on conducting or semi-conducting surfaces is also possible with the scanning tunneling microscope (STM) and these first NC-AFM images provided no new information on surface properties. The true potential of NC-AFM lies in the imaging of non-conducting surface with atomic precision. A long-standing question about the surface reconstruction of the technological relevant material Aluminium oxide could be answered by Barth et al. [15], who imaged the atomic structure of the high temperature phase of α-Al_2O_3(0001).

The high resolution capabilities of non-contact atomic force microscopy are nicely demonstrated by the images shown in Fig. 4. Allers et al. [16] resolved atomic steps and defects with atomic resolution on Nickel oxide. Today such a resolution is routinely obtained by various research groups (for an overview see, e.g., Refs. [2–6]). Recent efforts have also been concentrated on the analysis of functional organic molecules, since in the field of nanoelectronics it is anticipated that in particular organic molecules will

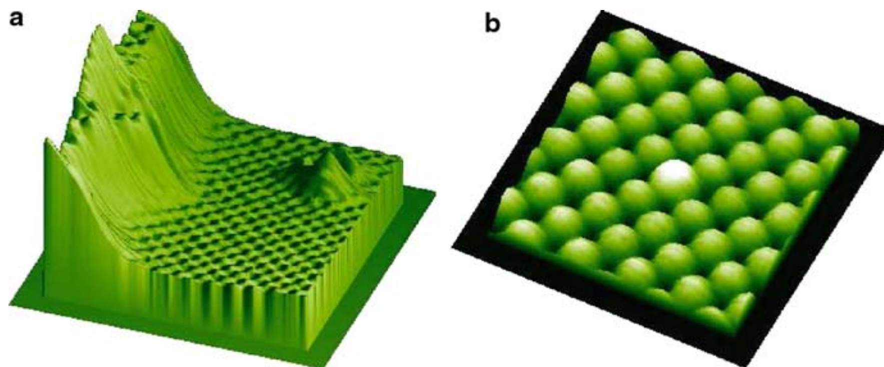

AFM, Non-contact Mode, Fig. 4 Imaging of a NiO(001) sample surface with a non-contact AFM. (**a**) Surface step and an atomic defect. The lateral distance between two atoms is 4.17 Å. (**b**) A dopant atom is imaged as a light protrusion about 0.1 Å higher as the other atoms (Images courtesy of W. Allers and S. Langkat, University of Hamburg; used with kind permission)

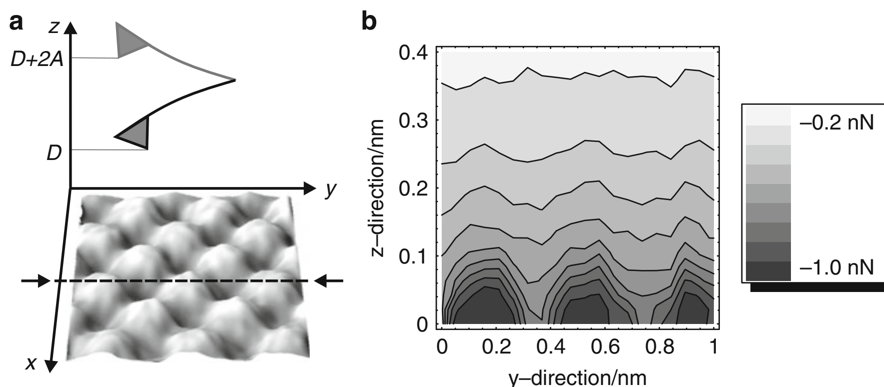

AFM, Non-contact Mode, Fig. 5 (**a**) Principle of 3D-force spectroscopy. The cantilever oscillates near the sample surface and measure the frequency shift in a x-y-z-box. The three dimensional surface shows the topography of the sample (image size: 10 Å × 10 Å) obtained immediately before the recording of the spectroscopy field. (**b**) The reconstructed force field of NiO(001) shows atomic resolution. The data is taken along the line shown in (**a**)

play an important role as the fundamental building blocks of nanoscale electronic device elements.

The concept of dynamic force spectroscopy can be also extended to 3D-force spectroscopy by mapping the complete force field above the sample surface [12]. Figure 5a shows a schematic of the measurement principle [17]. Frequency shift vs. distance curves are recorded on a matrix of points perpendicular to the sample surface. Using Eq. 7 the complete three-dimensional force field between tip and sample can be recovered with atomic resolution. Figure 5b shows a cut through the force field as a two-dimensional map.

If the NC-AFM is capable of measuring forces between single atoms with sub-nN precision, why should it not be possible to also exert forces with this technique? In fact, the new and exciting field of nanomanipulation would be driven to a whole new dimension, if defined forces can be reliably applied to single atoms or molecules. In this respect, Loppacher et al. [18] achieved to push on different parts of an isolated Cu-TBBP molecule, which is known to possess four rotatable legs. They measured the force-distance curves while one of the legs was pushed by the AFM tip and turned by 90°, thus being able to measure the energy which was dissipated during "switching" this molecule between different conformational states. The manipulation of single Sn-atoms with the NC-AFM was nicely demonstrated by Sugimoto et al. who manipulated single Sn-atoms on the Ge(111)-c(2 × 8) semiconductor surface (Fig. 6). By pushing single Sn-atoms from one lattice site to the other they finally succeeded to write the letter "Sn" with single atoms.

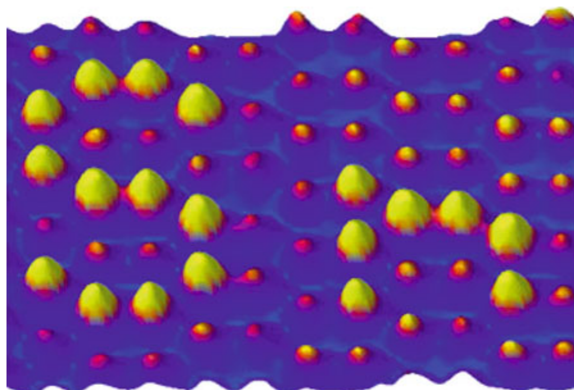

AFM, Non-contact Mode, Fig. 6 Final topographic NC-AFM image of the process of rearranging single Sn-atoms on a Ge (111)-c(2 × 8) semiconductor surface at room temperature (Reproduced from [19])

Cross-References

- ▶ AFM, Tapping mode
- ▶ Friction Force Microscopy
- ▶ Kelvin Probe Force Microscopy
- ▶ Magnetic Resonance Force Microscopy
- ▶ Piezoresponse Force Microscopy and Spectroscopy

References

1. Albrecht, T.R., Grütter, P., Horne, D., Rugar, D.: Frequency modulation detection using high-Q cantilevers for enhanced force microscope sensitivity. J. Appl. Phys. **69**, 668 (1991)
2. Morita, S., Wiesendanger, R., Meyer, E. (eds.): Noncontact Atomic Force Microscopy. Springer, Berlin (2002)
3. Garcia, R., Pérez, R.: Dynamic atomic force microscopy methods. Surf. Sci. Rep. **47**, 197 (2002)
4. Giessibl, F.-J.: Advances in atomic force microscopy. Rev. Mod. Phys. **75**, 949 (2003)
5. Meyer, E., Hug, H.J., Bennewitz, R.: Scanning Probe Microscopy - The Lab on a Tip. Springer, Berlin (2004)
6. Morita, S., Giessibl, F.J., Wiesendanger, R. (eds.): Noncontact Atomic Force Microscopy, vol. 2. Springer, Berlin (2009)
7. Ueyama, H., Sugawara, Y., Morita, S.: Stable operation mode for dynamic noncontact atomic force microscopy. Appl. Phys. A **66**, S295 (1998)
8. Hölscher, H., Gotsmann, B., Allers, W., Schwarz, U.D., Fuchs, H., Wiesendanger, R.: Comment on "Damping mechanism in dynamic force microscopy". Phys. Rev. Lett. **88**, 019601 (2002)
9. Hölscher, H., Schwarz, A., Allers, W., Schwarz, U.D., Wiesendanger, R.: Quantitative analysis of dynamic force spectroscopy data on graphite(0001) in the contact and non-contact regime. Phys. Rev. B **61**, 12678 (2000)
10. Giessibl, F.J.: Forces and frequency shifts in atomic-resolution dynamic-force microscopy. Phys. Rev. B **56**, 16010 (1997)
11. Dürig, U.: Relations between interaction force and frequency shift in large-amplitude dynamic force microscopy. Appl. Phys. Lett. **75**, 433 (1999)
12. Baykara, M.Z., Schwendemann, T.C., Altman, E.I., Schwarz, U.D.: Three-dimensional atomic force microscopy taking surface imaging to the next level. Adv. Mater. **22**, 2838 (2010)
13. Giessibl, F.-J.: Atomic resolution of the silicon (111)-(7 × 7) surface by atomic force microscopy. Science **267**, 68 (1995)
14. Sugawara, Y., Otha, M., Ueyama, H., Morita, S.: Defect motion on an InP(110) surface observed with noncontact atomic force microscopy. Science **270**, 1646 (1995)
15. Barth, C., Reichling, M.: Imaging the atomic arrangement on the high-temperature reconstructed α-Al_2O_3(0001) surface. Nature **414**, 54 (2001)
16. Allers, W., Langkat, S., Wiesendanger, R.: Dynamic low-temperature scanning force microscopy on nickel oxide (001). Appl. Phys. A **72**, S27 (2001)
17. Hölscher, H., Langkat, S.M., Schwarz, A., Wiesendanger, R.: Measurement of threedimensional force fields with atomic resolution using dynamic force spectroscopy. Appl. Phys. Lett. **81**, 4428 (2002)
18. Loppacher, C., Guggisberg, M., Pfeiffer, O., Meyer, E., Bammerlin, M., Luthi, R., Schlittler, R., Gimzewski, J.K., Tang, H., Joachim, C.: Direct determination of the energy required to operate a single molecule switch. Phys. Rev. Lett. **90**, 066107 (2003)
19. Sugimoto, Y., Abe, M., Hirayama, S., Oyabu, N., Custance, O., Morita, S.: Atom inlays performed at room temperature using atomic force microscopy. Nat. Mater. **4**, 156 (2005)

AFM, Tapping Mode

Hendrik Hölscher
Karlsruher Institut für Technologie (KIT), Institut für Mikrostrukturtechnik, Karlsruhe, Germany

Definition

The *tapping* or AM-mode is the most common dynamic mode used in atomic force microscopy. In dynamic mode AFM the cantilever is oscillated with (or near) its resonance frequency near the sample surface. Using a feedback electronic the cantilever sample distance is controlled by keeping either the amplitude or the phase of the oscillating cantilever constant. Since lateral tip–sample forces are avoided by this technique the resolution is typically higher

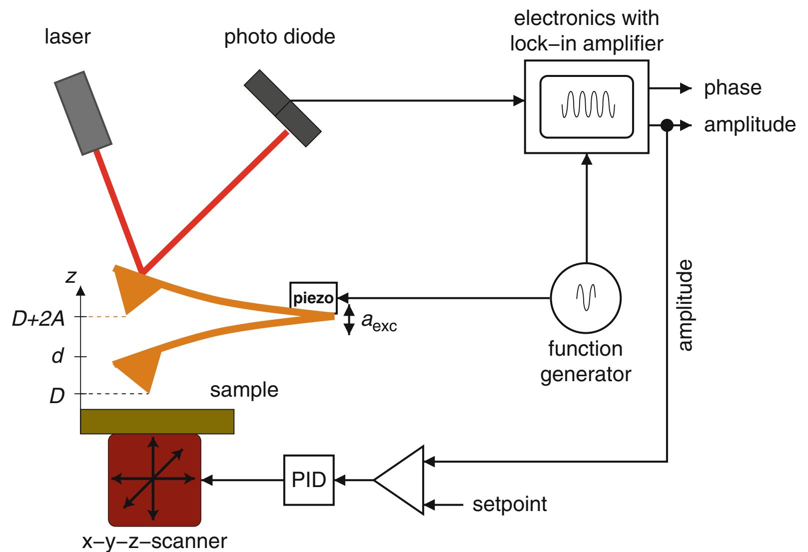

AFM, Tapping Mode, Fig. 1 Setup of a dynamic force microscope operated in the tapping (or AM-) mode. A laser beam is deflected by the back side of the cantilever, and its deflection is detected by a split photo-diode. The cantilever vibration is caused by an external frequency generator driving an excitation piezo. A lock-in amplifier is used to compare the cantilever driving with its oscillation. The amplitude signal is held constant by a feedback loop controlling the cantilever sample distance

compared to the classical contact mode AFM where tip and sample are in direct mechanical contact.

Overview

Since its introduction in 1986 [1], the *atomic force microscope* became a standard tool in nanotechnology. In early experimental setups, a sharp tip located at or near the end of a microstructured cantilever profiled the sample surface in direct mechanical contact (*contact mode*) to measure the force acting between tip and sample. Maps of constant tip–sample interaction force, which are usually regarded as representing the sample's "topography," were then recovered by keeping the deflection of the cantilever constant (▶ Friction Force Microscopy). This is achieved by means of a feedback loop that continuously adjusts the *z*-position of the sample during the scan process so that the output of the deflection sensor remains unchanged at a preselected set-point.

Despite the widespread success of contact mode AFM in various applications, the resolution was frequently found to be limited (in particular for soft samples) by lateral forces acting between tip and sample. In order to avoid this effect, it is advantageous to vibrate the cantilever in vertical direction near the sample surface. AFM imaging with an oscillating cantilever is often denoted as *dynamic force microscopy* (DFM) [2].

The cantilever dynamics are governed by the tip–sample interaction as well as by its driving method. For instance, the historically oldest scheme of cantilever excitation in DFM imaging is the external driving of the cantilever at a fixed excitation frequency chosen to be exactly at, or very close to, the cantilever's first resonance. For this driving mechanism, different detection schemes measuring either the change of the oscillation amplitude or the phase shift between driving signal and resulting cantilever motion were proposed. Over the years, the *amplitude modulation* (AM) or *tapping* mode, where the actual value of the oscillation amplitude is employed as a measure of the tip–sample distance, has been established as the most widely applied technique for ambient conditions and liquids.

Experimental Setup

A schematic of the experimental setup of an atomic force microscope driven in amplitude modulation mode is shown in Fig. 1. In this mode the cantilever is vibrated close to its resonant frequency near the sample surface. Due to the tip–sample interaction the resonant frequency (and consequently also amplitude A and phase ϕ) of the cantilever changes with the cantilever sample distance d. Therefore, the amplitude as well as the phase can be used as feedback channels. A certain set-point for example, the amplitude is given, and the feedback loop will adjust the tip–sample distance such that the amplitude remains constant. The cantilever sample distance is

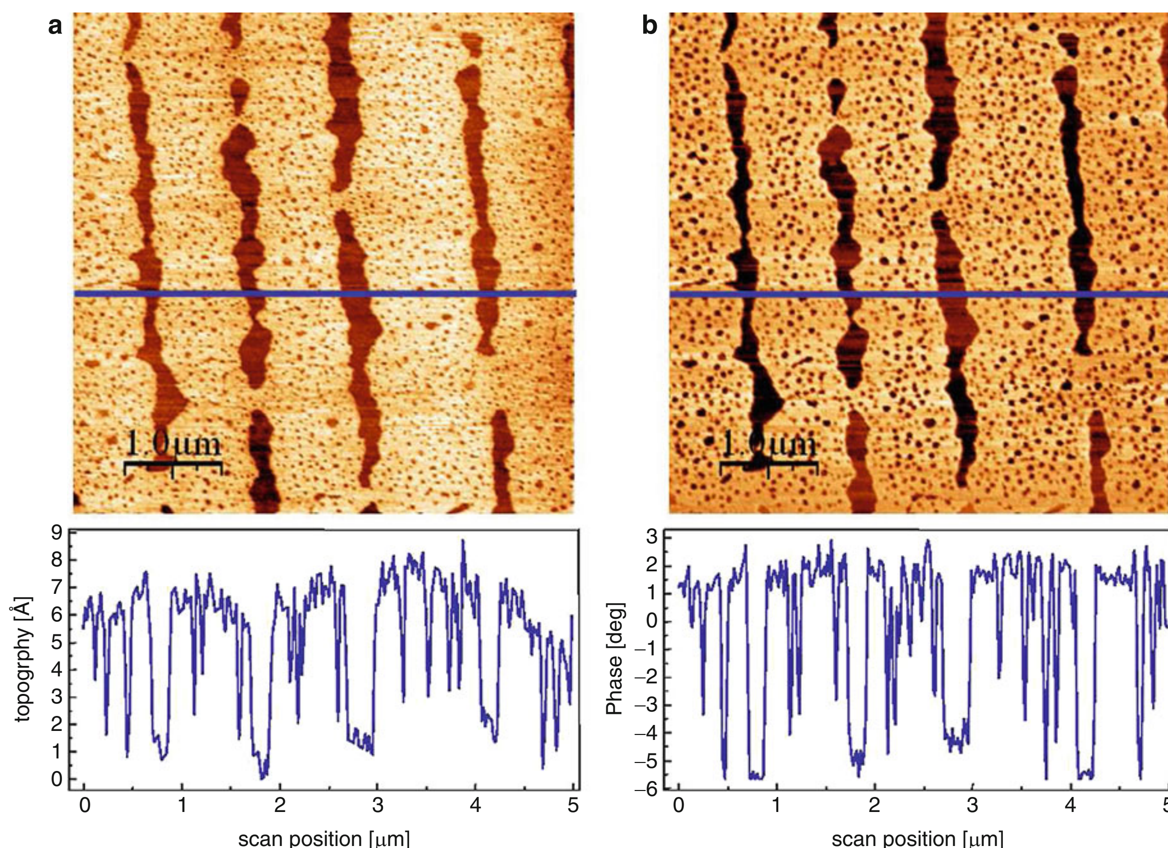

AFM, Tapping Mode, Fig. 2 (**a**) A dynamic force microscopy image of a monomolecular DPPC (L-α-dipalmitoyl-phophatidycholine) film adsorbed on mica. (**b**) The phase contrast is different between substrate and DPPC film. Equation 6 explains how this contrast is related to the energy dissipation caused by the tip–sample contact interaction

recorded as a function of the lateral position of the tip with respect to the sample and the scanned height essentially represents the surface topography.

The deflection of the cantilever is typically measured with the laser beam deflection method. During operation in conventional tapping mode, the cantilever is driven with a fixed frequency and a constant excitation amplitude using an external function generator, while the resulting oscillation amplitude and/or the phase shift are detected by a lock-in amplifier. The function generator supplies not only the signal for the dither piezo; its signal serves simultaneously as a reference for the lock-in amplifier.

This setup is mostly used in air and in liquids. A typical image obtained with this experimental setup in ambient conditions is shown in Fig. 2. The phase between excitation and oscillation can be acquired as an additional channel and gives information about the different material properties of DPPC and the mica substrate. As shown at the end of the next section, the phase signal is closely related to the energy dissipated in the tip–sample contact.

Due to its technical relevance the investigation of polymers has been the focus of many studies and high-resolution imaging has been extensively performed in the area of material science. Using specific tips with additionally grown sharp spikes Klinov et al. [3] obtained molecular resolution on a polydiacetylene crystal. Imaging in liquids opens up the avenue for the investigation of biological samples in their natural environment. For example, Möller et al. [4] have obtained high-resolution images

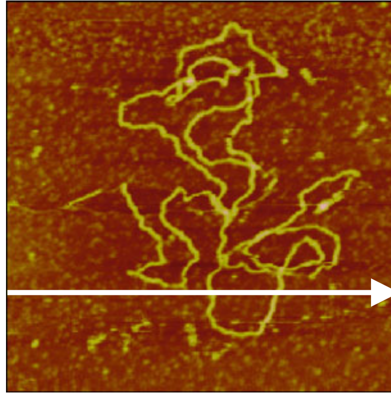

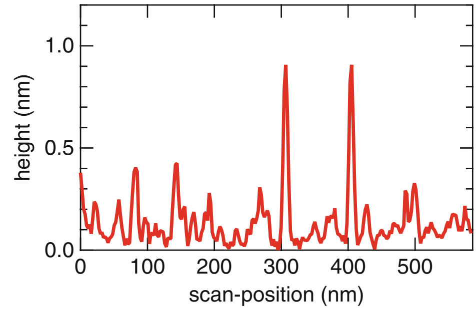

AFM, Tapping Mode, Fig. 3 Topography of DNA adsorbed on mica imaged in buffer solution by tapping mode AFM. The *right* graph shows a single scan line obtained at the position marked by an arrow in the *left* image

of the topography of hexagonally packed intermediate (HPI) layer of *Deinococcus radiodurans* with tapping-mode AFM. A typical example for the imaging of DNA in liquid solution is shown in Fig. 3.

Theory of Tapping-Mode AFM

Many features observed in tapping-mode AFM can be described by a simple spring-mass model which includes the tip–sample interaction force.

$$m\ddot{z}(t) + \frac{2\pi f_0 m}{Q_0}\dot{z}(t) + c_z(z(t) - d) = \underbrace{a_{\mathrm{d}} cz \cos(2\pi f_{\mathrm{d}} t)}_{\text{external driving force}} + \underbrace{F_{\mathrm{ts}}[z(t), \dot{z}(t)]}_{\text{tip-sample force}}. \quad (1)$$

Here, $z(t)$ is the position of the tip at the time t; c_z, m, and $f_0 = \sqrt{(c_z/m)}/(2\pi)$ are the spring constant, the effective mass, and the eigenfrequency of the cantilever, respectively. The quality factor Q_0 combines the intrinsic damping of the cantilever and all influences from surrounding media, such as air or liquid. The equilibrium position of the tip is denoted as d. The first term on the right-hand side of the equation represents the external driving force of the cantilever by the frequency generator. It is modulated with the constant excitation amplitude a_{d} at a fixed frequency f_{d}. The (nonlinear) tip–sample interaction force F_{ts} is introduced by the second term.

The actual tip–sample force is unknown in nearly all cases. However, in order to understand the most important effects it is often sufficient to apply the *DMT-M theory* [5]. In this approach it is assumed the tip is nearly spherical and that the noncontact forces are given by the long-range van-der-Waals forces while the contact forces are described by the well-known Hertz model. The resulting overall force law is given by

$$F_{\mathrm{DMT-M}}(z) = \begin{cases} -\frac{A_H R}{6z^2} & \text{for} \quad z \geq z_0, \\ \frac{4}{3}E^*\sqrt{R}(z_0 - z)^{3/2} & \text{for} \quad z < z_0, \end{cases} \quad (2)$$

where A_H is the Hamaker constant, E^* the effective modulus, and R the tip radius. At z_0 tip and sample come in contact. Figure 4 displays the resulting tip–sample force curve for this model.

For the analysis of dynamic force microscopy, experiments only on the steady states with sinusoidal cantilever oscillation are of interest. Consequently, the steady-state solution is given by the ansatz

$$z(t \gg 0) = d + A\cos(2\pi f_{\mathrm{d}} t + \phi), \quad (3)$$

where ϕ is the phase difference between the excitation and the oscillation of the cantilever.

Here, the situation where the driving frequency is set *exactly* to the eigenfrequency of the cantilever ($f_{\mathrm{d}} = f_0$) is analyzed. With this choice, which is also very common in actual DFM experiments, defined imaging conditions are given leading to a handy formula relationship between the free oscillation amplitude A_0, the actual amplitude A, and the equilibrium tip position d [6].

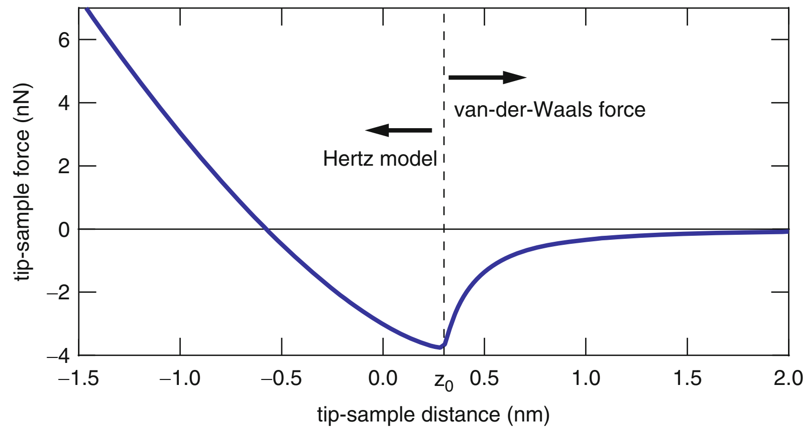

AFM, Tapping Mode, Fig. 4 Tip–sample model force after the DMT-M model for air Eq. 2 using the typical parameters: $A_H = 0.2$ aJ, $R = 10$ nm, $z_0 = 0.3$ nm, and $E^* = 1$ GPa. The *dashed line* marks the position z_0 where the tip touches the surface

$$A_0 = A\sqrt{1 + (Q_0 I_+[d, A])^2}, \quad (4)$$

where

$$\begin{aligned} I_+(d, A) &= \frac{2f_d}{c_z A} \int_0^{1/f_d} F_{ts}[z(t), \dot{z}(t)] \cos(2\pi f_d t + \phi) dt \\ &= \frac{1}{p c_z A^2} \int_{d-A}^{d+A} (F_\downarrow + F_\uparrow) \frac{z - d}{\sqrt{A^2 - (z - d)^2}} dz. \end{aligned} \quad (5)$$

The function $I_+(d, A)$ depends on the actual oscillation amplitude A and cantilever–sample distance d and it is a weighted average of the tip–sample forces during approach and retraction ($F_\downarrow + F_\uparrow$).

The solution of this equation allows us to study amplitude vs. distance curves as shown in Fig. 5 for a Q-factor of 300. Most noticeable, the tapping mode curve exhibits jumps between unstable branches, which occur at different locations for approach and retraction. The resulting bistable regime then causes a hysteresis between approach and retraction and divides the tip–sample interaction into two regimes. In order to identify the forces acting between tip and sample in these two regimes, the oscillation amplitude is plotted as a function of the nearest tip–sample distance in Fig. 6. In addition, the bottom graph depicts the corresponding tip–sample force (cf. Fig. 4). The origin of the nearest tip–sample position D is defined by this force curve. Since both, the amplitude curves and the tip–sample force curve, are plotted as a function of the nearest tip–sample position, it is possible to identify the resulting maximum tip–sample interaction force for a given oscillation amplitude.

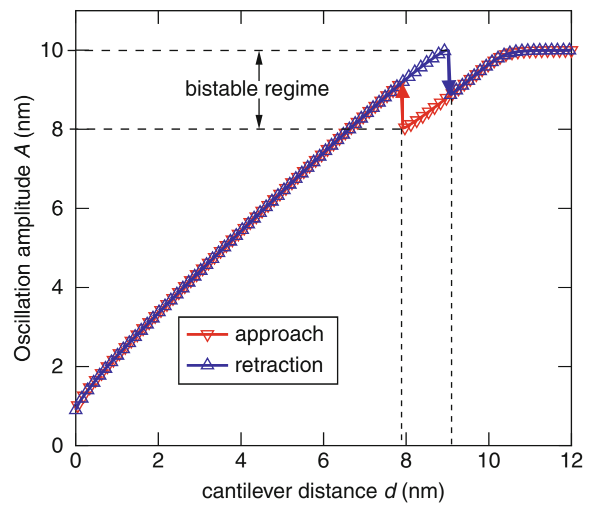

AFM, Tapping Mode, Fig. 5 Amplitude vs. distance curve for tapping-mode AFM assuming the parameters $A_0 = 10$ nm, $f_0 = 300$ kHz, and the tip–sample interaction force shown in Fig. 4. The overall amplitude decreases the sample surface distance, but instabilities (indicated by *arrows*) occur during approach and retraction

During the approach of the vibrating cantilever toward the sample surface, there is discontinuity in the nearest tip–sample position D. This gap corresponds to the bi-stability and the resulting jumps in the amplitude vs. distance curve. After the jump from the attractive to the repulsive regime has occurred, the amplitude decreases continuously. The nearest tip–sample position, however, does not reduce accordingly, remaining roughly between −0.8 and −1.5 nm. As a result, larger A/A_0 ratios do not necessarily result into lower tip–sample interactions, which is important to keep in

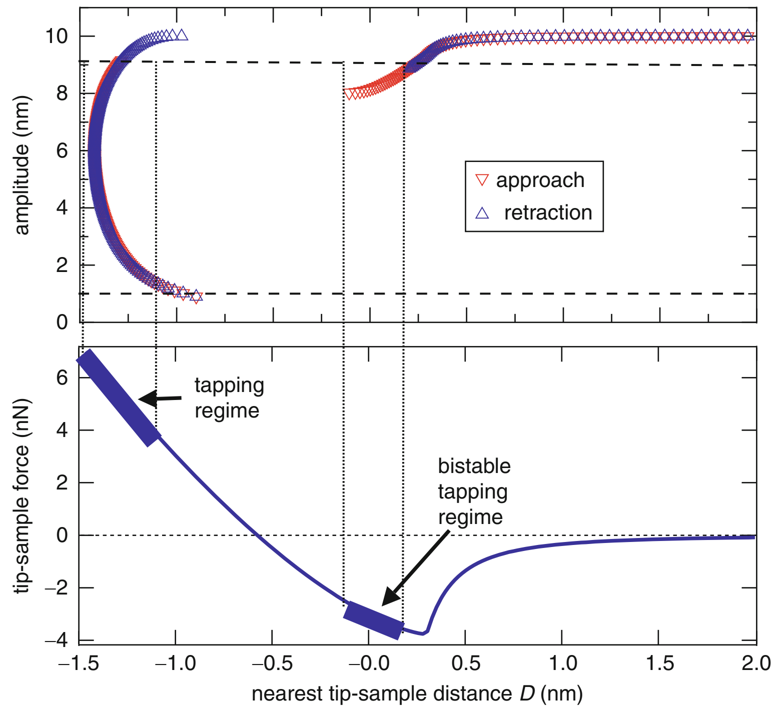

AFM, Tapping Mode, Fig. 6 A comparison between the maximum tip–sample forces (tip–sample forces acting at the point of closest tip–sample approach/nearest tip–sample position D) experienced by conventional "tapping mode" AM-AFM assuming the same parameters as in Fig. 5. The *upper* graph shows the nearest tip–sample position D vs. the actual oscillation amplitude A for tapping mode. The graph at the *bottom* reveals the force regimes sensed by the tip. The maximal tip–sample forces in tapping mode are on the repulsive (tapping regime) as well as attractive (bistable tapping regime) part of the tip–sample force curve

mind while adjusting imaging parameters in tapping mode. For practical applications, it is reasonable to assume that the set-point of the amplitude used for imaging has been set to a value between 90% and 10% of the free oscillation amplitude. With this condition, one can identify the accessible imaging regimes indicated by the horizontal (dashed) lines and the corresponding vertical (dotted) lines. Therefore, in tapping mode, two imaging regimes are typically accessible: the *tapping regime* (left) and the *bistable tapping regime* (middle). The bistable imaging state is only accessible during approach. Imaging in this regime is indeed possible with the limitation that the oscillating cantilever might jump into the repulsive regime [7, 8].

In the above paragraphs, the influence of the tip–sample interaction on the cantilever oscillation was analyzed, the maximum tip–sample interaction forces based on the assumption of a specific model force was calculated, and subsequently possible routes for image optimization were discussed. However, in practical imaging, the tip–sample interaction is not a priori known. Therefore, several authors [9–14] suggested solutions to this inversion problem, but some of them need further technical equipment. However, most commercial systems give access to amplitude and phase vs. distance data which already allows the reconstruction of the tip–sample force curve applying numerical procedures [11, 12, 14].

The energy dissipation caused by the tip–sample interaction can be easily calculated using the conservation of energy principle [15].

$$\Delta E = \left(\frac{1}{Q_0} \frac{f_d}{f_0} + \frac{a_d}{A} \sin \phi \right) \pi c_z A^2. \quad (6)$$

Since all parameters – except the phase ϕ – are constant during scanning, this formula shows that the energy dissipation is roughly proportional to $\sin \phi$ as already mentioned in the caption of Fig. 2.

Cross-References

▶ AFM, Non-contact Mode
▶ Friction Force Microscopy
▶ Kelvin Probe Force Microscopy
▶ Magnetic Resonance Force Microscopy
▶ Piezoresponse Force Microscopy and Spectroscopy

References

1. Binnig, G., Quate, C.F., Gerber, Ch: Atomic force microscopy. Phys. Rev. Lett. **56**, 930–933 (1986)
2. Garcia, R., Pérez, R.: Dynamic atomic force microscopy methods. Surf. Sci. Rep. **47**, 197–301 (2002)
3. Klinov, D., Maganov, S.: True molecular resolution in tapping-mode atomic force microscopy with high-resolution probes. Appl. Phys. Lett. **84**, 2697–2698 (2004)
4. Möller, C., Allen, M., Elings, V., Engel, A., Müller, D.J.: Tapping-mode atomic force microscopy produces faithful high-resolution images of protein surfaces. Biophys. J. **77**, 1150–1158 (1999)
5. Schwarz, U.D.: A generalized analytical model for the elastic deformation of an adhesive contact between a sphere and a flat surface. J. Coll. Interf. Sci. **261**, 99–106 (2003)
6. Hölscher, H., Schwarz, U.D.: Theory of amplitude modulation atomic force microscopy with and without Q-control. Int. J. Nonlinear Mech. **42**, 608–625 (2007)
7. Paulo, A.S., García, R.: High-resolution imaging of antibodies by tapping-mode atomic force microscopy: Attractive and repulsive tip-sample interaction regimes. Biophys. J. **78**, 1599–1605 (2000)
8. Stark, R.W., Schitter, G., Stemmer, A.: Tuning the interaction forces in tapping mode atomic force microscopy. Phys. Rev. B **68**, 085401 (2003)
9. Stark, M., Stark, R.W., Heckl, W.M., Guckenberger, R.: Inverting dynamic force microscopy: From signals to time-resolved interaction forces. PNAS **99**, 8473–8478 (2002)
10. Legleiter, J., Park, M., Cusick, B., Kowalewski, T.: Scanning probe acceleration microscopy (SPAM) in fluids: Mapping mechanical properties of surfaces at the nanoscale. Proc. Natl. Acad. Sci. U.S.A. **103**, 4813–4818 (2006)
11. Lee, M., Jhe, W.: General solution of amplitude-modulation atomic force microscopy. Phys. Rev. Lett. **97**, 036104 (2006)
12. Hölscher, H.: Quantitative measurement of tip-sample interactions in amplitude modulation atomic force microscopy. Appl. Phys. Lett. **89**, 123109 (2006)
13. Sahin, O., Maganov, S., Chanmin, Su, Quate, C., Solgaard, O.: An atomic force microscope tip designed to measure time-varying nanomechanical forces. Nat. Nanotechnol. **2**, 507–514 (2007)
14. Shuiqing, Hu, Raman, A.: Inverting amplitude and phase to reconstruct tip-sample interaction forces in tapping mode atomic force microscopy. Nanotechnology **19**, 375704 (2008)
15. Cleveland, J.P., Anczykowski, B., Schmid, A.E., Elings, V.B.: Energy dissipation in tapping-mode atomic force microscopy. Appl. Phys. Lett. **72**, 2613 (1998)

Aging

▶ Fate of Manufactured Nanoparticles in Aqueous Environment

ALD

▶ Atomic Layer Deposition

Alkanethiols

▶ BioPatterning

AlN

▶ Piezoelectric MEMS Switches

Alteration

▶ Fate of Manufactured Nanoparticles in Aqueous Environment

Aluminum Nitride

▶ Piezoelectric MEMS Switches

Amphibian Larvae

▶ Ecotoxicology of Carbon Nanotubes Toward Amphibian Larvae

Anamorphic Particle Tracking

▶ Astigmatic Micro Particle Imaging

S

Sand Skink

▶ Friction-Reducing Sandfish Skin

SANS

▶ Small-Angle Scattering of Nanostructures and Nanomaterials

SAXS

▶ Small-Angle Scattering of Nanostructures and Nanomaterials

Scanning Electron Microscopy

Yimei Zhu[1] and Hiromi Inada[2]
[1]Center for Functional Nanomaterials, Brookhaven National Lab, Upton, NY, USA
[2]Hitachi High-Technologies America, Pleasanton, CA, USA

Synonyms

Scanning electron microscopy and secondary-electron imaging microscopy

Definition

A scanning electron microscope (SEM) is an instrument that uses high-energy electrons in a raster-scan pattern to form images, or collect other signals, from the three-dimensional surface of a sample.

Introduction

The scanning electron microscope (SEM) is one of the most popular and user-friendly imaging tools that reveal the surface topography of a sample. It is also widely used for structural characterization of materials and devices, especially in the field of nanotechnology. Today there are in excess of 50,000 SEMs worldwide and it is often seen as a "must-have" apparatus for research institutes and industry laboratories. In the SEM, incident electrons interact with the atoms that make up the sample-producing signals that contain information about the sample's surface morphology, composition, and other physical and chemical properties. The most common imaging mode in SEM lies in using secondary electrons. Since secondary electrons have very low energies, they are generated in, and escape from regions near the sample surface. Combined with various detection systems, a SEM also can be used to determine the sample's chemical composition through energy-dispersive x-ray spectroscopy and Auger electron spectroscopy, and identify its phases through analyzing electron-diffraction patterns, mostly via high-energy backscattered electrons. Besides backscattered electrons, Auger electrons, characteristic x-rays, other signals are generated from the interactions of the incident

B. Bhushan (ed.), *Encyclopedia of Nanotechnology*, DOI 10.1007/978-90-481-9751-4,
© Springer Science+Business Media B.V. 2012

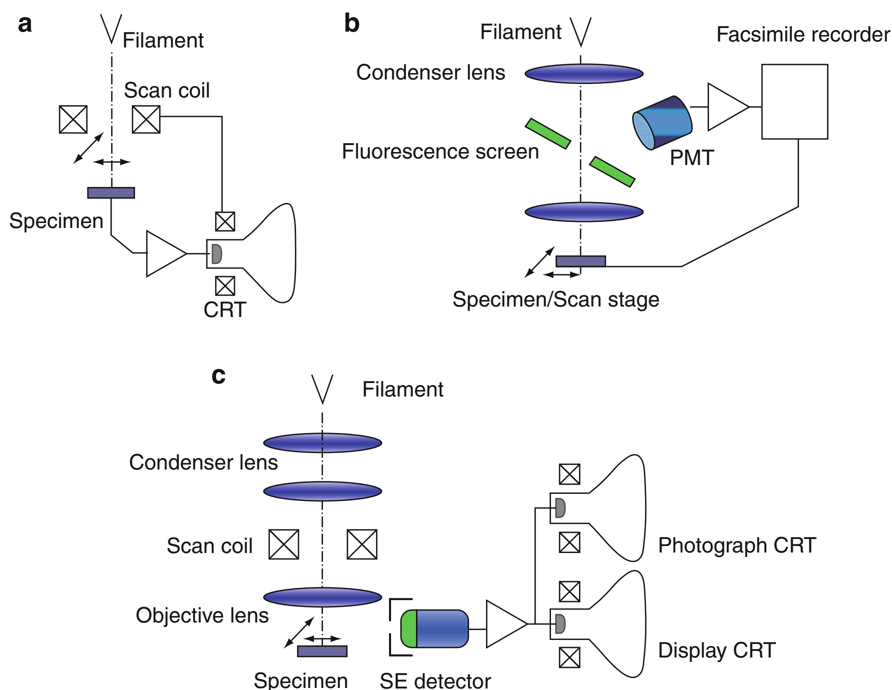

Scanning Electron Microscopy, Fig. 1 Schematics of configurations of the scanning electron microscopes proposed and developed by some notable pioneers in the SEM history. (**a**) Knoll in 1935, (**b**) Zworykin in 1945, and, (**c**) Cambridge Instruments in 1965

beam and the sample under a SEM include plasmons, bremsstrahlung radiation (noncharacteristic x-rays), cathodoluminescence, and electron-beam-induced current. This entry is focused on secondary-electron imaging related instrumentation, signal-generation processes, and state-of-the-art imaging capabilities in SEM.

A Brief History

SEM was invented by Max Knoll in 1935 in Germany [1] to study the targets of television tubes. The instrument consisted of electron-beam deflector coils that scan the beam on a plate as the sample in a cathode ray tube (CRT), and an amplifier that boosts the plate current to display the signal on another CRT (Fig. 1a). Two years later Manfred von Ardenne built an electron microscope with a highly demagnified probe using two condenser lenses for scanning transmission electron microscopy and also tried it as an SEM. Zworykin and his coworkers of the RCA Laboratories in the USA designed and built a dedicated SEM in 1942. Its electron optics includes three electrostatic lenses with scan coils placed between the second and third ones. A photomultiplier was first used to detect secondary electrons (Fig. 1b). The essential components of this apparatus are similar to those used in modern SEMs. The probe size of the incident, or primary, electron beam had a diameter of about 10 nm. However, compared with transmission electron microscopes (TEMs) at that period, it could not image secondary electrons satisfactorily due to the poor signal-to-noise ratios of the images [3]. Sir Charles Oatley and Dennis McMullan built their first SEM at Cambridge University in 1948. The SEM technology was further pioneered by many postgraduate students at Cambridge including Gary Stewart. The first commercial instrument, named as “Stereoscan,” was launched in 1965 by the Cambridge Scientific Instrument Company for DuPont [4]. The instrument consists of electron multiplier detector with beryllium–copper dynodes to detect scattered electrons from the specimen surface. Images were displayed on a CRT, while another synchronized CRT recorded them on camera film. An Everhart-Thornley type secondary-electron detector [5] significantly improved the detection efficiency of the low-energy secondary-electron signals (Fig. 1c). JEOL produced first commercial Japanese SEM, JSM-1, in 1966, while Hitachi commercialized its SEM, HSM-2, in 1969.

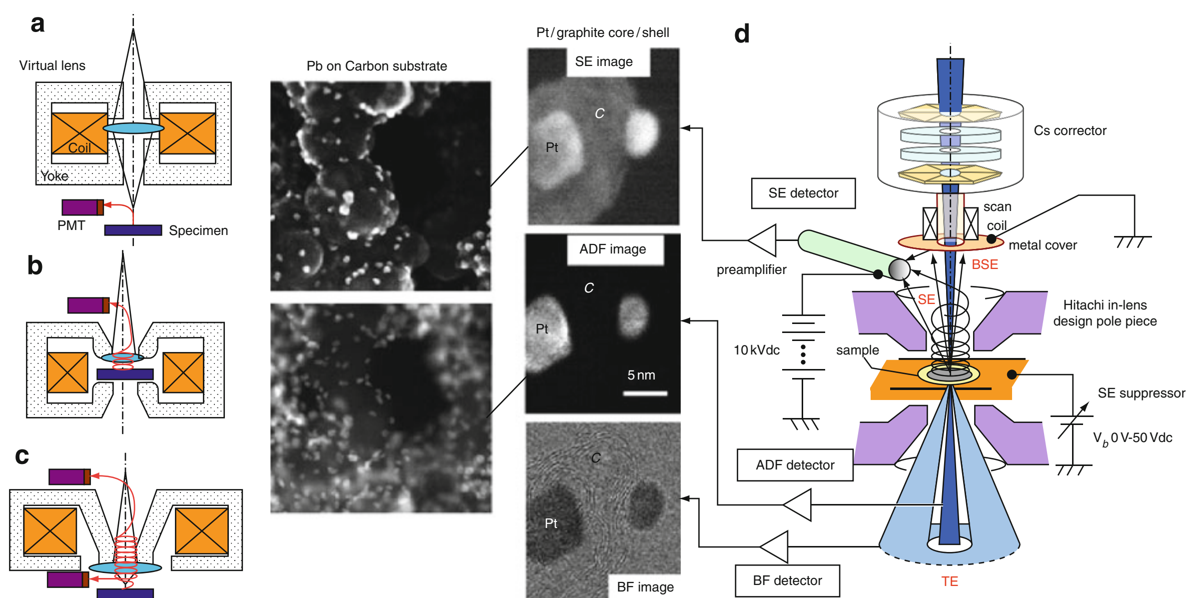

Scanning Electron Microscopy, Fig. 2 (**a–c**) Three different objective lens designs. (**a**) Out-lens, (**b**) in-lens, and (**c**) semi-in-lens. (**d**) Schematic of the lens-detector configuration of the aberration-corrected scanning electron microscope, Hitachi HD2700C, that routinely achieves an atomic resolution in imaging using secondary electrons and transmitted electrons. Two examples are shown on the *left*; one is Pb particles on a carbon support, the other is Pt particles with carbon-graphite shells. *BF* bright-field, *ADF* annular dark-field, *SE* secondary electrons, *TE* transmitted electrons, and *BES* backscattered electrons. The SE images clearly give a topographic view of the area, and higher brightness of the light element C, compared with the corresponding ADF images

Instrumentation

A typical SEM consists of an electron gun, an electron lens system, various electron-beam deflection coils, electron detectors, and display and recording devices [6]. In a SEM, an electron beam is emitted from an electron gun sitting on a thermionic filament cathode, or from a field-emission needle tip. Tungsten is often used for thermionic electron guns due to its low cost, high melting point, and low vapor pressure so that it tolerates heating to about 2,800 K for electron emission. Other types of electron emitters include lanthanum hexaboride (LaB6) cathodes, which offer higher brightness but require a better vacuum to avoid oxidizing the gun. Field emission guns (FEGs) often used in modern SEMs can be the thermally assisted Schottky type, using emitters of zirconium oxide (ZrO), or the cold-cathode type using tungsten <310 > single crystal emitters and operated at room temperature. A cold field-emission gun has a much smaller source size (5 $\sim$ 10 nm) than a tungsten filament (1 $\sim$ 10 μm) with three to four orders of magnitude larger current density and brightness [7].

The typical energy range of the electron beam used in SEM is from 0.5 to 40 keV. The electron-condenser lens system usually demagnifies the electron source more than hundreds of times to form a small probe on the sample. The beam passes through pairs of deflection coils, or scanning coils, in the electron column, typically in the final lens, which deflect the beam in the x and y axes by applying an incremental current into the scan coils, so that it scans in a raster fashion over a rectangular area of the sample surface.

Historically, SEM incorporates an objective lens. Unlike the objective lens in optical microscopes or transmission electron microscopes (TEMs), its purpose in SEM is not to image the sample, but to focus the small probe on the sample. There are three types of objective lenses: out-lens (Fig. 2a); in-lens (Fig. 2b); and, semi in-lens (Fig. 2c). Most early SEMs had the simplest out-lens design, in which the sample sits beneath the lens leaving a large area available in the sample chamber. However, the yoke gap across the optical axis acts as a lens with leakage field, thus yielding significant imaging aberration. The in-lens pole piece, originally designed for TEMs, was

adopted for SEM to reduce spherical aberration. Hitachi developed the first commercial SEM with such a design in 1985 [8]. Their microscope operating at 30 kV reaches a probe size of 0.5 nm with spherical aberration coefficient C_s of 1.6 mm. The drawback of the design is that a conventional thin sample, similar to that used in TEM, is required because the sample sits inside the pole-piece gap. A design resulting from a compromise between the out-lens and in-lens is the semi in-lens pole piece (Fig. 2c), offering reasonable spatial resolution but with larger open space for the sample chamber so that a thick sample can be used. Such a design allows the sample to be placed a few mm from the pole piece, and a large magnetic field to be applied to produce a smaller focal length and less spherical aberration. SEMs with the semi in-lens design played a significant role in characterizing devices for the semiconductor industry in early 1990s.

It is noteworthy that the in-lens design shown in Fig. 2b is very similar to that used in conventional TEM and/or STEM (scanning transmission electron microscope). Thus, with an efficient secondary-electron detector, a TEM, or an STEM also can image a sample surface [9, 10]. Figure 2d shows a schematic of the objective lens (in-lens design), the sample, and the arrangement of detectors in the Hitachi HD2700C aberration-corrected SEM/STEM [11]. The instrument operates at 80 ~ 200 kV, allowing simultaneous acquisition of bright-field (BF), annular dark-field (ADF), and secondary-electron (SE) images. In the BF and ADF modes, the transmitted electrons are used to form the images, thus providing structural information from the sample's interior. In contrast, in the SE mode electrons emerging from the surface with low energies, or short escape length, are used, and thus, the signals are surface sensitive. Different imaging modes have their own advantages and limitations. Since the BF signals are close to the phase contrast seen in TEM, they offer high spatial resolution, but are difficult to interpret. ADF images, on the other hand, are based on Rutherford scattering, and thus their image intensity is directly related to the sample's atomic number Z (the so-called Z-contrast imaging). Since BF- and ADF-images are projected images they give little structural information in the direction of the beam's trajectory. In contrast, SE imaging offers depth information on the surface topography, and is more sensitive to the light elements than is ADF imaging (see Fig. 2d). Combining these different imaging modes in an electron microscope with an in-lens design, it has been demonstrated that simultaneously imaging both surface (SE) and bulk (ADF) at atomic resolution is possible in thin samples for a wide range of elements, from uranium and gold to silicon and carbon [11, 12].

The electron detector is another important part of the SEM instrumentation. Although detector itself does not determine the image resolution in SEMs, it is essential to improving the SEM resolving power in terms of the signal-to-noise ratio. The commonest detector used in SEMs today still is that developed by Everhart and Thornley in 1957 [5], the so-called E-T detector. The detector consists of a photomultiplier, a light guide, and a positively biased scintillator. To attract low energy electrons effectively, the scintillator is applied a 10 kV dc bias to accelerate the electrons. The energized electrons cause the scintillator to emit flashes of light (cathodoluminescence) that then are transmitted to the photomultiplier. The amplified output of the electrical signals by the photomultiplier is displayed as a two-dimensional intensity distribution that can be viewed and photographed on an analogue video display. The Everhart-Thornley detector, which normally is positioned to one side above the specimen, exhibits low efficiency in detecting backscattered electrons because few such electrons are emitted in the solid angle subtended by the detector. Furthermore, its positive bias cannot readily attract the high-energy backscattered electrons (close to the energy of the incident electrons). Backscattered electrons are usually collected above the sample in a "doughnut type" arrangement, concentric with the electron beam, to maximize the solid angle of collection.

Secondary-Electron Signal Generation

Secondary-electron (SE) imaging is the most frequently used mode of imaging in SEM. Secondary electrons, defined as the electrons with energy below 50 eV, are generated along the primary electrons' trajectories within the sample, but are subject to elastic and inelastic scattering during their passage through the sample. These electrons can be valence electrons or are ejected from the orbits of the inner shells (most likely the k-shells) of the sample. The consequence of their low kinetic energy is their shallow escape depth, which is about 1 nm for metals, and up to 10 nm for

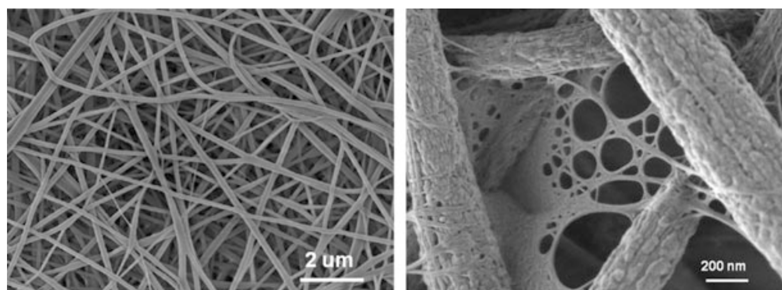

Scanning Electron Microscopy, Fig. 3 SEM micrographs of a polymer membrane that consists of electrospun fibrous scaffold for water filtration. The fibrous scaffold has an average diameter of 200 nm. The high-resolution SEM image on the right shows cellulose nanofibers (5–10 nm in diameter) infused into the scaffold form a cellulose network to enhance the membrane's ability to remove bacteria and viruses. The images were taken with JEOL7600 SEM at operation voltage of 0.5 eV. A thin layer of carbon was coated on the sample to avoid charging. Note the bright contrast at the edge of the fibers generates a topological view of the fibrous structure

insulators. The probability of escape decreases continuously with the increase of the depth below the surface. However, there is a nonzero probability of secondary-electron emission arising from inelastic scattering below the escape depth, as, for example, when a primary electron creates a fast secondary electron (energy > 50 eV) that travels toward the surface and generates a lower-energy secondary electron within the escape depth. The production of the secondary electron signals involves the generation, propagation, escape from the surface, and arrival at the detector. These four processes are detailed in the atomic-imaging section.

The secondary electrons discussed here are often referred to as SE_I, i.e., the secondary electrons generated by the incident beam upon entering the sample. Secondary electrons generated by backscattered electrons when leaving the sample are termed SE_{II}. Secondary electrons generated when the backscattered electrons strike a lens pole piece or the sample chamber's wall, and by primary electrons hitting the aperture are, respectively called SE_{III} and SE_{IV}. Although SE_{III} contain the information on the sample, SE_{IV} do not. Furthermore, there are fast secondary electrons, with energy higher than 50 eV. Bias experiments, wherein a positive dc voltage is applied to the sample to suppress the emission of the secondary electrons, were mainly designed to separate the SE_I from backscattered electrons; they cannot distinguish SE_I from SE_{II}, which for a very thin specimen should be negligible. Measuring other types of secondary electrons, including those with high energy, would require a different bias experiment. Heavy elements (high atomic number) that backscatter electrons more strongly than do light elements (low atomic number), and thus appear brighter in the image, can be used to yield contrast that contains information of a sample's chemical composition.

Figure 3 shows SEM images of a nanofiber-containing polymer membrane developed for water filtration with enhanced ability to remove bacteria and viruses. The image on the right shows the structural network formed by the 5–10 nm diameter cellulose nanofibers. It reveals astonishing topographic details on how the cellulose nanofibers are interwoven with scaffold. In SEM images flat surfaces give even contrast while curved surfaces and sharp edges often appear brighter (high image intensity). This is due to the increased escape of secondary electrons from the top and side surfaces when the interaction volume intercepts them. Since the secondary electron detector is biased with a high acceleration voltage, a surface facing away from the detector still can be imaged. Surfaces tilted away from the normal to the beam allow more secondary electrons to escape [13].

Atomic Imaging Using Secondary Electrons

In the last decade or so, high-resolution SEM has proven an indispensable critical dimension metrology tool for the semiconductor industry. The roadmap for semiconductor nanotechnology identifies the need for ultra-high-resolution SEM in the quest for ever-decreasing device sizes. In a SEM, the size of

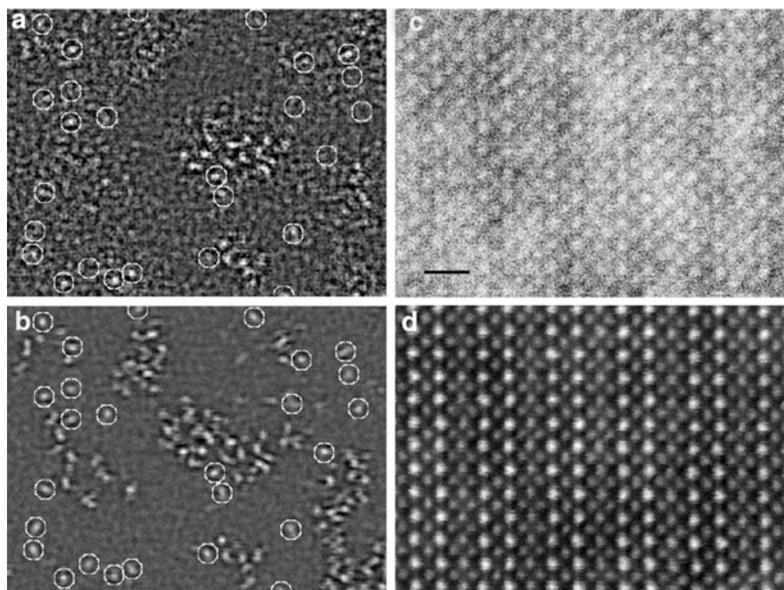

Scanning Electron Microscopy, Fig. 4 (**a–b**) Simultaneous atomic imaging using secondary electrons (secondary-electron mode, **a**) and transmitted electrons (annual dark-field mode, **b**) of uranium individual atoms on a carbon support (raw data). The circles mark the single uranium atoms. The atoms shown in (**b**) but not in (**a**) are presumably those on the back side of the support. (**c–d**) Simultaneous atomic imaging using secondary electrons (**c**) and transmitted electrons (**d**) of $YBa_2Cu_3O_7$ superconductor viewing along the [010] direction (raw data). The scale bar in (**c**) is 0.7 nm

the imaging probe often determines the instrument's resolution power. The probe size d (measured in full-width and half maximum) is a function of the beam convergence half-angle α is an incoherent sum of contributions from source size, diffraction limit, spherical aberration, and chromatic aberration, and is given by

$$d^2 = \left(\frac{4i_p}{\beta\pi^2\alpha^2}\right)^2 + \left(\frac{0.6\lambda}{\alpha}\right)^2 + (0.5C_s\alpha^3)^2 + \left(C_c\alpha\frac{\Delta E}{E}\right)^2$$

where $i_p$is the probe current, α is the convergence half-angle, β is the source brightness, λ is the electron wavelength at beam energy E, ΔE is the energy spread, and C_s and C_c are, respectively, the spherical- and chromatic-aberration coefficients of the probe-forming lens. The first term on the right side of the equation is the probe size defined by the source size, the second term is due to the diffraction limit, and the third and the fourth terms are due, respectively, to the spherical and chromatic aberrations. Recent advancement on correcting spherical aberration in SEM and STEM diminishes C_s to zero, thus eliminating the third term and produces a small probe. It is important to note that the probe size also depends on the energy spread in the fourth term that includes the energy distribution of the primary electron beam and the fluctuation of the instruments' acceleration voltage.

In SEM, the image resolution depends not only on the instrument, but also on the sample, or, more accurately, on the sampling volume of the sample from which the signal is generated When the incident electrons impinge on a point of the sample's surface, they interact with atoms in the sample via elastic- (change trajectory) and inelastic- (lose energy) interactions. The size of the interaction volume depends on the electron's landing energy, the atomic number of the sample, and its density. The simultaneous energy loss and change in trajectory spreads beam into the bulk of the sample and produces an interaction volume therein, that, for a thick sample, can extend from less than 100 nm to around 5 μm into the surface, i.e., more than an order of magnitude larger than the original probe size. For a very thin sample (a few nm thick), the interaction volume, as the first approximation, might be defined as the probe size.

Figure 4 illustrates the atomic resolution images using secondary electrons on single uranium atoms (a) and the (010) surface of a $YBa_2Cu_3O_7$ crystal (c) recorded on the Hitachi HD2700C SEM/STEM (Fig. 2d). For comparison, the corresponding annular dark-field images using transmitted electrons, (b) and (d), respectively, are included. The equally sharp images in SE and ADF suggest negligible imaging delocalization. Such an attainable resolution was attributed to the combination of several factors: Better design of the electro-optics of the instrument (including ultrahigh electric and mechanical stabilities) and

the detector; aberration correction that reduces the probe size and increases the probe current; and, the higher operation voltage that beneficially assures a very small volume of beam interaction for a thin sample.

The physical mechanism of producing the low-energy secondary electrons traditionally is ascribed to inelastic scattering and decay of collective electron excitation with the incident electron giving up, say 20 eV, to produce a secondary electron with energy 20 eV minus the work function of the surface. Since the momentum transfer (scattering angle) of the scattering with 20 eV energy loss is small, the transfer should be delocalized to an area >1 nm; thus atomic imaging using secondary electrons was not considered possible. Recent studies suggest that this is not the primary mechanism for secondary-electron imaging at least on a thin sample [11]. The secondary electrons responsible for atomic-scale resolution are generated by inelastic scattering events with large momentum transfer, including those from inner shell orbitals, which give rise to a sharp central peak in the point-spread function for signal generation.

In general, four steps are involved in producing the signal that is used to form a secondary electron (SE_I) image [12]. (1) The generation of secondary electrons through the inelastic scattering of primary electrons in the sample, at a generation rate, G; (2) random motion of these secondary electrons, which are scattered by atoms of the specimen both elastically and inelastically (potentially creating other secondary electrons of lower energies), such that, on average, T electrons reach the sample surface for each secondary electron generated; (3) the escape of secondary electrons over the potential barrier at the sample surface of the specimen, with an average probability P; and, (4) the acceleration of the emitted electrons in vacuum, such that a fraction D reaches the electron detector.

The secondary-electron signal S is a product of these four factors: $S = G \cdot T \cdot P \cdot D$. To generate contrast in a scanned-probe image, one or more of the above steps must depend on the x-coordinate of the electron probe in the scan direction, i.e.,

$$\frac{dS}{dx} = I_0 TPD\frac{dG}{dx} + I_0 GPD\frac{dT}{dx} + I_0 GTD\frac{dP}{dx} + I_0 GTP\frac{dD}{dx}$$

For most non-atomically resolved SE images obtained in an SEM, $\frac{dT}{dx}$ provides the main contrast mechanism: Secondary electrons created at an inclined surface or close to a surface step have an increased probability of escape, resulting in surface-topography contrast [14]. Less commonly, variations in surface work function contribute additional contrast by providing a nonzero $\frac{dP}{dx}$. In voltage-contrast applications, changes in surface voltage provide a nonzero $\frac{dD}{dx}$. Atomic-number contrast is possible if the specimen is chemically inhomogeneous and G varies with atomic number, yielding a nonzero $\frac{dG}{dx}$. However, for atomic imaging in a thin sample (Fig. 4), the dominant mechanism can be quite different. $\frac{dG}{dx}$ is likely to play an important role in the atomic-scale contrast as a consequence of Z-dependence inelastic scattering cross section and channeling effect for crystals (for thickness in the order of extinction distance it should be minor). Because secondary electrons are generated through inelastic scattering of the incident electrons, $\frac{dG}{dx}$ is limited by the delocalization of the scattering process, which may be described by the point-spread function for inelastic scattering. The term $\frac{dT}{dx}$ should be small, for adatoms or surface atoms that lie on the detector side of the sample. $\frac{dP}{dx}$ would not become important unless the effective work function varies on an atomic scale, and $\frac{dD}{dx}$ must be also negligible at atomic scale. These assumptions are reasonable because the scattering process disperses secondary electrons over a range of x that is comparable to the escape depth, typically 1–2 nm. Consequently, T, P, and D are x-averages that vary little with x on an atomic scale. For uranium atoms on a carbon substrate, the argument is even simpler; these atoms lie outside the solid, so the terms T and P are not applicable.

Future Remarks

Secondary-electron imaging is the most popular mode of operation of the scanning electron microscope (SEM) and traditionally is used to reveal surface topography. Nevertheless, this imaging method never was regarded as being on the cutting edge of performance, due to its perceived limited spatial resolution in comparison with its TEM or STEM counterparts using transmitted electrons. Recent work using aberration-corrected electron microscopes demonstrated that secondary electron signals in the SEM can resolve both crystal lattices and individual atoms, showing SEM's unprecedented and previously unrealized

imaging capabilities. Furthermore, the work demonstrates the incompleteness of present understanding of the formation of secondary-electron images. Secondary-electron imaging using high acceleration voltage with thin samples can now compete with TEM on spatial resolution, and provide new capabilities, such as depth-resolved profiles, at the atomic level. There seems to be no fundamental reason why atomic resolution in secondary-electron imaging could not be achieved at the accelerating voltages of 0.5–40 keV that are currently used in conventional SEMs. It remains to be seen whether the integrated spherical and chromatic aberration of a probe-forming objective lens can be corrected to a sufficient degree at low operation voltages. One clear outcome thus far is the importance of preparing samples with clean surfaces in order to obtain interpretable and reproducible results.

Acknowledgments The work was supported by the US Department of Energy, Office of Basic Energy Science, Materials Science and Engineering Division, under Contract Number DEAC02–98CH10886.

Cross-References

▶ Robot-Based Automation on the Nanoscale
▶ Scanning Tunneling Microscopy
▶ Transmission Electron Microscopy

References

1. Knoll, M.: Aufladepotentiel und sekundäremission elektronenbestrahlter körper. Z. Tech. Phys. **16**, 467–475 (1935)
2. von Ardenne, M.: Das Elektronen-Rastermikroskop. Praktische Ausführung. Z. Tech. Phys. **19**, 407–416 (1938) (in German)
3. Wells, O.C., Joy, D.C.: The early history and future of the SEM. Surf. Interface Anal. **38**, 1738–1742 (2006)
4. Oatley, C.W.: The early history of the scanning electron microscope. J. Appl. Phys. **53**, R1–R13 (1982)
5. Everhart, T.E., Thornley, R.F.M.: Wide-band detector for micro-microampere low-energy electron currents. J. Sci. Instrum. **37**, 246–248 (1960)
6. Goldstein, G.I., Newbury, D.E., Echlin, P., Joy, D.C., Fiori, C., Lifshin, E.: Scanning Electron Microscopy and x-ray Microanalysis. Plenum, New York (1981)
7. Pawley, J.: The development of field-emission scanning electron microscopy for imaging biological surfaces. Scanning **19**, 324–336 (1997)
8. Tanaka, K., Mitsushima, A., Kashima, Y., Osatake, H.: A new high resolution scanning electron microscope and its application to biological materials. In: Proceedings of the 11th International Congress On Electron Microscopy, Kyoto, pp. 2097–2100 (1986)
9. Liu, J., Cowley, J.M.: High resolution SEM in a STEM instrument. Scanning Microsc. **2**, 65–81 (1988)
10. Howie, A.: Recent developments in secondary electron imaging. J. Microsc. **180**, 192–203 (1995)
11. Zhu, Y., Inada, H., Nakamura, K., Wall, J.: Imaging single atoms using secondary electrons with an aberration-corrected electron microscope. Nat. Mater. **8**, 808–812 (2009)
12. Inada, H., Su, D., Egerton, R.F., Konno, M., Wu, L., Ciston, J., Wall, J., Zhu, Y.: Atomic imaging using secondary electrons in a scanning transmission electron microscope: experimental observations and possible mechanisms. Ultramicroscopy **111**(7), 865–876 (2011). doi:10.1016/j.ultramic.2010.10.002. Invited articles for the special issue in honor of John Spence
13. Joy, D.C.: Beam interactions, contrast, and resolution in the SEM. J. Microsc. **136**, 241–258 (1984)
14. Reimer, L.: Scanning Electron Microscopy, 2nd edn. Springer, New York (1998)

Scanning Electron Microscopy and Secondary-Electron Imaging Microscopy

▶ Scanning Electron Microscopy

Scanning Force Microscopy in Liquids

▶ AFM in Liquids

Scanning Kelvin Probe Force Microscopy

▶ Kelvin Probe Force Microscopy

Scanning Near-Field Optical Microscopy

Achim Hartschuh
Department Chemie und CeNS,
Ludwig-Maximilians-Universität München,
Munich, Germany

Synonyms

Near-field scanning optical microscopy (NSOM)

Definition

Scanning near-field optical microscopy (SNOM) is a microscopic technique for nanostructure investigation that achieves sub-wavelength spatial resolution by exploiting short-ranged interactions between a sharply pointed probe and the sample mediated by evanescent waves. In general, the resolution of SNOM is determined by the lateral probe dimensions and the probe-sample distance. Images are obtained by raster-scanning the probe with respect to the sample surface corresponding to other scanning-probe techniques. As in conventional optical microscopy, the contrast mechanism can be combined with a broad range of spectroscopic techniques to study different sample properties, such as chemical structure and composition, local stress, electromagnetic field distributions, and the dynamics of excited states.

Introduction

Optical microscopy forms the basis of most of the natural sciences. In particular, life sciences have benefited from the fascinating possibility to study smallest structures and processes in living cells and tissue. Optical techniques feature extremely high detection sensitivity reaching single molecule sensitivity in fluorescence, Raman scattering and absorption spectroscopy. Besides the direct visualization, chemically specific information is obtained through Raman spectroscopy.

The resolution of conventional optical microscopes, however, is limited by diffraction, a consequence of the wave nature of light, to about half the wavelength. Concepts extending optical microscopy down to nanometer length scales below the diffraction-limit are distinguished into far-field and near-field techniques. Far-field techniques rely on the detection of propagating waves at distances from the source larger than the wavelength, while near-field techniques exploit short ranged evanescent waves.

Scanning near-field optical microscopy, initiated by pioneering work of Pohl, Lewis and others in the late 1980s and the beginning of 1990s gave access to nanoscale resolution for the first time. The history of near-field optics is reviewed in [1]. In addition numerous review articles and books exist describing fundamentals and applications (see e.g., [2–4]).

This entry introduces first the key physical principles beginning with the role of evanescent and propagating waves, and the loss of spatial information upon light propagation. Concepts of near-field detection are shown using different pointed probes. The next sections describe the experimental realization and present several applications of SNOM. The outlook addresses future prospects of SNOM and remaining challenges.

Key Principles and Concepts

Near-field optics has its origin in the effort of overcoming the diffraction limit of optical imaging. The physical origin of this limit is sketched in the following starting with the distinction between propagating waves that form the optical far-field of a radiation source and their evanescent counterpart that dominate the optical near-field. A powerful tool to describe wave propagation is the so-called angular spectrum representation of fields expressing the electromagnetic field E in the detector plane at z as the superposition of harmonic plane waves of the form $exp\,(i\vec{k}\vec{r} - i\omega t)$ with amplitudes $\bar{E}(k_x, k_y, z = 0)$ emanating from the source plane at $z = 0$ [2].

$$E(x,y,z) = \iint_{-\infty}^{+\infty} \bar{E}(k_x, k_y, z = 0) e^{i(k_x x + k_y y)} e^{\pm i k_z z} dk_x dk_y \tag{1}$$

The wave vector $\vec{k}$ describing the propagation direction of the wave is represented by its components $\vec{k} = (k_x, k_y, k_z)$ while its length is fixed by the wavelength of light λ and the refractive index of the medium n through $\left|\vec{k}\right| = \sqrt{k_x^2 + k_y^2 + k_z^2} = 2\pi n/\lambda$. In Eq. 1, the time dependence of the fields has been omitted for clarity. For simplicity the following discussion is limited to the x-z-plane and $n = 1$ such that $k_z = \sqrt{4\pi^2/\lambda^2 - k_x^2}$. In Eq. 1 the term $e^{\pm i k_z z}$ controls the propagation of the associated wave: For $k_x \le 2\pi/\lambda$ the component k_z is real and the corresponding wave with amplitude $\bar{E}(k_x, z = 0)$ propagates along the z-axis oscillating with $e^{-ik_z z}$. If $k_x > 2\pi/\lambda$ the component k_z becomes complex and $e^{-|k_z z|}$ describes an exponential decay of the associated wave that is therefore evanescent. As a result, only waves with $k_x \le 2\pi/\lambda$ can

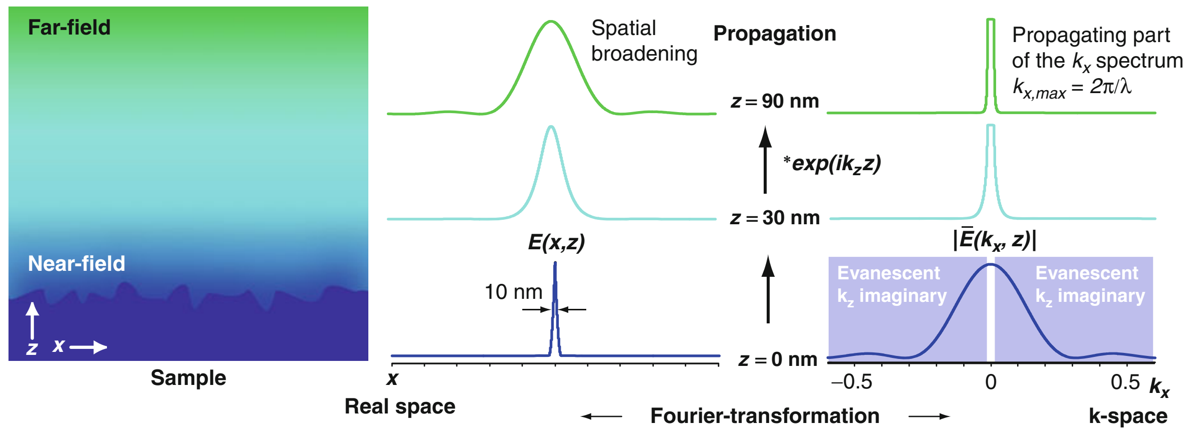

Scanning Near-Field Optical Microscopy, Fig. 1 Scheme illustrating the propagation of waves and the loss of spatial information. Initial field distribution $E(x, z = 0)$ at a 10-nm wide source in the x-z-plane (*center*) and corresponding angular spectrum $|\bar{E}(k_x, z = 0)|$ (*right*). Near the source the spectrum contains both evanescent and propagating waves. Upper panels illustrate the evolution of the fields at $z = 30$ nm and $z = 90$ nm distance for a source wavelength of $\lambda = 500$ nm in vacuum. Only waves with $k_x \leq 2\pi/\lambda$ propagate. Evanescent waves decay exponentially following $e^{-|k_z|z}$. The decay of high spatial frequencies leads to spatial broadening and loss of spatial information in the far-field

propagate and contribute to the field far from the source forming the far-field. Figure 1 schematically illustrates this behavior: In the center, the electric field $E(x, z)$ emanating from a narrow sub-wavelength source at $z = 0$ is shown together with its angular spectrum $\bar{E}(k_x, z = 0)$ calculated by the inverse of Eq. 1. The wave amplitudes $\bar{E}$ result from the Fourier-transformation of E with respect to the spatial coordinate x. As for the correlation between time and frequency domain, where a short optical pulse requires a broad frequency spectrum, a sharp field distribution requires a broad spectrum of spatial frequencies k_x.

Since only waves with limited spatial frequencies can propagate, the spectral width rapidly decreases with increasing distance from the source z leading to fast broadening of the electric field distribution in real space. In other words, propagation corresponds to low-pass filtering with frequency limit $k_{x,\,\max} = 2\pi/\lambda$. The far-field thus contains limited spatial frequencies equivalent to limited spatial information. To overcome this limitation different near-field concepts have been developed that are outlined in the following.

The key concept of SNOM is the probing of the sample near-field that contains the evanescent waves using a sharply pointed probe. Since evanescent waves decay rapidly for increasing distance to the source, the probe needs to be in close proximity to the sample. Waves with large k_x components that carry high spatial information decay most rapidly following $e^{-|k_z|z}$ as can be seen from Fig. 1. Hence the spatial resolution obtained in an SNOM experiment drops fast with increasing tip-sample distance z. As for other scanning probe techniques that exploit short-ranged interactions, such as atomic force and scanning tunneling microscopy, AFM and STM, respectively, the lateral resolution is also determined by the lateral dimension of the probe. Two conceptually different types of probes can be distinguished: The first confines and samples electromagnetic fields using an aperture with sub-wavelength diameter (Fig. 2a). The second exploits the antenna concept that couples locally enhanced near-fields to propagating waves and vice versa (Fig. 2b–d). The two types, termed aperture and antenna probe, respectively, are illustrated in the following.

Aperture Probes

Aperture probes confine light by squeezing it through a sub-wavelength hole (Fig. 2a). This approach, termed aperture-SNOM, provides an enormous flexibility regarding signal formation. Different operation modes can be used that are capable of local sample excitation and/or local light collection. Depending on which step of the experiment exploits near-field interactions to obtain sub-wavelength resolution, aperture-SNOM can be implemented in excitation ①, collection ② and excitation-collection ③ mode (Fig. 2a).

The original scheme was proposed by Synge in 1928. He suggested to use a strong light source behind

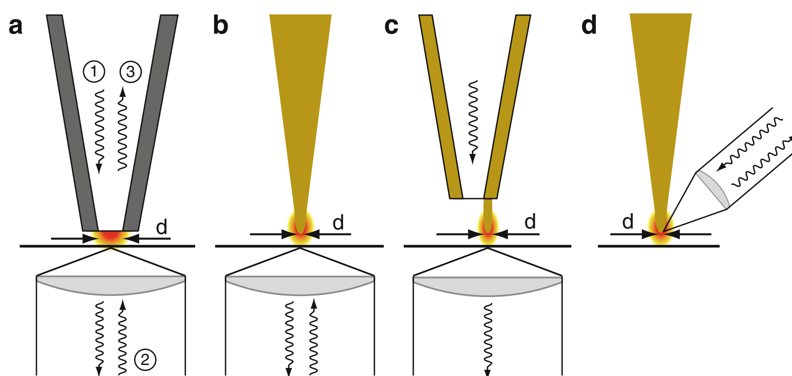

Scanning Near-Field Optical Microscopy, Fig. 2 Schematics of the most common SNOM probes and configurations: (**a**) Aperture probes are utilized in different modes: Near-field excitation – far-field collection ①, far-field excitation – near-field collection ② and near-field excitation – collection mode ③. (**b**) Tip-enhanced near-field optical microscopy (TENOM) using local field enhancement at a sharp metal antenna probe upon far-field excitation. (**c**) Tip-on-aperture (TOA) probe using local field enhancement at an antenna probe that is excited in the near-field of an aperture probe. (**d**) Scattering-SNOM (s-SNOM) based on far-field illumination and detection of local scattering at a sharp antenna probe. The label *d* indicates the structural parameter that determines the achievable spatial resolution

a thin, opaque metal film with a 100-nm diameter hole in it as a very small light source. In 1984, two groups adopted this scheme and presented the first experimental realizations in the optical regime [1]. The aperture was formed at the apex of a sharply pointed transparent probe tip coated with metal. Raster-scanning the probe was made possible by the scanning technology developed in the context of scanning tunneling microscopy (STM). In Fig. 3a, a scanning electron microscopy (SEM) image of an aperture probe consisting of a metal-coated tapered glass fiber is shown. At the front surface a well-defined aperture with diameter of 70 nm is seen.

Analytical expressions for the electric field distribution in a sub-wavelength aperture in a metallic screen were already presented in 1944 and 1950 by Bethe and Bouwkamp. Numerical simulations for metal-coated tapered fiber probes show that strong fields pointing in axial direction occur at the rim due to local field-enhancement by the metal coating (see Fig. 4). The center of the aperture is dominated by a weaker horizontal component [2]. The optical field distribution can be determined experimentally by raster-scanning single fluorescent molecules that act as point-like dipoles across the aperture while recording the fluorescence intensity [5] (see section "Fluorescence Microscopy" and Fig. 3).

Tapered aperture probes suffer from low light transmission due to the cut-off of propagating wave-guide modes. For probe diameters below the cut-off diameter only evanescent waves remain and the intensity decays exponentially toward the aperture (Fig. 2c, d). Probe designs, therefore, aim at maximizing the cone angle that determines the distance between aperture and cut-off diameter. Hollow-cantilever probes feature relatively large cone-angles as compared to fiber-based probes (Fig. 2b). On the other hand, the input power needs to be limited because of the damage threshold of the metal coating in case of fiber-based probes. Due to the limited transmission and the skin-depth of the optical fields on the order of several tens of nanometers, most aperture-SNOM measurements are carried out with apertures of 50–100 nm.

Antenna Probes

Antenna probes act as transmitter and receiver coupling locally enhanced near-fields to propagating waves and vice versa (Fig. 2b–d) [8]. To distinguish this approach from the earlier implementations based on apertures, it is also termed apertureless-SNOM or a-SNOM. Antenna probes can be used in two different techniques: (1) Scattering type microscopy [9, 10], also termed scattering-SNOM or s-SNOM, in which the tip locally perturbs the fields near a sample surface. The response to this perturbation is detected in the far-field at the frequency of the incident light corresponding to elastic scattering (Fig. 2d). (2) Tip-enhanced near-field optical microscopy (TENOM) in which locally enhanced fields at laser-illuminated metal structures are used to increase the spectroscopic response of the system at frequencies different from

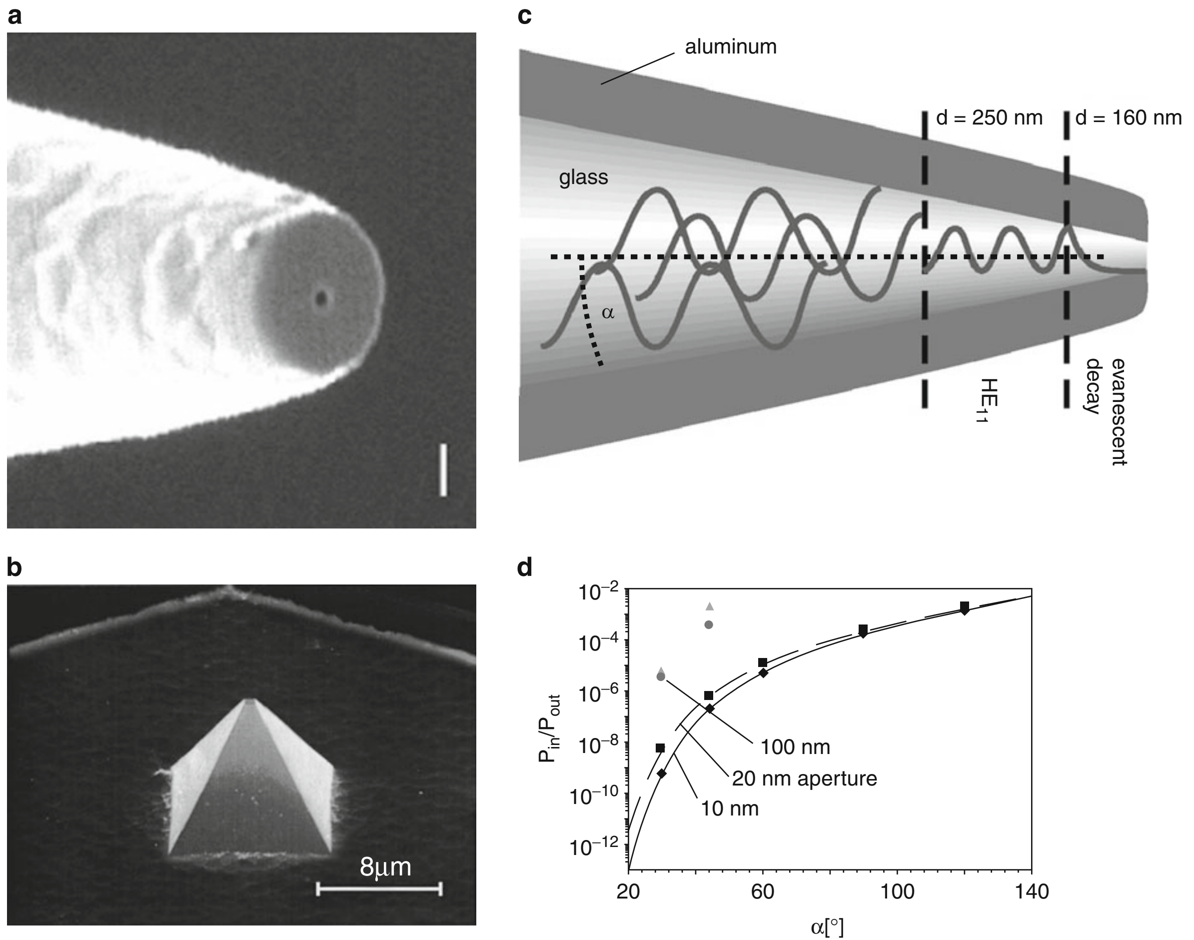

Scanning Near-Field Optical Microscopy, Fig. 3 (**a**) Scanning-electron microscopy (SEM) image of an aperture probe formed by a metal-coated tapered fiber with an aperture diameter of 70 nm (scale bar 200 nm) (Reprinted with permission from Veerman et al. [5]. Copyright 1999, John Wiley and Sons) (**b**) SEM image of a metallic hollow aperture probe microfabricated on a Si cantilever. The aperture diameter is about 130 nm (Reprinted with permission from Mihalcea et al. [6]. Copyright 1996, American Institute of Physics) (**c**) Schematic of the mode propagation in a tapered aperture probe. For probe diameters below the cut-off diameter, here $d = 160$ nm, the intensity decays exponentially toward the aperture. (**d**) Transmission of tapered probes determined as the ratio of input versus output power P_{in}/P_{out} as a function of the cone angle α defined in (**c**). For smaller cone angles, the distance between cut-off and aperture increases leading to extremely low transmission (**c** and **d**) (Reprinted with permission from Hecht et al. [7]. Copyright 2000, American Institute of Physics)

that of the incident light [8, 11] (Fig. 2b, c). The flexibility of this technique allows the study of a variety of spectroscopic signals including Raman scattering (tip-enhanced Raman spectroscopy (TERS)), and fluorescence as well as time-resolved measurements. In the following, the signal formation in the case of optical antennas is sketched.

Elastic scattering signal. The near-field interaction can be treated within a simplified model in which the tip is replaced by a polarizable sphere. Due to the antenna properties of the tip, laser excitation with incident fiel E_i creates a dominating dipole oriented along the tip axis in z-direction normal to the sample surface. This dipole induces a mirror dipole in the sample depending on its dielectric properties. The mirror dipole's field, decreasing with the third power of distance, interacts with the tip dipole. Solving the system of electrostatic equations that describes the multiple interaction between tip and mirror dipoles neglecting retardation yields an effective polarizability of the coupled tip-sample system which fully expresses the influence of the sample.

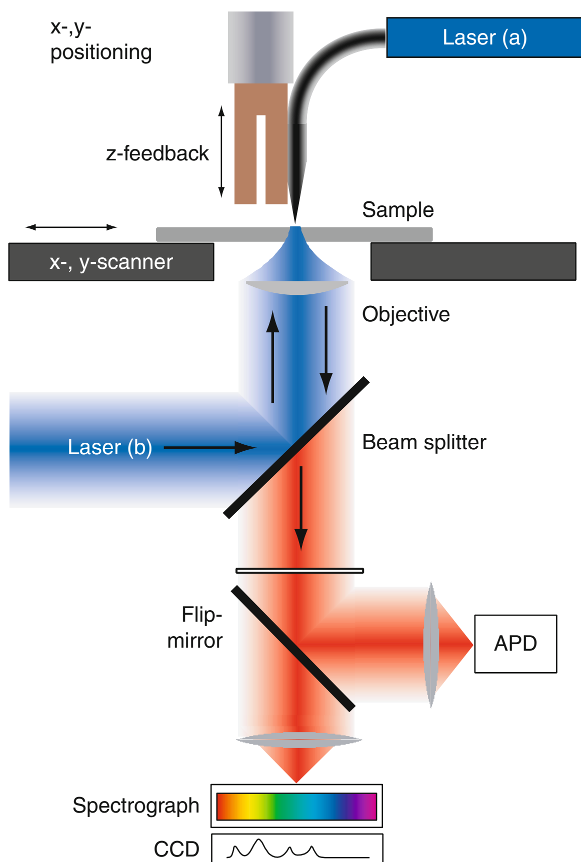

Scanning Near-Field Optical Microscopy, Fig. 4 Schematic of an experimental setup applicable to aperture-probe SNOM (laser (**a**), excitation mode) and TENOM (laser (**b**)) in case of transparent samples. In the case of TENOM the fiber probe would be replaced by an optical antenna, for example, an etched metal wire. The probe tip is positioned in the focus of the microscope objective by piezo-electric actuators. The sample is raster-scanned using a closed-loop *x*-*y*-scanner while both laser and probe position remain fixed. The tip-sample distance is controlled using a tuning-fork shear-force feedback scheme. The optical signal is collected by the objective and detected either by a highly sensitive avalanche photodiode (APD) or energetically resolved using a spectrograph and a CCD

$$\alpha_{\mathrm{eff}} = \left(\frac{(\alpha\,(1+\beta)\;/\;1-(\alpha\beta)}{(16\pi\,(\alpha+z)^3)} \right) \quad (2)$$

The scattered field can then be calculated from $E_s \propto \alpha_{\mathrm{eff}} E_i$ reflecting the short-ranged interaction required for sub-diffraction resolution. Since the laser illuminates a greater part of the tip and the sample, elimination of background-scattering contributions is crucial. Efficient background suppression can be achieved by demodulating the detected intensity signal at higher harmonics of the tapping mode frequency (see section "Instrumentation"). Besides the amplitude of the scattered field, its phase can be retrieved using interferometric heterodyne detection [9].

Raman scattering signal. In the case of Raman scattering, the total signal depends on the product of the excitation and emission rates $k^{\mathrm{ex}}(\lambda^{\mathrm{ex}})\,k^{\mathrm{rad}}(\lambda^{\mathrm{rad}})$. As a consequence, the total signal enhancement scales with the fourth power of the field enhancement for small differences between the excitation λ^{ex} and emission wavelength λ^{rad} and assuming that the field enhancement at the tip does not depend sensitively on the wavelength.

$$M_{\mathrm{Raman}} = \frac{k_{\mathrm{tip}}^{\mathrm{ex}}}{k_0^{\mathrm{ex}}} \cdot \frac{k_{\mathrm{tip}}^{\mathrm{rad}}}{k_0^{\mathrm{rad}}} \approx f^4 \quad (3)$$

The factor f measures the ratio between tip-enhanced E_{tip} and non-enhanced electric field E_0 in the absence of the tip. For the general case of surface-enhanced Raman scattering (SERS), Raman enhancement factors are reported reaching up to 12 orders of magnitude for particular multiple particle configurations involving interstitial sites between particles or outside sharp surface protrusions. Since the signal scales with the fourth power, already moderate field enhancement, predicted for a single spherical particle to be in the range of $f = 10–100$ is sufficient for substantial signal enhancement.

Fluorescence signal. The fluorescence intensity depends on the excitation rate k^{ex} and the quantum yield η denoting the fraction of transitions from excited state to ground state that give rise to an emitted photon. The quantum yield is expressed in terms of the radiative rate k^{rad} and the non-radiative rate k^{nonrad} through $\eta = k^{\mathrm{rad}}/(k^{\mathrm{rad}} + k^{\mathrm{nonrad}})$. Accordingly, the fluorescence enhancement due to the presence of the metal tip can be written as

$$M_{\mathrm{Flu}} = \left(\frac{E_{\mathrm{tip}}}{E_0}\right)^2 \left(\frac{\eta_{\mathrm{tip}}}{\eta_0}\right) = f^2 \left(\frac{\eta_{\mathrm{tip}}}{\eta_0}\right). \quad (4)$$

Here, it is assumed that the system is excited far from saturation. From Eq. 4 it is clear that TENOM works most efficiently for samples with small fluorescence quantum yield η_0 such as semiconducting single-walled carbon nanotubes [11]. For highly fluorescent samples such as dye molecules, the quantum yield η_0 is already close to unity and cannot be enhanced further.

Because of the small separation between emitter and metal tip required for high spatial resolution, non-radiative transfer of energy from the electronically excited state to the metal followed by non-radiative dissipation in the metal has to be taken into account. This process represents an additional competing non-radiative relaxation channel and reduces the number of detected fluorescence photons. Metal-induced fluorescence quenching can also be exploited for image contrast formation (see e.g., [12]). In this case M_{Flu} in Eq. 4 becomes smaller than unity.

While the theory of energy transfer between molecules and flat metal interfaces is well understood in the framework of phenomenological classical theory, nanometer-sized objects are more difficult to quantify [2]. Tip- and particle-induced radiative rate enhancement and quenching has been studied in literature both experimentally and theoretically. Experiments on model systems formed by single dipole emitters such as molecules and semiconductor nanocrystals and spherical metal particles revealed a distance-dependent interplay between competing enhancement and quenching processes. While semiconducting tips cause less efficient quenching, they also provided weaker enhancement because of their lower conductivity at optical frequencies.

Polarization and angular-resolved detection of the fluorescence signal of single emitters demonstrated that the fluorescence rate enhancement provided by the optical antenna also results in a spatial redistribution of the emission [13]. The same redistribution can be expected to occur for tip-enhanced Raman scattering. The spatial distribution of the enhanced electric field follows approximately the outer dimensions of the tip apex. Since the signal enhancement scales with higher orders of field enhancement, the optical resolution can surpass the size of the tip [11]. Stronger fields and field confinement are observed for so-called gap modes formed by metal tips on top of metal substrates.

The scheme depicted in Fig. 2b shows that in addition to the signal resulting from the near-field tip–sample interaction the confocal far-field signal contribution is detected, representing a background. This background originates from a diffraction-limited sample volume that is far larger than the volume probed in the near-field. The near-field signal has to compete with this background, and strong enhancement is required to obtain clear image contrast. This requirement is relaxed in case of low-dimensional sample structures such as spatially isolated molecules or one-dimensional nanostructures [11]. The near-field signal to background ratio can be improved by exploiting the non-linear optical response of sample and tip. Examples include two-photon excitation of fluorescence using a metal tip antenna and the application of the four-wave mixing signal of a metal particle dimer as local excitation source.

Instrumentation

Near-field optical microscopy exploits short-ranged near-field interactions between sample and probe. SNOM instruments thus require a mechanism for tip-sample distance control working on the scale of nanometers. Typical implementations utilize other non-optical short-ranged probe–sample interactions such as force or tunneling current used for topography measurements in AFM and STM, respectively. During image acquisition by raster-scanning the sample with respect to the tip, optical and topographic data are thus obtained simultaneously. Due to the strong tip-sample distance dependence of the near-field signal, cross-talk from topographic variations is possible that can lead to artifacts in the optical contrast. Tip-sample distance curves need to be measured to prove unequivocally the near-field origin of the observed image contrast. Since the optical signal results from a single sample spot only, SNOM instruments are often based on a confocal laser scanning optical microscope equipped with sensitive photodetectors.

Scattering-SNOM is often implemented with intermittent-contact-mode AFM in which the tip-sample distance is modulated sinusoidally at frequencies typically in the range of 10–500 kHz. The elastically scattered laser light intensity is demodulated by the tapping-mode frequency using lock-in detection for background suppression.

Since Raman and fluorescence signals are typically weak requiring longer acquisition times, signal demodulation is more challenging. In the case of single-photon counting time-tagging can be used to retrieve the signal phase with respect to the tapping oscillation. While this can be applied to single-color experiments, spectrum acquisition using CCD cameras in combination with spectrometers is not feasible at typical tapping frequencies.

In most aperture-SNOM and TENOM experiments, the tip-sample distance is kept constant by either using STM, contact/non-contact AFM, or shear-force feedback. Sensitive piezoelectric tuning-fork detection schemes operating at small interaction forces have been developed and are used for fragile fiber and antenna probes [2].

Probe Fabrication

The near-field probe forms the crucial part of an SNOM setup since both optical and topographic signals are determined by its short-ranged interactions with the sample. Instrument development, therefore, focuses mainly on the design of optimized tip concepts and tip geometries as well as on fabrication procedures for sharp and well-defined probes with high reproducibility. These continuing efforts benefit substantially from improving capabilities regarding nanostructuring and nanocharacterization, using, for example, focused ion beam milling (FIB) or electron beam lithography (EBL).

Aperture Probes

Optical fiber probes. Sharply pointed optical fiber probes were the first to provide sub-diffraction spatial resolution and are widely used as nanoscale light sources, light collectors or scatterers (Fig. 2a and 3a). Probe fabrication requires a number of steps starting with the formation of a tapered optical fiber. Typically two different methods are used. Chemical etching of a bare glass fiber dipped into hydro-fluoric (HF) acid yields sharp tips [4, 7]. The surface tension of the liquid forms a meniscus at the interface between air, glass, and acid. A taper is formed due to the variation of the contact angle at the meniscus, while the fiber is etched and its diameter decreased. Chemical etching allows reproducible production of larger quantities of probes in a single step. A specific advantage is that the taper angle can be tuned and optical probes with correspondingly large transmission coefficient can be produced.

The second method combines local heating using a CO_2 laser or a filament and subsequent pulling until the fiber is split apart. The resulting tip shapes depend heavily on the temperature and the timing of the heating and pulling, as well as on the dimensions of the heated area. The pulling method has the advantage of producing tapers with very smooth surfaces, which positively influences the quality of the evaporated metal layer. Etched probes, on the other hand, typically feature rough surfaces. Pulled fibers, however, have small cone angles and thus reduced optical transmission as well as flat end-faces limiting the minimum aperture size.

The aperture is formed during the evaporation of aluminum. Since the evaporation takes place under an angle slightly from behind, the deposition rate of metal at the apex is much smaller than on the sides. This geometrical shadowing effect leads to the self-aligned formation of an aperture at the apex.

The ideal aperture probe should have a perfectly flat end face to position a sample as close as possible into the near-field of the aperture. Conventional probes generally have a roughness determined by the grain size of the aluminum coating, which is around 20 nm at best. Due to the corrugated end face the distance between aperture and sample increases, which lowers the optical resolution and decreases the light intensity on the sample. Furthermore, these grains often obscure the aperture, which makes the probe ill-defined and not suited for quantitative measurements [4, 5, 7]. Subsequent focused ion beam (FIB) milling can be used to form high definition SNOM probes with well-defined end face (Fig. 3).

Microfabricated cantilevered probes. Hollow-pyramid cantilevered probes can be batch-fabricated with large taper angles. Lithographic patterning of an oxidized silicon wafer first defines the position of the aperture and the dimensions of the cantilever beam by structuring the oxide layer [6]. Anisotropic etching of the exposed silicon with buffered HF forms a pyramidal groove for the tip and trenches for the cantilever beam. After removing the oxide layer on the opposite side anisotropic etching is used to open a small aperture in the pyramidal groove. A 120-nm chromium layer is deposited on the back side forming the hollow pyramidal tip that is finally freed by isotropic reactive ion etching.

Si_3N_4 tips can be fabricated by dry etching in a CF_4 plasma and covering with thin aluminum films. Microfabricated probes based on quartz tips attached to silicon cantilevers have also been reported [2, 7]. First sharp quartz tips were produced in hydrofluoric acid followed by coating with thin films of aluminum and silicon nitride. Reactive ion etching was then used to selectively remove the silicon nitride from the tip apex, while the remaining film served as a mask for wet-etching of the protruding aluminum in a standard

Al-etching solution, leaving a small aperture on the apex of the tip. For light coupling, windows are etched into the backside of the levers at the position of the tip.

Microfabricated tips provide several advantages over fiber-based probes. The mechanical stability is typically increased and often sufficient to measure also in contact AFM mode without destroying the tip. A reproducible fabrication of the tips leads to a well-defined aperture shape. Large taper angles of around 70° shift the position of the mode cut-off closer to the aperture, resulting in higher transmission.

Antenna Probes

Sharp metal tip are fabricated in a single step by simple electrochemical etching. In the case of gold, pulsed or continuous etching in hydro-chloric acid (HCL) or a mixture of HCL and ethanol routinely yields tips with diameters in the range of 30–50 nm. These tips can either be used in shear-force mode after gluing to the prong of a tuning-fork or in STM-mode. Silicon or silicon nitride cantilevered probes can be coated by a thin metal film through evaporation. Subsequent nanostructuring by FIB-milling can be used to optimize tip parameters.

Tip-on-aperture probes need to be fabricated in a series of sequential steps [14] (Fig. 2c). First, a fiber-based aperture probe is produced on which a well-defined end face is formed by FIB-milling. In the second step, a nanoscale tip is grown by electron beam–induced deposition of carbon. Next, the carbon tip is coated by a thin layer of chromium to improve adhesion of an aluminum layer evaporated during the final preparation step. Since the length of the tip can be controlled during electron beam deposition, TOA probes can be tailored to provide optimum antenna enhancement for a chosen wavelength [8].

Applications in Nanoscience

The energy of light quanta – photons – is in the range of electronic and vibrational excitations of materials. These excitations are directly determined by the chemical and structural composition of matter. Optical spectroscopy, the energy-resolved probing of the material response to light exposure, thus provides a wealth of information on the static and dynamical properties of materials. Combining spectroscopy with near-field microscopy is particularly interesting since spectral information is obtained spatially resolved at the nanoscale. In the following several representative examples covering different material responses including fluorescence, Raman scattering and elastic scattering are briefly illustrated to highlight the capabilities of SNOM techniques.

Fluorescence Microscopy

Fluorescence measurements were among the first applications of SNOM. In these experiments, aperture-based probes were used to probe highly fluorescent dye-molecules on substrates. Aluminum-coated fiber tips were used for excitation while the fluorescence was collected in the far-field by a high-numerical aperture objective. A molecule is excited only if the optical electric field is polarized parallel to its transition dipole moment. The resulting fluorescence patterns rendered by a single molecule with known orientation can thus be used to visualize the local electric field distribution at the probe. Conversely, the molecular orientation can be determined for known field distributions. These experiments showed that the strongest electrical fields do not occur in the center of the aperture, but at the rims of the metal coating. This is the result of local field enhancement at the thin metal rim (see section "Aperture Probes"). Two lobes with strong fields oriented in axial direction occur located on opposite sides of the aperture in the direction of the polarization of the incident linearly polarized light. Molecules with a transition dipole moment oriented parallel to the tip axis are excited efficiently by these field components as can be seen in Fig. 5 [5]. Rotating the polarization of the incident linearly polarized light is seen to rotate the resulting double lobe pattern that indicates the area with strongest fields.

Fluorescence measurements typically do not require high excitation densities and in many cases, the small light transmission of aperture probes represents no major drawback. In fact, fluorescence imaging of single dye molecules with 32 nm spatial resolution has been demonstrated using a microfabricated cantilevered glass tip covered with a 60-nm-thick aluminum film. Due to the thickness of the virtually opaque film, possible contributions from surface plasmons propagating on the outside of the film have been discussed [4]. Examples of fluorescence microscopy measurements based on aperture probes also include, for example, studies of single nuclear pore

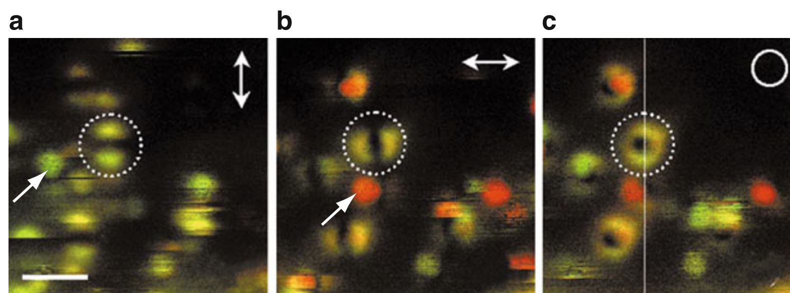

Scanning Near-Field Optical Microscopy, Fig. 5 Series of three successive aperture-SNOM fluorescence images of the same area (1.2 × 1.2 μm) of a sample of dye molecules embedded in a thin transparent polymer film. The excitation polarization, measured in the far-field, was rotated from linear vertical (**a**) to linear horizontal (**b**) and then changed to circular polarization (**c**). Circular features marked by arrows result from molecules with transition dipole moments oriented parallel to the sample plane. The double lobe structure marked by the dashed circle results from a molecule with perpendicularly oriented transition dipole moment. This molecule senses the strong electrical fields that occur at the rim of the metal aperture at positions determined by the far-field polarization. Scale bar 300 nm (Reprinted with permission from Veerman et al. [5]. Copyright 1999, John Wiley and Sons)

complexes and the kinetics of protein transport under physiological conditions.

Optical antennas have been used for a variety of samples and materials including photosynthetic proteins, polymers, semiconductor quantum dots, and carbon nano-tubes [11]. The image contrast was based on local field enhancement provided by the tip. The spatial resolution achieved in these experiments was essentially determined by the diameter of the tip and ranged between 10 and 20 nm. Imaging can be combined with local spectroscopy to visualize emission energies on the nanoscale. Single-molecule experiments revealed the field distribution at the tip-antenna in analogy to the discussion made above for aperture probes [14].

While most of the reported studies were exploiting local signal enhancement, distance-dependent metal-induced quenching of fluorescence can also be used for high-resolution imaging. This approach provides sub 10 nm spatial resolution and has been applied to single fluorescent organic molecules and inorganic semiconductor nanorods (see e.g., [12]). In these experiments, the spectrally integrated fluorescence signal was demodulated by the tapping-mode frequency of the AFM cantilever after recording photon-arrival times.

Raman Microscopy

Raman scattering probes the unique vibrational spectrum of a sample and directly reflects its chemical composition and molecular structure. A main drawback of Raman scattering is the extremely low scattering cross-section which is typically 10–14 orders of magnitude smaller than the cross-section of fluorescence in the case of organic molecules. Raman measurements thus require higher laser intensities and in many cases the low transmission of aperture probes prohibits their application. The signal enhancement provided by the antenna tip in TENOM is substantial for the detection of nanoscale sample volumina. In the following, a review of selected examples is given to illustrate the possibilities of tip-enhanced Raman scattering (TERS) (see e.g., [11, 15]).

In Fig. 6, simultaneous near-field Raman and topographic imaging of individual single-walled carbon nanotubes is shown. The optical image in (a) reflects the intensity of the G’ band, a particular Raman-active vibrational mode of carbon nanotubes. The optical resolution obtained in this experiment was about 25 nm as can be seen from the width of the peaks in the cross-section in Fig. 6c.

The strong fields required for sufficient enhancement of the Raman scattering signal can cause laser-induced decomposition and photochemical reactions in the presence of oxygen. TERS of single electronically resonant molecules has been demonstrated for ultra-high vacuum conditions. A review focusing on single-molecule surface- and tip-enhanced Raman scattering can be found in [15].

Elastic Scattering Microscopy

Elastic scattering SNOM probes the dielectric properties of the sample and has been used from the visible to the microwave regime of the electromagnetic

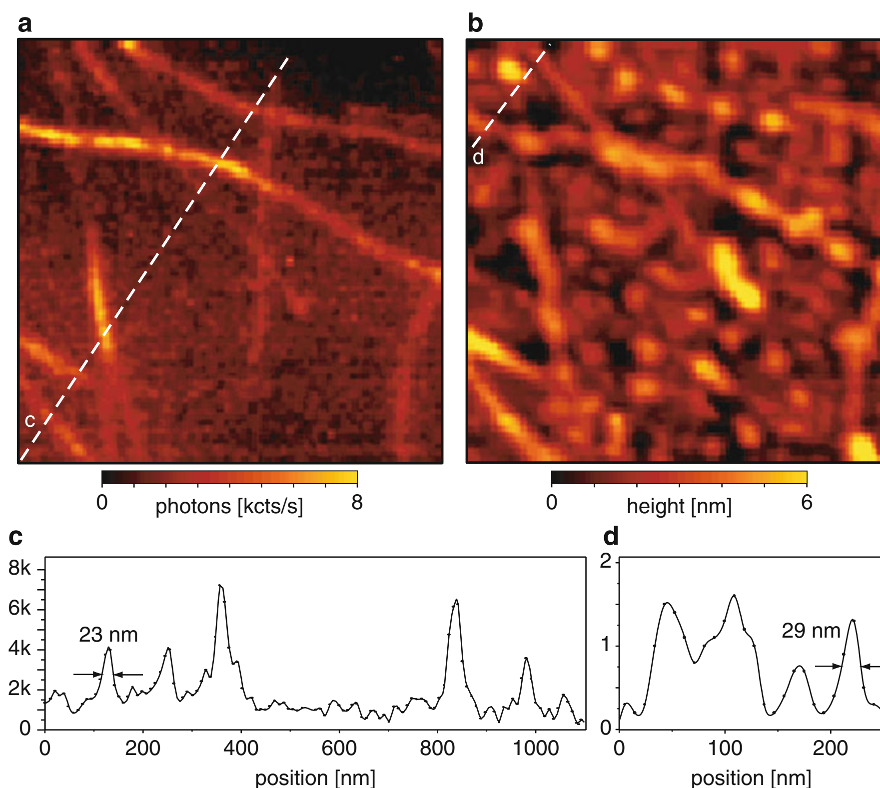

Scanning Near-Field Optical Microscopy, Fig. 6 Tip-enhanced Raman spectroscopy (TERS) of single-walled carbon nanotubes on glass. Simultaneous near-field Raman image (**a**) and topographic image (**b**). Scan area 1 × 1 μm^2. The Raman image is acquired by detecting the intensity of the G' band upon laser excitation at 633 nm. No Raman scattering signal is detected from humidity-related circular features present in the topographic image. (**c**) Cross-section taken along the *dashed line* in the Raman image indicating a spatial resolution around 25 nm. (**d**) Cross-section taken along the indicated dashed line in the topographic image. Vertical units are photon counts per second for c and nanometer for d (Reprinted with permission from Hartschuh et al. [16]. Copyright 2003, American Physical Society)

spectrum. Reviews of the fundamentals of the technique and representative applications can be found in [9, 10]. The majority of s-SNOM experiments have been reported for the IR to THz spectral range. Applications include detection of the Mott-transition in nanodomains, mapping of the doping concentration in semiconductors, surface characterization with a sensitivity of a single monolayer, strain-field mapping, and infrared spectroscopy of a single virus.

As an example nanoscale infrared spectroscopic near-field mapping of single nano-transistors is shown in Fig. 7. A cantilevered metallized Si-tip operating in tapping-mode with an oscillation frequency of 300 kHz and an amplitude of about 60 nm was used [17]. The data clearly demonstrates the potential of s-SNOM for infrared spectroscopic recognition of materials within individual semiconductor nanodevices.

Based on the antenna approach, s-SNOM typically provides 10–20 nm spatial resolution determined by the diameter of the tip-apex. In most of the s-SNOM experiments to date, monochromatic laser sources were used. Since only the optical response at this frequency is determined, the acquisition of scattering spectra or spectrally resolved images can only be obtained sequentially with a series of image scans at different laser frequencies. New developments exploiting broadband NIR laser sources aim at overcoming this limitation, and recently obtained a spectral bandwidth exceeding 400 cm^{-1}.

Plasmonics and Photonic Nanostructures

SNOM plays a vital role in the field of plasmonics which deals with the study of optical phenomena related to the electromagnetic response of metals

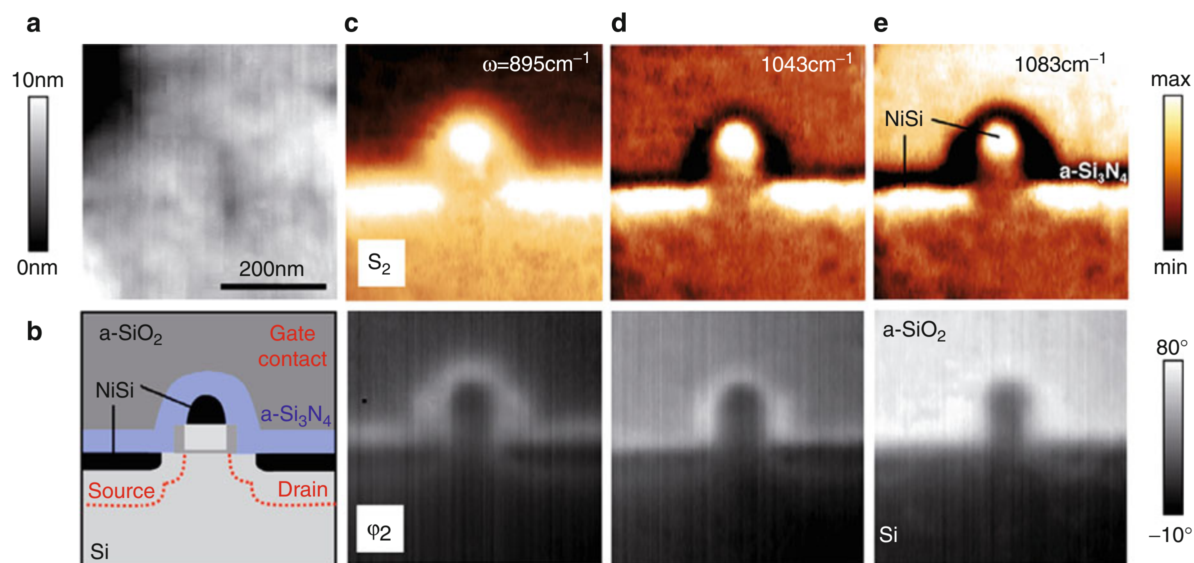

Scanning Near-Field Optical Microscopy, Fig. 7 Material-specific mapping of transistor components using s-SNOM: Cross-sectional images of a single transistor fabricated at the 65 nm technology node. (**a**) Topography. (**b**) Sketch of the transistor with materials indicated. (**c**–**e**) Near-field amplitude and phase images recorded at three different laser frequencies. Amorphous SiO_2 and Si_3N_4 render reversed optical contrast and are clearly distinguished. A spatial resolution better than 20 nm has been achieved (Reprinted with permission from Huber et al. [17]. Copyright 2010, IOP)

[18]. Near-field optical probes are particularly important for two reasons. First, they provide a means to locally excite propagating surface plasmon polaritons (SPPs) in metal films, a process that is not possible in case of propagating light waves because of momentum (k-vector) mismatch. The broad k-spectrum associated with the near-field of the probe contains sufficient bandwidth for efficient SPP-excitation (see Fig. 1). Second, near-field probes can be used simultaneously to convert SPPs back into propagating waves, thereby probing the local distribution of electromagnetic fields in the vicinity of metallic nanostructures. As an example, the near-field associated with SPPs has been visualized along gold nanowires using an aperture probe in collection mode (see Fig. 2a, [4]). This approach is also termed photon scanning tunneling microscopy (PSTM) to illustrate the analogy between evanescent electromagnetic waves and the corresponding exponentially decaying electron wavefunctions within the tunnel barrier of an STM. PSTM has been widely used to spatially resolve light wave propagation also in dielectric photonic nanostructures [4].

Besides the visualization of static field distributions, optical spectroscopy also allows for the study of their temporal evolution and the propagation of pulses. Figure 8 illustrates ultrafast and phase-sensitive imaging of the plasmon propagation in a metallic waveguide by PSTM [19]. In this case the near-field microscope uses an aperture-probe in collection mode and incorporates a Mach-Zehnder–type interferometer enabling heterodyne time-resolved detection.

Scattering-SNOM with antenna tips has been used extensively to study localized surface plasmon polaritons (LSPP) in different metal nanostructures. By varying the laser excitation frequency near-field optical imaging allowed for distinguishing higher order plasmonic resonances [20].

Perspectives

During the last 25 years SNOM has demonstrated its capabilities for sub-wavelength optical imaging and spectroscopy of surfaces and sub-surface features. The strength of SNOM results from its enormous flexibility with respect to sample types as well as measurement configurations and in particular, from its combination with a broad range of spectroscopic techniques. Ongoing developments aim at increasing antenna efficiencies and new aperture-type schemes [18]. In addition, the combination of nano-optical approaches and ultrafast laser technique is explored

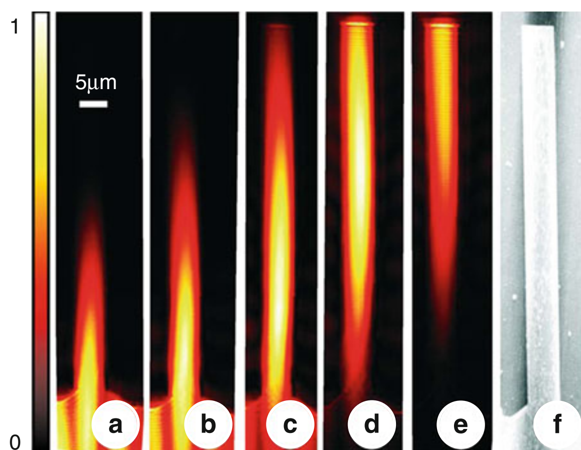

Scanning Near-Field Optical Microscopy, Fig. 8 Phase-sensitive and ultrafast near-field microscopy of a surface plasmon polariton (SPP) waveguide. The local electric field is collected by an aperture-probe and detected interferometrically in a Mach-Zehnder–type configuration. (**a**–**e**) Normalized amplitude information of the SPP wavepacket E-field. Succeeding frames are new scans of the probe. In between the frames the delay line is lengthened to 14.4 μm. Therefore, the time between two frames is 48 fs. The scan frame is $15 \times 110\ \mu m^2$, scan lines run from *top* to *bottom*. (**f**) Topography of the SPP waveguide obtained by shear-force feedback (Reprinted with permission from Sandtke et al. [19]. Copyright 2008, American Institute of Physics)

to achieve enhanced light localization and the control of optical near-fields on the time scale of few optical cycles.

Cross-References

▶ Atomic Force Microscopy
▶ Confocal Laser Scanning Microscopy
▶ Light Localization for Nano-optical Devices
▶ Nanostructures for Photonics
▶ Scanning Tunneling Microscopy

References

1. Novotny, L.: The history of near-field optics. In: Wolf, E. (ed.) Progress in Optics, vol. 50, pp. 137–184. Elsevier, Amsterdam (2007)
2. Novotny, L., Hecht, B.: Principles of Nano-optics. Cambridge, Cambridge University Press (2006)
3. Kawata, S., Shalaev, V.M. (eds.): Advances in Nano-Optics and Nano-Photonics Tip Enhancement. Elsevier, Amsterdam (2007)
4. Kawata, S., Shalaev, V.M. (ed.): Handbook of Microscopy for Nanotechnology. Kluwer, Dordrecht (2006)
5. Veerman, J.A., Garcia-Parajo, M.F., Kuipers, L., van Hulst, N.F.: Single molecule mapping of the optical field distribution of probes for near-field microscopy. J. Microsc. **194**, 477–482 (1999)
6. Mihalcea, C., Scholz, W., Werner, S., Münster, S., Oesterschulze, E., Kassing, R.: Multipurpose sensor tips for scanning near-field microscopy. Appl. Phys. Lett. **68**, 3531–3533 (1996)
7. Hecht, B., Sick, B., Wild, U.P., Deckert, V., Zenobi, R., Martin, O.J.F., Pohl, D.E.: Scanning near-field optical microscopy with aperture probes: fundamentals and applications. J. Chem. Phys. **112**, 7761–7774 (2000)
8. Bharadwaj, P., Deutsch, B., Novotny, L.: Optical antennas. Adv. Opt. Photon. **1**, 438–483 (2009)
9. Keilmann, F., Hillenbrand, R.: Near-field microscopy by elastic light scattering from a tip. Phil. Trans. R. Soc. Lond. **A 362**, 787–805 (2004)
10. Bründermann, E., Havenith, M.: SNIM: scanning near-field infrared microscopy. Annu Rep Prog Chem Sect. C Phys. Chem. **104**, 235–255 (2008)
11. Hartschuh, A.: Tip-enhanced near-field optical microscopy. Angew. Chem. Int. Ed. **47**, 8178–8198 (2008)
12. Ma, Z., Gerton, J.M., Wade, L.A., Quake, S.R.: Fluorescence near-field microscopy of DNA at sub-10 nm resolution. Phys. Rev. Lett. **97**, 260801–260804 (2006)
13. Taminniau, T.H., Stefani, F.D., Segerink, F.B., van Hulst, N.F.: Optical antennas direct single-molecule emission. Nat. Photon. **2**, 234–237 (2008)
14. Frey, H.G., Witt, S., Felderer, K., Guckenberger, R.: High resolution imaging of single fluorescent molecules with the optical near field of a metal tip. Phys. Rev. Lett. **93**, 200801–200804 (2004)
15. Pettinger, B.: Single-molecule surface-and tip-enhanced Raman spectroscopy. Mol. Phys. **108**, 2039–2059 (2010)
16. Hartschuh, A., Sánchez, E.J., Xie, X.S., Novotny, L.: High-resolution nearfield Raman microscopy of single-walled carbon nanotubes. Phys. Rev. Lett. **90**, 095503–4 (2003)
17. Huber, A.J., Wittenborn, J., Hillenbrand, R.: Infrared spectroscopic near-field mapping of single nanotransistors. Nanotechnology 21, 235702–6 (2010)
18. Schuller, J.A., Barnard, E.S., Cai, W., Jun, Y.C., White, S. W., Brongersma, M.L.: Plasmonics for extreme light concentration and manipulation. Nat. Mater. **9**, 193–204 (2010)
19. Sandtke, M., Engelen, R.J.P., Schoenmaker, H., Attema, I., Dekker, H., Cerjak, I., Korterik, J.P., Segerink, F.B., Kuipers, L.: Novel instrument for surface plasmon polariton tracking in space and time. Rev. Sci. Instrum. **79**, 013704–10 (2008)
20. Dorfmüller, J., Vogelgesang, R., Khunsin, W., Rockstuhl, C., Etrich, C., Kern, K.: Plasmonic nanowire antennas: experiment, simulation, and theory. Nano. Lett. **10**(9), 3596–3603 (2010)

Scanning Probe Microscopy

▶ Atomic Force Microscopy

tip [20]. These techniques have the potential for profiling the surface temperature distribution of devices with a spatial resolution of a fraction of the IR wavelength. Similarly, the spatial resolution of Raman thermograph or thermal reflectance techniques can potentially be improved with either a near-field or far-field nanoscopy technique.

Cross-References

▶ Atomic Force Microscopy
▶ Carbon-Nanotubes
▶ Graphene
▶ Scanning Tunneling Microscopy
▶ Thermal Conductivity and Phonon Transport

References

1. Williams, C.C., Wickramasinghe, H.K.: Scanning thermal profiler. Appl. Phys. Lett. **49**, 1587–1589 (1986)
2. Majumdar, A., Carrejo, J.P., Lai, J.: Thermal imaging using the atomic force microscope. Appl. Phys. Lett. **62**, 2501–2503 (1993)
3. Pollock, H.M., Hammiche, A.: Micro-thermal analysis: techniques and applications. J. Phys. D Appl. Phys. **34**, R23–R53 (2001)
4. Majumdar, A.: Scanning thermal microscopy. Annu. Rev. Mater. Sci. **29**, 505–585 (1999)
5. Aigouy, L., Tessier, G., Mortier, M., Charlot, B.: Scanning thermal imaging of microelectronic circuits with a fluorescent nanoprobe. Appl. Phys. Lett. **87**, 3 (2005)
6. Shi, L., Majumdar, A.: Thermal transport mechanisms at nanoscale point contacts. J. Heat Trans-T. ASME. **124**, 329–337 (2002)
7. Incropera, F.P., Dewitt, D.P., Bergman, T.L., Lavine, A.S.: Fundamentals of Heat and Mass Transfer. John Wiley, Hoboken (2007)
8. Chen, G.: Nanoscale Energy Transport and Conversion: A Parallel Treatment of Electrons, Molecules, Phonons, and Photons. Oxford University Press, New York (2005)
9. Chung, J., Kim, K., Hwang, G., Kwon, O., Jung, S., Lee, J., Lee, J.W., Kim, G.T.: Quantitative temperature measurement of an electrically heated carbon nanotube using the null-point method. Rev. Sci. Instrum. 81, 5 (2010)
10. Jo, I., Hsu, I.-K., Lee, Y.J., Sadeghi, M.M., Kim, S., Cronin, S., Tutuc, E., Banerjee, S.K., Yao, Z., Shi, L.: Low-frequency acoustic phonon temperature distribution in electrically biased graphene. Nano Lett. (2010). doi:10.1021/nl102858c
11. Cahill, D.G., Goodson, K., Majumdar, A.: Thermometry and thermal transport in micro/nanoscale solid-state devices and structures. J. Heat Trans-T. ASME. **124**, 223–241 (2002)
12. Tien, C.L., Majumdar, A., Gerner, F.M.: Microscale Energy Transport. Taylor & Francis, Washington, DC (1998)
13. Berciaud, S., Han, M.Y., Mak, K.F., Brus, L.E., Kim, P., Heinz, T.F.: Electron and optical phonon temperatures in electrically biased graphene. Phys. Rev. Lett. **104**, 227401 (2010)
14. Chae, D.H., Krauss, B., von Klitzing, K., Smet, J.H.: Hot phonons in an electrically biased graphene constriction. Nano Lett. **10**, 466–471 (2010)
15. Nakabeppu, O., Suzuki, T.: Microscale temperature measurement by scanning thermal microscopy. J. Therm. Anal. Calorim. **69**, 727–737 (2002)
16. Price, D.M., Reading, M., Hammiche, A., Pollock, H.M.: Micro-thermal analysis: scanning thermal microscopy and localised thermal analysis. Int. J. Pharm. **192**, 85–96 (1999)
17. Kwon, O., Shi, L., Majumdar, A.: Scanning thermal wave microscopy (STWM). J. Heat Trans-T. ASME. **125**, 156–163 (2003)
18. Dunn, R.C.: Near field scanning optical microscopy. Chem. Rev. **99**, 2891–2928 (1999)
19. Hell, S.W.: Far-field optical nanoscopy. Science **316**, 1153–1158 (2007)
20. De Wilde, Y., Formanek, F., Carminati, R., Gralak, B., Lemoine, P.A., Joulain, K., Mulet, J.P., Chen, Y., Greffet, J.J.: Thermal radiation scanning tunneling microscopy. Nature **444**, 740–743 (2006)

Scanning Thermal Profiler

▶ Scanning Thermal Microscopy

Scanning Tunneling Microscopy

Ada Della Pia and Giovanni Costantini
Department of Chemistry, The University of Warwick, Coventry, UK

Definition

A scanning tunneling microscope (STM) is a device for imaging surfaces with atomic resolution. In STM, a sharp metallic tip is scanned over a conductive sample at distances of a few Å while applying a voltage between them. The resulting tunneling current depends exponentially on the tip-sample separation and can be used for generating two-dimensional maps of the surface topography. The tunneling current also depends on the sample electronic density of states, thereby allowing to analyze the electronic properties of surfaces with sub-nm lateral resolution.

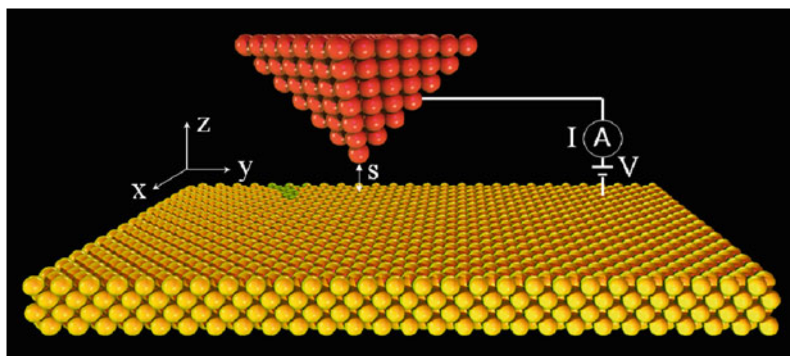

Scanning Tunneling Microscopy, Fig. 1 Schematic representation of a STM. Tip and sample are held at a distance *s* of a few Å and a bias voltage *V* is applied between them. The resulting tunneling current *I* is recorded while the tip is moved across the surface. The coordinate system is also shown

Overview and Definitions

If two electrodes are held a few Å apart and a bias voltage is applied between them, a current flows even though they are not in contact, due to the quantum mechanical process of electron tunneling. This current depends exponentially on the electrode separation, and even minute, subatomic variations produce measurable current changes. In 1981, Gerd Binnig and Heinrich Rohrer at IBM in Zürich realized that this phenomenon can be used to build a microscope with ultrahigh spatial resolution [1], if one of the electrodes is shaped as a sharp tip and is scanned across the surface of the other (Fig. 1). Moreover, since the tunneling current depends also on the electronic properties of the electrodes, this microscope has the ability to probe the electronic density of states of surfaces at the atomic scale. A few years later, Don Eigler at IBM in Almaden, showed that, due to the extremely localized interaction between tip and sample, it is also possible to use this instrument to manipulate individual atoms, to position them at arbitrary locations and therefore to build artificial structures atom-by-atom [2]. This remarkable achievement brought to reality the visionary predictions made by Richard Feynman in his famous 1959 lecture "*There's plenty of room at the bottom*" [3].

The construction of this instrument, dubbed the scanning tunneling microscope (STM), was awarded the 1986 Nobel Prize in Physics and has since then revolutionized contemporary science and technology. The STM has enabled individual atoms and molecules to be imaged, probed, and handled with an unprecedented precision, thereby essentially contributing to our current understanding of the world at the nanoscale. Together with its offspring, the atomic force microscope (AFM) [▶ AFM], the STM is considered as the main innovation behind the birth of nanotechnology.

This entry will start with a discussion of the physical principles and processes at the heart of STM in section Theory of Tunneling. This will be followed by a description of the experimental setup and the technical requirements needed for actually operating such a microscope in section Experimental Setup. Section STM Imaging is dedicated to the most frequent use of STM, namely imaging of surfaces, while section Scanning Tunneling Spectroscopy gives a brief account of the spectroscopic capabilities of this instrument. Finally, section Applications discusses several applications and possible uses of STM.

Theory of Tunneling

Figure 2 is a schematic representation of the energy landscape experienced by an electron when moving along the *z* axis of a metallic-substrate/insulator/metallic-tip tunneling junction. The following treatment can easily be extended to include also semiconducting tips or samples. Usually, the tip and the sample are not made of the same material and therefore have different work functions, ϕ_T and ϕ_S, respectively. At equilibrium, the two metals have a common Fermi level, resulting in an electric field being established across the gap region and in different local vacuum levels, depending on the difference $\phi_T - \phi_S$ (Fig. 2a). Since the work functions in metals are of the order of several eV, the potential in the gap region is typically much higher than the thermal energy kT and thus acts as a barrier for sample and tip electrons. A classical particle cannot penetrate into any region where the potential energy is greater than its total energy because this requires a negative kinetic energy. However, this is

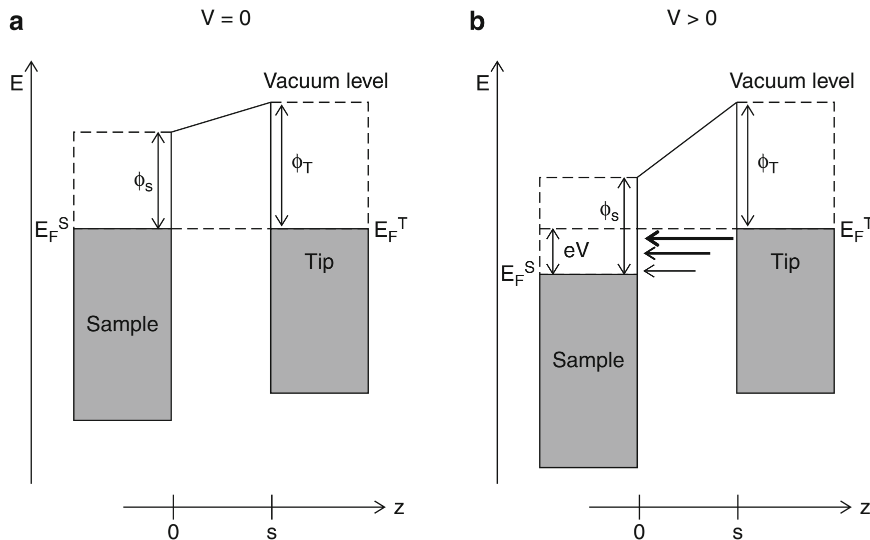

Scanning Tunneling Microscopy, Fig. 2 Energy potential perpendicular to the surface plane for an electron in a tip-vacuum-sample junction. z is the surface normal direction, and s is the tip-sample distance. The gray boxes represent the Fermi–Dirac distribution at 0 K. $\phi_{T,S}$ and $E_F^{T,S}$ are the work functions and the Fermi levels of tip and sample, respectively. (**a**) Tip and sample in electrical equilibrium: a trapezoidal potential barrier is created. (**b**) Positive sample voltage V: the electrons tunnel from occupied states of the tip into unoccupied states of the sample. The thickness and the length of the *arrows* indicate the exponentially decreasing probability that an electron with the corresponding energy tunnels through the barrier

possible for electrons which, being quantum mechanical objects, are described by delocalized wave functions. This phenomenon goes under the name of *quantum tunneling*. In an unpolarized tip-sample junction the electrons can tunnel from the tip to the sample and vice versa, but there is no net tunneling current. On the contrary, if a voltage V is applied between sample and tip, the Fermi level of the former is shifted by $-eV$ and a net tunneling current occurs, whose direction depends on the sign of V (Fig. 2b). Here the convention is adopted to take the tip as a reference since experimentally the voltage is often applied to the sample while the tip is grounded. If V is the bias voltage, the energy for an electron in the sample will change by $-eV$, that is, it will decrease for positive values of V.

The tunneling current can be evaluated by following the time-dependent perturbation approach developed by Bardeen [4, 5]. The basic idea is to consider the isolated sample and tip as the unperturbed system described by the stationary Schrödinger equations:

$$(\mathcal{T} + \mathcal{U}_S)\psi_\mu = E_\mu \psi_\mu \tag{1}$$

and

$$(\mathcal{T} + \mathcal{U}_T)\chi_\nu = E_\nu \chi_\nu, \tag{2}$$

where $\mathcal{T}$ is the electron kinetic energy. The electron potentials $\mathcal{U}_S$ and $\mathcal{U}_T$ and the unperturbed wavefunctions ψ_μ and χ_ν are nonzero only in the sample and in the tip, respectively. Based on this, it can be shown [5] that the transition probability per unit time $w_{\mu\nu}$ of an electron from the sample state ψ_μ to the tip state χ_ν is given by Fermi's golden rule:

$$w_{\mu\nu} = \frac{2\pi}{\hbar}|M_{\mu\nu}|^2 \delta(E_\nu - E_\mu), \tag{3}$$

where the matrix element is:

$$M_{\mu\nu} = \int \chi_\nu^*(\vec{x})\mathcal{U}_T(\vec{x})\psi_\mu(\vec{x})d^3\vec{x}. \tag{4}$$

The δ function in Eq. (3) implies that the electrons can tunnel only between levels with equal energy, that is, (3) accounts only for an *elastic tunneling* process. The case of an inelastic tunneling process will be considered in section Scanning Tunneling Spectroscopy. The total current is obtained by summing $w_{\mu\nu}$ over all the possible tip and sample states and by multiplying this by the electron charge e. The sum over

the states can be changed into an energy integral by considering the density of states (DOS) $\rho(E) : \Sigma \to 2\int f(\varepsilon)\rho(\varepsilon)d\varepsilon$, where the factor 2 accounts for the spin degeneracy while f, the Fermi–Dirac distribution function, takes into consideration Pauli's exclusion principle and the electronic state population at finite temperatures.

As a consequence, the total current can be written as:

$$I = \frac{4\pi e}{\hbar}\int_{-\infty}^{\infty}\left[f_T(E_F^T - eV + \varepsilon) - f_S(E_F^S + \varepsilon)\right] \times \rho_T(E_F^T - eV + \varepsilon)\rho_S(E_F^S + \varepsilon)|M|^2 d\varepsilon, \quad (5)$$

where E_F is the Fermi energy and the indexes T and S refer to the tip and the sample, respectively. Equation 5 already accounts for the movement of electrons from the sample to the tip and vice versa.

Several approximations can be made to simplify Eq. 5 and to obtain a manageable analytical expression for I. If the thermal energy $k_BT << eV$, the Fermi–Dirac distributions can be approximated by step functions and the total current reduces to:

$$I = \frac{4\pi e}{\hbar}\int_{0}^{eV}\rho_T(E_F^T - eV + \varepsilon)\rho_S(E_F^S + \varepsilon)|M|^2 d\varepsilon. \quad (6)$$

(Note that Eq. 6 is valid only for $V > 0$. For $V < 0$ the integrand remains identical but the integration limits become $-e|V|$ and 0). In this case, only electrons with an energy differing from E_F by less than eV can participate to the tunneling current. This can be directly seen in Fig. 2b for the case of positive sample bias: tip electrons whose energy is lower than $E_F^T - eV$ cannot move because of Pauli's exclusion principle, while there are no electrons at energies higher than E_F^T. The main problem in determining expression (5) is, however, the calculation of the tunneling matrix elements M since this requires a knowledge of the sample and the tip wave functions, which can be very complicated. On the other hand, for relatively small bias voltages (in the ± 2 V range), Lang [6] showed that a satisfactory approximation of $|M|^2$ is given by a simple one-dimensional WKB tunneling probability. In the WKB approximation [7], the probability $D(\varepsilon)$ that an electron with energy ε tunnels through a potential barrier $U(z)$ of arbitrary shape is expressed as:

$$D(\varepsilon) = \exp\left\{-\frac{2}{\hbar}\int_0^s \left[2m(U(z) - \varepsilon)\right]^{\frac{1}{2}}dz\right\}. \quad (7)$$

This semiclassical approximation is applicable if ($\varepsilon << U$) which is generally satisfied in the case of metal samples where the work function is of the order of several eV. In order to obtain a simple analytical expression for D, the trapezoidal potential barrier of a biased tip-sample junction (see Fig. 2b) is further approximated with a square barrier of average height $\phi_{eff}(V) = (\phi_T + \phi_S + eV)/2$. By using this, the integral in Eq. 7 becomes:

$$D(\varepsilon, V, s) = \exp(-2ks), \quad (8)$$

where

$$k = \sqrt{\frac{2m}{\hbar^2}(\phi_{eff} - \varepsilon)}. \quad (9)$$

In order to evaluate k, it must be noted that electrons closest to the Fermi level experience the lowest potential barrier and are therefore characterized by an exponentially larger tunneling probability (see Fig. 2b). Thus, in a first approximation, it can be assumed that only these electrons contribute to the tunneling current which, for positive bias, is equivalent to set $\varepsilon \approx eV$ in (Eq. 9). Moreover, if the bias is much smaller than the work functions, eV can be neglected, resulting in

$$k \cong \frac{\sqrt{m(\phi_T + \phi_S)}}{\hbar} = 5.1\sqrt{\frac{\phi_T + \phi_S}{2}}\ \mathrm{nm}^{-1}, \quad (10)$$

where the work functions are expressed in eV. Using typical numbers for metallic work functions, the numerical value of the inverse decay length $2k$ in Eq. 8 becomes of the order of 20 nm^{-1}. Therefore, variations in s of 1 Å correspond to one order of magnitude changes in the tunneling probability and, as a consequence, in the measured current. This very high sensitivity provides the STM with a vertical resolution in the picometer regime. The lateral resolution of STM depends on how different points of the tip contribute to the total tunneling current. By considering a spherical tip shape with radius R, most of the current originates from the central position since this is closest to the surface. A point laterally displaced by Δx from the tip center is $\Delta z \approx \frac{\Delta x^2}{2R}$ further away from the substrate (higher order Δx terms are neglected in this

evaluation). As a consequence, with respect to the tip center, the corresponding tunneling probability is reduced by a factor:

$$\exp\left(-2k\frac{\Delta x^2}{2R}\right). \quad (11)$$

By considering a tip radius $R \approx 1$ nm, the current changes by one order of magnitude for variations $\Delta x = 3$ Å. The actual lateral resolution is typically smaller than this upper limit and can reach down to fractions of an Å. Its specific value however depends on the precise shape of the tip which is unknown a priori. These values, together with the vertical resolution discussed above, lie at the basis of the STM atomic imaging capabilities.

Finally, if the tunneling probability (Eq. 8) is substituted for the tunneling matrix $|M|^2$ in Eq. 6, the total tunneling current can be expressed as:

$$I = \frac{4\pi e}{\hbar}\int_0^{eV}\rho_T(E_F^T - eV + \varepsilon)\rho_S(E_F^S + \varepsilon)e^{-2ks}d\varepsilon. \quad (12)$$

Therefore, for a fixed lateral position of the tip above the sample, the tunneling current I depends on the tip-sample distance s, the applied voltage V and the tip and sample density of states ρ_T and ρ_S, respectively.

Experimental Setup

As seen in the previous section, variations of 1 Å in s induce changes in the tunneling probability of one order of magnitude. The exponential dependence in Eq. 8 is responsible for the ultimate spatial resolution of STM but places stringent constraints on the precision by which s must be controlled, as well as on the suppression of vibrational noise and thermal drift. Moreover, typical tunneling currents are in the 0.01–10 nA range, requiring high gain and low noise electronic components. The following subsections are dedicated to a general overview of technologies and methods used to meet these specifications.

Scanner and Coarse Positioner

The extremely fine movements of the tip relative to the sample required for operating an STM are realized by using piezoelectric (▶ Piezoresistivity) ceramic actuators (*scanners*) which expand or retract depending on the voltage difference applied to their ends. In a first approximation, the voltage-expansion relation can be considered as linear with a proportionality factor (piezo constant) usually of few nanometer/Volt. The main requirements for a good scanner are: high mechanical resonance frequencies, so as to minimize noise vibrations in the frequency region where the feedback electronics operates (see section Electronics and Control System); high scan speeds; high spatial resolution; decoupling between x, y, and z motions; minimal hysteresis and creep; and low thermal drift. Although several types of STM scanner have been developed, including the bar or tube tripod, the unimorph disk and the bimorph [8], the most frequently used is a single piezoelectric tube whose outer surface is divided into four electrode sections of equal area. By applying opposite voltages between the inner electrode and opposite sections of the outer electrode, the tube bends and a lateral displacement is obtained. The z motion is realized by polarizing with the same voltage the inner electrode in respect to all four outer electrodes. By applying several hundred Volts to the scanner, lateral scan widths up to 10 μm and vertical ones up to 1 μm can be obtained, while retaining typical lateral and vertical resolutions of 0.1 nm and 0.01 nm, respectively.

While scanning is typically done by one individual piezoelectric element, larger displacements up to several millimeters are needed to bring the tip in close proximity to the sample, to move it to different regions of the surface or to exchange samples or tips. These are achieved by mounting the scanner onto a coarse position device. Several designs have been developed to this aim including micrometric screws driven either manually or by a stepper motor, piezoelectric walkers like the louse used in the first STM [9] or the inchworm [10], magnetic walkers where the movement is obtained by applying voltage pulses to a coil with a permanent magnet inside and piezoelectric driven stick-slip motors, as the Besocke-beetle [11] or the Pan motor [12].

Electronics and Control System

The voltages driving the piezoelectric actuators and their temporal succession and duration are generated by an electronic control system. The electronics are also used to bias the tunneling junction, to record the tunneling current and to generate the STM images.

In most of the modern instruments, these tasks are digitally implemented by a computer interfaced with digital to analog (DAC) and analog to digital (ADC) converters. The tunneling current is amplified by a high gain I–V converter (10^8–10^{10} V/A) usually positioned in close proximity of the tip, so as to reduce possible sources of electronic interference. This signal is then acquired by an ADC and processed by the control system. DACs are used to apply the bias voltage (from a few mV to a few V) between tip and sample and, in conjunction with high voltage amplifiers, to polarize the piezo elements. A feedback loop is integrated into the control system and is activated during the frequently used *constant current* imaging mode (see section STM Imaging). By acting on the z motion of the scanner, the feedback varies s to keep the tunneling current constant. This is controlled by a proportional-integral and derivative (PID) filter whose parameters can be set by the operator. Finally, a lock-in amplifier is often used to improve the signal-to-noise ratio in scanning tunneling spectroscopy (STS) measurements (see section Scanning Tunneling Spectroscopy).

Tip

Sharp metal tips with a low aspect ratio are essential to optimize the resolution of the STM images and to minimize flexural vibrations of the tip, respectively. Ideally, in order to obtain atomically resolved topographies and accurate spectroscopic measurements, the tip should be terminated by a single atom. In this case, because of the strong dependence on the tip-sample separation (see section Theory of Tunneling), most of the tunneling current would originate from this last atom, whose position and local DOS would precisely determine the tunneling conditions. In practice, however, it is almost impossible to determine the exact atomic configuration of the tip and the actual current is often due to a number of different atoms. This is still compatible with good tunneling conditions as long as these atoms are sufficiently localized (in order to avoid "multiple tip effects") and their structural and chemical state remains constant during scanning.

The most commonly used methods to produce STM tips are to manually cut or to electrochemically etch thin wires of platinum-iridium and tungsten, respectively. These materials are chosen because of their hardness, in order to prevent tips becoming irreversible damaged after an accidental crash. Other metallic elements and even semiconductor materials have been used as tips for specific STM applications. Due to their chemical inertness, Pt-Ir tips are often used to scan in air on atomically flat surfaces without the need of any further processing. However, they typically have inconsistent radii, while etched W tips are characterized by a more reproducible shape. These latter have the drawback that a surface oxide up to 20 nm thick is formed during etching or exposure to air. For this reason, W tips are mostly used in ultrahigh vacuum (UHV) where the oxide layer can be removed through ion sputtering and annealing cycles. Prior to use, tips are often checked by optical microscopy, scanning electron microscopy (▶ SEM), and field ion microscopy or transmission electron microscopy (▶ TEM). The quality of a tip can be further improved during scanning by using "*tip forming*" procedures, including pulsing and controlled crashing into metal surfaces. These processes work because the desorption of adsorbed molecules or the coating with atoms of the metallic substrate can produce a more stable tip apex. If STM is performed in polar liquids (▶ EC-STM), electrochemical processes might generate Faradaic or non-Faradaic currents which can be of the same order of magnitude or even larger than the tunneling current. In order to minimize these effects, the tip, except for its very apex, must be coated with an insulating material.

Vibration Isolation

A low level of mechanical noise is an essential requirement for any type of scanning probe microscopy. For this reason, the core of a STM, where the tip-sample junction is located, is always equipped with one or several types of vibration damping systems. These can be stacks of metal plates separated by elastic spacers, suspension springs, or eddy current dampers composed of copper elements and permanent magnets. The low-frequency components of mechanical noise ($<$10 Hz), which are the most difficult to eliminate, are minimized by building a small and rigid STM with a high resonance frequency. Depending on the overall size and weight of the microscope, further noise damping strategies can be adopted. Smaller, typically ambient conditions STMs can be placed on metal or granite slabs suspended by springs or bungee cords or floating on pneumatic isolators. Sometimes, piezo-driven, feedback-controlled active vibration suppressors are also combined with passive systems. Larger

versions of pneumatic isolators and active damping are often used to float the frames and the chambers of big UHV STMs. The laboratory where a STM instrument is located also plays an essential role for its performance. Ground floor rooms are always preferred since they minimize low-frequency natural building oscillations, which can be very difficult to counteract. High-resolution instruments are sometimes placed on large concrete blocks which are separated from the rest of the laboratory floor and rest either on a sand bed, an elastomer barrier or on second-stage pneumatic isolators. Moreover, they are also often surrounded by an acoustically insulating box. All these systems essentially act as low-pass mechanical filters whose effectiveness improves with decreasing cutoff frequencies, that is, with increasing mass and decreasing rigidity. For this reason, the body of a STM is typically a relatively heavy block of metal and the frames, slabs, and vacuum chambers supporting or containing the microscope often have a considerable weight.

Setups for Different Environments and Temperatures

Different types of STMs have been developed that can operate in various environments such as air, inert atmosphere (N_2, Ar), vacuum, high pressure, liquid, or in an electrochemical cell. The core of the different instruments is essentially the same, although the experimental chambers and setups in which they are located can vary substantially. Ambient condition STMs are typically quite compact and rigid and do not need elaborated anti-vibrational mechanisms. On the other hand, since sound waves represent a major problem, atmospheric pressure STMs are usually contained in an acoustic enclosure. A STM operating in vacuum must be hosted in a chamber with vibration-free pumps (typically ionic pumps for UHV) and must be equipped with sophisticated sample and tip manipulation mechanisms. Such systems often also have an in situ surface preparation stage allowing the handling of samples without air exposure.

STM can be performed at high pressures (1–30 bar) by installing the microscope head into gas manifolds under conditions similar to those used in industrial catalytic processes. Also in this case, sample and tip manipulation and preparation stages are mandatory parts of the system. Since these types of studies are typically performed at elevated temperatures (up to 600 K) and in the presence of highly reactive gases, the metallic parts of the STM scanner and of the chamber are often gold plated, the volume of the STM chamber is kept as small as possible and the tip material is chosen to be inert toward the gases [13]. Moreover, low voltages are used for polarizing the piezos in order to avoid gas discharges at intermediate pressures (10^{-3}–10 mbar) and shields are added to protect the STM from the deposition of conductive materials which could create electrical shorts.

STM at the liquid/solid interface and electrochemical STM (EC-STM) (▶ EC-STM) need the tip and sample to be inside a liquid cell which, in turn, may be placed in a humidity-controlled atmosphere. In the case of low vapor pressure liquids, the STM can be simply operated under ambient conditions by dipping the tip into a liquid droplet deposited on the sample. A special coating must be applied to the tip when working with polar liquids (see section Tip).

STM can also be performed at different temperatures (in vacuum or controlled atmosphere chambers): variable temperature STM (VT-STM) able to cover the 5–700 K range, low temperature STM (LT-STM) operating at 77 K or 5 K and even milli-Kelvin STM instruments are currently available. A VT-STM is typically used to study thermally activated processes such as diffusion and growth, phase transitions, etc. These systems have sample heating and cooling stages which can be operated in a combined way so as to achieve a very precise temperature stabilization. Resistive heating is normally employed to increase the temperature, while both flow and bath cryostats with liquid nitrogen or helium as cryogenic fluids are used to reduce it. Continuous flow cryostats offer a high flexibility in temperature but are characterized by lower thermal stability, by inherent mechanical vibrations and do not easily attain temperatures below 20 K. Bath cryostats are more stable, are able to reach lower temperatures but are often also much bulkier (e.g., in order to limit the He consumption rate, a liquid He cryostat is actually a double-stage cryostat with an outer liquid nitrogen mantle). For most of these instruments the variable temperature capabilities refer to the possibility of choosing different (fixed) temperatures at which the microscope is run. However, few systems endowed with specific position tracking and drift compensating capabilities allow a “true” variable temperature operation where the same surface area can be imaged with atomic resolution while its temperature

is changed. LT-STMs are operated at a fixed temperature and are typically inserted inside double stage cryostats which significantly complicates the tip and sample access. However, these instruments are extremely stable with a very low thermal drift and are therefore the best choice for STS and manipulation experiments (see sections Scanning Tunneling Spectroscopy and Applications). Milli-Kelvin STMs enable temperatures to be reached where extremely interesting magnetic, quantum Hall physics and superconductivity phenomena occur. Moreover, the thermal broadening of electronic features is strongly reduced, which is required for high-resolution measurements. These systems operate based on the evaporative cooling of liquid ^{3}He to temperatures of about 300 mK or liquid ^{3}He and ^{4}He mixtures below 10 mK. The STM heads can be further placed inside large-bore superconducting magnets (up to 15 T), enabling the low temperature and high magnetic field conditions necessary to access superconductive phase transitions or to detect single spin flip processes.

STM Imaging

STM images are generated by recording the tunneling current as a function of the tip position while the tip is scanned across the sample surface. This can be done in two different ways which define the two main STM imaging modes:

- *Constant height mode*. The z section of the piezo scanner is kept fixed while the tip is moved over the substrate at a constant bias voltage (Fig. 3a). Variations of the tip-sample distance due to the surface topography produce a corresponding variation of the tunneling current which is recorded point-by-point and used to build the STM gray-level image. This mode is employed only in small areas of extremely flat surfaces, where the probability of crashing into protrusions such as steps or defects is relatively small. Very high scanning speeds can be used because of the absence of a feedback control.
- *Constant current mode*. While the x and y sections of the piezo scanner are used to laterally move the tip across the surface, the z section is driven by the electronic feedback so as to maintain a constant tunneling current (Fig. 3b). The corresponding z-voltage applied to the scanner (feedback signal) is recorded point-by-point and used to build the STM gray-level image. This mode can be employed for any type of surface topography and is therefore the most frequently used.

Since the constant height mode is applied to atomically flat surfaces with sub-Å height variations, the exponential $I - s$ relation derived from Eq. 12 can be approximated by a linear dependence. As a consequence, constant height STM images are a good representation of flat surfaces. On the other hand, for less planar substrates, one must use the constant current mode which directly reproduces the surface height due to the linear voltage-extension relation of piezoelectric materials. However, even constant current STM images are a reliable representation of the "true" surface topography only if the sample local DOS does not vary across the scanned area. If this is not the case, a constant current profile corresponds to a complex convolution of topographical and electronic features (see Eq. 12) which can be particularly relevant for surfaces covered with molecular adsorbates.

Scanning Tunneling Spectroscopy

Besides complicating the interpretation of STM images, the dependence of the tunneling current on the sample DOS also offers the unique opportunity of probing the electronic characteristics of surfaces with sub-nm spacial resolution. Having fixed the tip lateral position, the tunneling current I is a function of the applied bias voltage V and the tip-sample separation s only, the precise relation being established by Eq. 12. In a STS experiment, the relation between two of these three parameters is measured while the remaining one is kept constant (STS). $I(V)$ spectroscopy, where the tunneling current is measured as a function of the bias voltage for a constant tip-sample separation, is the most widely used technique because it provides indications about the DOS of the sample.

Due to the spatial localization of the tunneling current (see section Theory of Tunneling), STS enables the characterization of the electronic properties of individual atoms and molecules in relation to their structure, bonding and local environment. Moreover, STS can also be used to create 2D maps of the sample DOS with sub-nm resolution. Such measurements are particularly interesting for quantum confined

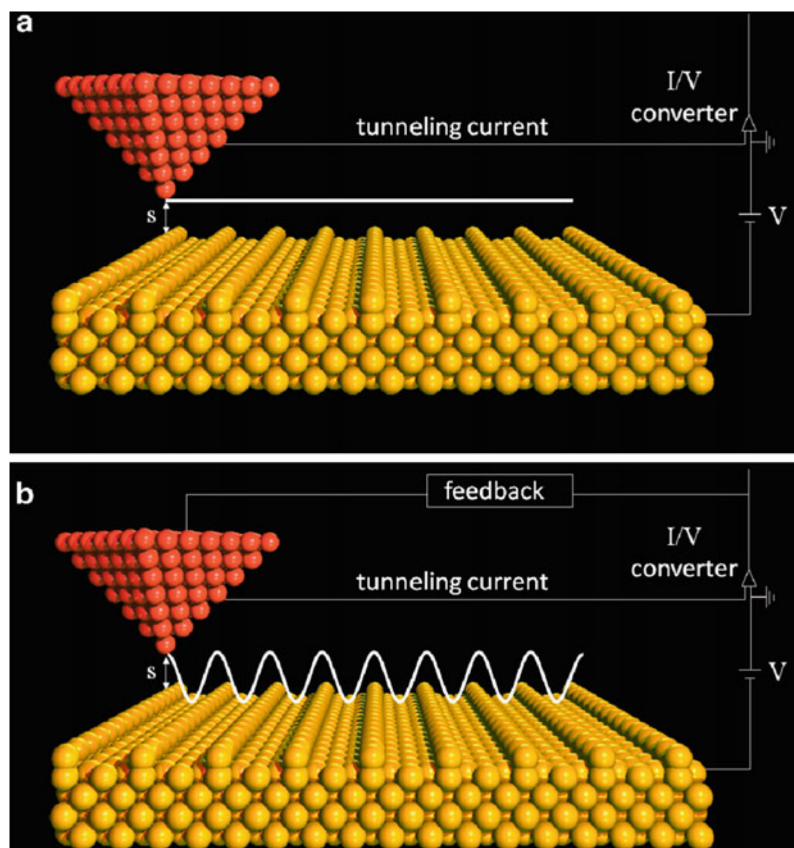

Scanning Tunneling Microscopy, Fig. 3 Schematic representation of (**a**) the constant height and (**b**) the constant current imaging modes, respectively. The *thick lines* represent the trajectory followed by the tip

electronic systems (e.g., quantum dots or quantum corrals) or for determining the shape of molecular orbitals [14] (*wavefunction mapping*). By changing the polarity of the bias voltage, STS gives access to both the occupied and the unoccupied states of the sample. In this sense, it is often considered as complementary to ultraviolet photoemission spectroscopy (UPS), inverse photoemission spectroscopy (IPS) and electron energy loss spectroscopy (EELS), where the signal is averaged over a large area of the surface (between 0.1 and 2 mm in diameter). On the other hand, STS does not provide direct chemical information and tip artifacts can strongly influence the spectroscopic data.

So far we have assumed that electrons conserve their energy during the tunneling process (see Eq. 3). However, electrons can also tunnel inelastically between the tip and the sample by exchanging energy and inducing the excitation of vibrational modes, spin-flips, magnons, plasmons, excitons, etc. These extra tunneling channels become available only above specific voltage thresholds since only beyond these values a part of the electron energy can be converted into the excitation. The additional inelastic pathways increase the overall tunneling probability and therefore show up as discrete step-like features in the tunneling conductivity or as slope changes in $I(V)$ curves. This technique is called inelastic electron tunneling spectroscopy (IETS) and benefits from the same spatial resolution as STM and STS. IETS has been used to measure vibrational modes of individual molecules, spin excitations of single magnetic atoms, collective plasmon excitations in 2D materials and magnons in ferromagnets.

A different way of detecting tunneling-induced molecular vibrations by means of a STM is to rely on their coupling with dynamical processes such as molecular motions. In particular, by measuring the frequency of molecular hopping events as a function of the applied bias voltage, it is possible to create so-called *action spectra* which reflect the vibrational spectrum of an individual molecule in a quantitative

manner [15]. Optical excitations can also be revealed in an alternative way by coupling the STM with a photon detection system able to collect and analyze the luminescence stimulated by inelastically tunneling electrons [16]. Such a setup has been used to characterize plasmon emission from metallic surfaces and luminescence from semiconductor quantum structures and adsorbed molecules.

Applications

Since the first STM images of the surfaces of $CaIrSn_4$ and Au [1] were published back in 1982, STM has been used to analyze a wide range of materials: clean and adsorbate covered metal surfaces, semiconductors, superconductors, thin insulating layers, small and large organic molecules, individual atoms, liquid-solid interfaces, magnetic layers and surfaces, quasicrystals, polymers, biomolecules, nanoclusters, and carbon nanotubes. Imaging is the most frequent application of STM used to determine the structural properties of substrates and their reconstructions, the presence of defects, sites of adsorption for adatoms and molecules and the symmetry and periodicity of adsorbate superstructures. Nevertheless, right from the beginning, it became clear that the ultimate spatial resolution of STM, in combination with its dependence on the electronic properties of tip and sample, could allow a much wider range of applications of this instrument. These include the characterization of surface electronic, vibrational, optical, and magnetic properties, the measurement of single molecule conductivities, and the study of dynamic processes. In the following, we will only touch upon some of the most frequent applications, without any presumption of being exhaustive.

Equation 12 shows that the tunneling current depends on the sample DOS close to the Fermi energy E_F. As a consequence, at a typical bias of a few Volts, it should be possible to image conductors, superconductors and small-gap or doped semiconductors but not molecules and insulating materials due to the vanishing DOS in the probed energy range (for most molecules the highest occupied and the lowest unoccupied orbitals are separated by an energy gap of several eV). However, the great majority of molecules adsorbed on metallic substrates can be easily imaged at moderate bias voltages. This is due to the formation of a metal-organic interface which can modify the molecular electronic properties leading to a broadening of the initial discrete energy levels, to a reduction of the gas-phase energy gap and even to the development of new states if covalent molecule-substrate bonds are established. All these effects contribute to the DOS at E_F and allow the imaging process. Regarding insulating materials, STM can only be done on films deposited onto conductive substrates if they are thin enough to allow the tunneling of electrons. These films are often used to electronically decouple organic adsorbates from metallic substrates.

The mechanism which allows the imaging of biomolecules such as DNA and proteins is currently still under debate [17]. As these molecules have a very large energy gap (5–7 eV) they can be considered as insulating materials and the current measured in STM experiments might be mediated by the thin water layer surrounding the molecules in air. Metalloproteins have also been imaged in their "natural" environment by using EC-STM (▶ EC-STM). Several reports have shown that when these redox active molecules are imaged under potentiostatic control, the tunneling current can be mediated by their metal redox-center, with enhanced conductivities measured for bias voltages close to the redox potential.

Although STM is a surface sensitive method, it can be also used to analyze buried interfaces and structures in cross-sectional STM (XSTM) [18]. The specific sample preparation in this technique requires brittle materials such as oxide samples or semiconductor wafers. A cross section of the structure to be analyzed is prepared by cleaving the sample and positioning the STM tip onto the exposed edge. In this way, various physical properties can be probed, including the morphology and abruptness of buried nanostructures and interfaces, the alloying in epitaxial layers, the spatial distribution of dopants and their electronic configuration and the band offsets in semiconductor heterojunctions. XSTM has also been used to study, in real time, the changes occurring in semiconductor quantum well laser devices under operating conditions.

STM can further be employed for tracking dynamic surface processes, provided that the corresponding characteristic times are longer than the acquisition time. By choosing optimized designs for the piezo scanners and the electronic feedback,

video-rate instruments have been developed able to record several tens of images per second and thereby to follow mobility and assembly processes in real time [19, 20].

When a tip with spin polarized electrons is used in STM, besides the parameters already indicated in Eq. 12, the local sample magnetization also influences the tunneling current. In fact, due to the different density of states at E_F of "spin-up" and "spin-down" electrons in magnetic materials, a spin polarized tip causes a tunnel magnetoresistance effect which results in a further contrast mechanism. This technique, called spin-polarized STM (SP-STM), has been used both in the presence and absence of an external magnetic field for detecting magnetic domain structures and boundaries in ferro- and antiferromagnetic materials, visualizing atomic-scale spin structures and determining spatially resolved spin-dependent DOS. An essential aspect of SP-STM is the ability to control the magnetization direction of the tip which can be achieved by evaporating different types of ferromagnetic or antiferromagnetic thin films on nonmagnetic tips. This technique is preferred to the use of bulk magnetic tips since it reduces the magnetic stray fields which can significantly modify the sample magnetization [21].

The ability of STM to identify and address individual nano-objects has been used to measure the conductivity of single molecules absorbed on metal surfaces. While the tip is approached to the molecule of interest at constant bias voltage, the current flowing in the junction can be measured, thereby generating an $I(s)$ curve. Alternatively, $I(V)$ curves can be recorded at different s values. Since tip and substrate act as electrodes, both methods enable information to be obtained about the conductance of the individual molecule embedded in the junction. These measurements are often complemented by IETS experiments in the same configuration. IETS might in fact help to determine the arrangement and the coupling of the junction, which has a significant influence on the electronic and structural properties of the molecule. Single molecule STM conductance experiments represent an important source of information for understanding mechanisms of electron transport in organic molecules with applications in organic electronics and photovoltaics. They complement narrow gap electrode and break junction techniques, having the significant advantage of a highly localized electrode which allows to address and characterize individual molecules.

A similar type of application, although typically not aimed at individual molecules, is at the basis of the four point probe STM, where four STM tips, in addition to imaging, are used for local four point electric conduction measurements. A scanning electron microscope is installed above the STM enabling the positioning of the tips on the contact. The purpose of such very complex instruments is to measure the charge transport through individual nanoelectronic components (in particular self-assembled ones) and to correlate this information with a local high-resolution structural characterization.

Tip-Induced Modification

Besides being an extraordinary instrument for the characterization of structural, electronic, vibrational, optical, and magnetic properties of surfaces with subnanometer resolution, STM has also developed as a tool to modify and nanoengineer matter at the single molecule and atom scale.

By decreasing the distance between the tip and the sample in a controlled way, indentations can be produced in the substrate with lateral sizes down to a few nm. Nanolithography can also be performed by tunneling electrons into a layer of e-beam photoresist (▶ SU-8 Photoresist), thereby reaching a better resolution compared to standard electron beam lithography (EBL). Many other STM-based nanopatterning and nanofabrication techniques have been developed based on a number of physical and chemical principles including anodic oxidation, field evaporation, selective chemical vapor deposition, selective molecular desorption, electron-beam induced effects, and mechanical contact. All these methods exploit the extreme lateral localization of the tunneling current and can be applied in air, liquids and vacuum.

However, the nanotechnological application that gained most attention is the ability to manipulate individual atoms and molecules on a substrate. This is possible due to a controlled use of tip-particle forces and is typically done in UHV and at low temperatures. The first atomic manipulation experiment was performed by Eigler and Schweizer in 1989 [2]. This phenomenal result fulfilled Richard Feynman's prophecy that "ultimately-in the great future-we can arrange the atoms the way we want; the very atoms, all the way down!" [3].

During a lateral manipulation experiment, the tip is first placed above the particle to be moved (for example an atom) and the tunneling current is increased while keeping a constant voltage. This results in a movement of the tip toward the atom, see Eq. 12. If their separation is reduced below 0.5 nm, Van der Waals forces start to come into play together with attractive and repulsive chemical interactions. When these forces equal the diffusion energy barrier, a lateral displacement of the tip can induce a movement of the atom parallel to the surface. After the desired final position is reached, the tip is retracted by reducing the tunneling current to the initial value, leaving the atom in the selected place. Depending on the tip-particle distance and therefore on the strength and nature of the interaction, different manipulation modes including pulling, pushing, and sliding [22] were identified and used to move different types of atoms and molecules.

Thanks to this technique, it was possible to fabricate artificial nanostructures such as the *quantum corral* [23] and to probe quantum mechanical effects like the quantum confinement of surface state electrons or the *quantum mirage*. Lateral STM manipulation has also been used to switch between different adsorption configurations and conformations of molecules on surfaces and to modify their electronic properties in a controlled way [24].

A further application of STM manipulation is the synthesis of new molecular species based on the ability of STM to form and break chemical bonds with atomic precision. Reactants are brought close together on the surface and the actual reaction is realized by applying a voltage pulse or by exciting vibrational modes through inelastically tunneling electrons. Examples of this technique include the dissociation of diatomic molecules, the Ullmann reaction, the isomerization of dichlorobenzene and the creation of metal-ligand complexes.

The STM tip has also been used to perform vertical manipulations of nanoparticles where an atom (or molecule) is deliberately transfered from the surface to the tip and vice versa by using the electric field generated by the bias voltage. In contrast to the lateral manipulation, here the bonds between the surface and the atom are broken and re-created [25]. By approaching the tip at distances of a few Å from the chosen particle chemical interactions are established that reduce the atom-surface binding energy. If a voltage pulse is applied under these conditions, the resulting electric field (of the order of 10^8 V/cm) can be enough to induce the particle desorption. The vertical manipulation technique has also been used as a means to increase the lateral resolution of STM. In fact, the controlled adsorption of a specific molecule onto the tip often makes it "sharper" and can add a chemical resolution capability if the DOS of the extra molecule acts as an "energy filter."

A related effect is exploited in the recently proposed scanning tunneling hydrogen microscopy (STHM) technique. In STHM, the experimental chamber is flooded with molecular hydrogen while the tip is scanned in constant height mode at very close distances over the surface. H_2 can get trapped in the tip-sample junction and its rearrangement during scanning of the surface generates a new contrast mechanism based on the short-range Pauli repulsion. This is extremely sensitive to the total electron density, thereby endowing the STM with similar imaging capabilities to non-contact AFM (▶ AFM, Non-contact Mode) and making it able to resolve the inner structure of complex organic molecules [26].

Acknowledgments This work was supported by EPSRC (EP/D000165/1); A. Della Pia was funded through a WPRS scholarship of the University of Warwick. J. V. Macpherson, T. White, and B. Moreton are gratefully thanked for their critical reading of the manuscript.

Cross-References

- ▶ AFM, Non-contact Mode
- ▶ Atomic Force Microscopy
- ▶ Electrochemical Scanning Tunneling Microscopy
- ▶ Electron Beam Lithography (EBL)
- ▶ Piezoresistivity
- ▶ Scanning Electron Microscopy
- ▶ Scanning Tunneling Microscopy
- ▶ SU-8 Photoresist
- ▶ Transmission Electron Microscopy

References

1. Binnig, G., Rohrer, H., Gerber, C., Weibel, E.: Surface studies by scanning tunneling microscopy. Phys. Rev. Lett. **49**, 57 (1982)

2. Eigler, D.M., Schweizer, E.K.: Positioning single atoms with a scanning tunneling microscope. Nature **344**, 524 (1990)
3. Feynman, R.P.: There's plenty of room at the bottom: an invitation to enter a new field of physics. Engineering and Science. **23**, 22 (1960)
4. Bardeen, J.: Tunneling from a many-particle point of view. Phys. Rev. Lett. **6**, 57 (1961)
5. Gottlieb, A.D., Wesoloski, L.: Bardeen's tunnelling theory as applied to scanning tunnelling microscopy: a technical guide to the traditional interpretation. Nanotech. **17**, R57 (2006)
6. Lang, N.D.: Spectroscopy of single atoms in the scanning tunneling microscope. Phys. Rev. B **34**, 5947 (1986)
7. Landau, L.D., Lifshitz, E.M.: Quantum mechanics: non-relativistic theory. Pergamon Press, Oxford, (1977)
8. Chen, C.J.: Introduction to scanning tunneling microscopy. Oxford University Press, Oxford (2008)
9. Binnig, G., Rohrer, H.: Scanning tunneling microscope. Helv. Phys. Acta **55**, 726 (1982)
10. Okumura, A., Miyamura, K., Gohshi, Y.: The STM system constructed for analytical application. J. Microsc. **152**, 631 (1988)
11. Besocke, K.: An easily operable scanning tunneling microscope. Surf. Sci. **181**, 145 (1987)
12. Pan, S.H., Hudson, E.W., Davis, J.C.: ^{3}He refrigerator based very low temperature scanning tunneling microscope. Rev. Sci. Instrum. **70**, 1459 (1999)
13. Laegsgaard, E., et al.: A high-pressure scanning tunneling microscope. Rev. Sci. Instrum. **72**, 3537 (2001)
14. Repp, J., Meyer, G., Stojkovic, S.M., Gourdon, A., Joachim, C.: Molecules on insulating films: scanning-tunneling microscopy imaging of individual molecular orbitals. Phys. Rev. Lett. **94**, 026803 (2005)
15. Sainoo, Y., et al.: Excitation of molecular vibrational modes with inelastic scanning tunneling microscopy processes: examination through action spectra of cis-2-butene on Pd(110). Phys. Rev. Lett. **95**, 246102 (2005)
16. Gimzewski, J.K., Reihl, B., Coombs, J.H., Schlittler, R.R.: Photon emission with the scanning tunneling microscope. Z. Phys. B:Condens. Matter **72**, 497 (1988)
17. Davis, J.J.: Molecular bioelectronics. Philos. Trans. Roy. Soc. A **361**, 2807 (2003)
18. Feenstra, R.M.: Cross-sectional scanning-tunneling-microscopy of III-V semiconductor structures. Semicond. Sci. Technol. **9**, 2157 (1994)
19. Rost, M.J., et al.: Scanning probe microscopes go video rate and beyond. Rev. Sci. Instrum. **76**, 053710 (2005)
20. Petersen, L., et al.: A fast-scanning, low- and variable-temperature scanning tunneling microscope. Rev. Sci. Instrum. **72**, 1438 (2001)
21. Wiesendanger, R.: Spin mapping at the nanoscale and atomic scale. Rev. Mod. Phys. **81**, 1495 (2009)
22. Bartels, L., et al.: Dynamics of electron-induced manipulation of individual CO molecules on Cu(111). Phys. Rev. Lett. **80**, 2004 (1998)
23. Crommie, M.F., Lutz, C.P., Eigler, D.M.: Confinement of electrons to quantum corrals on a metal-surface. Science **262**, 218 (1993)
24. Moresco, F., et al.: Conformational changes of single molecules induced by scanning tunneling microscopy manipulation: a route to molecular switching. Phys. Rev. Lett. **86**, 672 (2001)
25. Avouris, P.: Manipulation of matter at the atomic and molecular-levels. Acc. Chem. Res. **28**, 95 (1995)
26. Weiss, C., et al.: Imaging Pauli repulsion in scanning tunneling microscopy. Phys. Rev. Lett. **105**, 086103 (2010)

Scanning Tunneling Spectroscopy

Amadeo L. Vázquez de Parga and Rodolfo Miranda
Dep. Física de la Materia Condensada, Universidad Autónoma de Madrid and Instituto Madrileño de Estudios Avanzados en Nanociencia (IMDEA-Nanociencia), Madrid, Spain

Definition

Scanning tunneling spectroscopy (STS) is a technique that allows the study of the electronic structure of surfaces with atomic resolution.

Overview

Scanning tunneling microscopy (STM) was historically the second technique that could image individual atoms one by one. It was invented in 1981–1982 by Gerd Binnig and Heindrich Rohrer [1], long after the technique of field ion microscopy (FIM) developed in 1951 by Erwin Müller [2].

In STM a sharp tip probes the surface of interest by allowing electrons to tunnel quantum-mechanically between the tip and the surface. Because such tunneling is extremely sensitive to the distance between tip and surface, one gets high resolution perpendicular to the surface. Assuming a constant density of states on the surface, when the STM tip is scanned over the sample surface while keeping the tunneling current constant, the tip movement depicts the surface topography, because the separation between the tip apex and the sample surface is always constant. It is worth noting that STM not only converts the spatial change in the tunneling current into a highly detailed topographic image of surfaces with constant density of states, but also the tunneling current changes with the available surface electronic states. This dependence of the tunneling current on the surface electronic structure together with the high spatial resolution of STM allows us to study the electronic structure of the

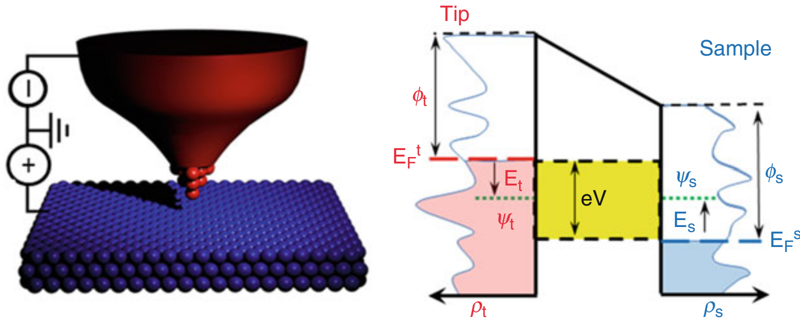

Scanning Tunneling Spectroscopy, Fig. 1 *Left panel*: Configuration of a positively biased tunnel junction in a STM. The bias voltage is applied to the sample and the tunneling current is measured on the tip. *Right panel*: Energy diagram of an STM tunnel junction. In this diagram the vertical axis represents energy and the horizontal axes distance between tip and sample and density of states. E_t, Ψ_t and E_s, Ψ_s are the energy and wave function of the states of the electrode tip and sample respectively. ϕ_t, ϕ_s, E_F^t, E_F^s, ρ_t, ρ_s are the work functions, Fermi energies and densities of states (DOS) of electrode tip and sample, respectively, and V is the voltage applied to electrode sample

surfaces with atomic resolution. The technique is known as scanning tunneling spectroscopy (STS).

Scanning Tunneling Spectroscopy Theory

Most theoretical treatments applied today to describe the tunneling process in an STM start from the formalism of the transfer Hamiltonian developed by Bardeen in 1961 [3] for the study of superconducting tunnel junctions. In this approach, the electronic structure and electron wave functions of both electrodes are calculated assuming no interaction between them and afterward the tunneling current is calculated [3]. Figure 1a shows the scheme of the tunnel junction in a STM where one of the electrodes is a tip. Figure 1b shows the energy diagram of the tunnel junction. In this diagram the vertical axis represents energy. E_t and Ψ_t are the energy and wave function of the states of the electrode "tip" in the absence of electrode "sample." E_s and Ψ_s are the energy and wave function of the states of the electrode "sample" in the absence of electrode "tip." ϕ_t, ϕ_s, $E_F{}^t$, $E_F{}^s$, ρ_t, ρ_s are the work functions, Fermi energies, and densities of states (DOS) of electrode "tip" and "sample," respectively, and V is the voltage applied to electrode "sample." When the distance between the electrodes is small enough, the overlap between their wave functions is significant and the probability of electron transfer between the two electrodes by tunneling starts to be noticeable. In the absence of applied voltage, the Fermi levels of the two electrodes are aligned and no net tunneling current flows. However, by applying a voltage V the Fermi levels move with respect to each other opening an energy window, eV, where electrons from one electrode can tunnel to the empty states of the other and, thus, the tunneling current starts to flow.

In 1983, Tersoff and Hamann applied the Bardeen's formalism to the STM, replacing one of the electrodes by a point [4, 5, 6]. The tip was shaped like an s orbital centered at the tip position and the calculated tunneling matrix elements proved to be proportional to the amplitude of the wave functions of the sample at the position of the tip. If the distance between tip and sample is not very large (few ångstroms), the bias voltage small and the temperature low, the tunneling current can be written as follows:

$$I \propto \int_o^{eV} \rho_s(\vec{r}_s, E)\rho_t(\vec{r}_s, E - eV)T(E, eV, d, \phi)dE \quad (1)$$

where $\vec{r}_s$ is the tip position over the sample surface, d is the distance between tip and sample, and T is the transmission probability that depends on the energy of the states involved, the bias voltage applied between tip and sample, the distance between tip and sample, and the tunneling barrier height, which is related with the tip and surface work functions. This equation indicates that the tunneling process depends, for a given energy, on three interconnected parameters, i.e., the tunneling current I, the bias voltage V, and the tip sample separation d. Almost all attempts to explore these complex dependences of the tunneling current (and simultaneously extend the performance of STM)

have been demonstrated by the late 1980s [7]. Scanning tunneling spectroscopy measures the relation between any two of while keeping fixed the third one. This gives three modes of spectroscopy measurements: (1) I-V curves, where the variation of the tunneling current with the bias voltage is measured for a fixed distance between tip and sample, (2) I-z curves, where the variation of the tunneling current with the distance between tip and sample is measured for a fixed bias voltage V, and (3) V-z curves, where the variations in the tip sample distance are measured as function of the bias voltage for a fixed tunneling current.

In these three modes energy conservation for the tunneling electrons is assumed. If electrons change their energy during the tunneling process by an inelastic process, the inelastic electron tunneling spectroscopy (IETS) mode is possible. Finally, if the STM tip and the sample are magnetic, the tunneling current depends on the relative orientation of the magnetization of both tip and sample. This mode is called spin polarized scanning tunneling microscope (SP-STM) and allows the study of magnetic properties with atomic resolution. In the following the five modes will be discuss in detail.

Scanning Tunneling Spectroscopy Modes

I-V Curves

I-V measurements are the most widely used spectroscopic technique in STM experiments. If the tunneling current (Eq. 1) is differentiated with respect to the bias voltage the following expression is obtained:

$$\frac{dI}{dV} \propto \rho_t(0)\rho_s(eV)T(eV, eV, d, \phi) + \int_0^{eV} \rho_t(E - eV)\rho_s(E)\frac{dT(E, eV, d, \phi)}{dV}dE + \int_0^{eV} \rho_s(E)\frac{d\rho_t(E - eV)}{dV}T(E, eV, d, \phi)dE$$

Assuming a constant density of states for the tip, the third term is zero, but, it should be mentioned that, often, the tip electronic states have a strong influence in the STS spectra [8]. Another common simplification is to assume that the transmission coefficients are constant in the voltage range explored in the measurement. Then the second term also vanishes and the expression becomes:

$$\frac{dI}{dV} \propto \rho_t(0)\rho_s(eV)T(eV, eV, d, \phi)$$

In general the experimentally determined differential tunneling conductance is widely accepted as a good approximation to the DOS of the surface (modulated by the specific transmission of the barrier) at an energy value of eV, with V being the bias voltage applied between tip and sample.

Figure 2 shows an STS experiment performed on the Cu(111) surface in which the transmission probability (see Eq. 1) can be seen to depend on the energy parallel to the surface. Figure 2a shows the bulk band projection of Cu(111) along the $\overline{\Gamma \mathrm{M}}$ direction of the surface Brillouin zone. Bulk bands are represented in gray and the projectional bandgap in white. The gray line corresponds to the dispersion relation of Shockley surface state of Cu(111). The surface state can be seen as a two-dimensional electron gas with the bottom of the band at −0.44 eV and an effective mass $m^* = 0.42$ m_e. Therefore, disregarding any contribution from the bulk electronic structure, the LDOS expected around the Fermi level of Cu(111) is a step function centered at the bottom of the band. This step function is shown in Fig. 2b. Figure 2c shows an STS spectrum taken on the Cu(111) surface. The experimental data correspond to the dots. The spectrum has a peak at −0.38 eV superimposed on a background which decays with increasing energy. The bottom of the surface state band corresponds to the point halfway up the peak (dashed line in Fig. 2c). The line in the graphic is a fit to the background that reflects the contribution of the bulk states. As the bias voltage approaches the Fermi level from below, the $k_{||}$ of the accessible bulk states increases, so that they present a smaller effective perpendicular energy which means a smaller transmission probability and, thus, they contribute less to the spectrum. On the other hand, the peak at −0.38 eV corresponds to the sharp increase in the LDOS associated to the bottom of the surface state, superimposed on the background due to the bulk bands. Although the LDOS of a 2D is a step function to a constant value, the peak in the spectrum instead of staying constant for energies higher than the bottom of the band (−0.44 eV), decreases with increasing energy. This reduction in the signal with energy reflects the dispersion of the surface state, i.e., the fact that the $k_{||}$ of the surface state increases also when the energy increases. Accordingly, the transmission probability (and the signal in the spectrum) gets smaller.

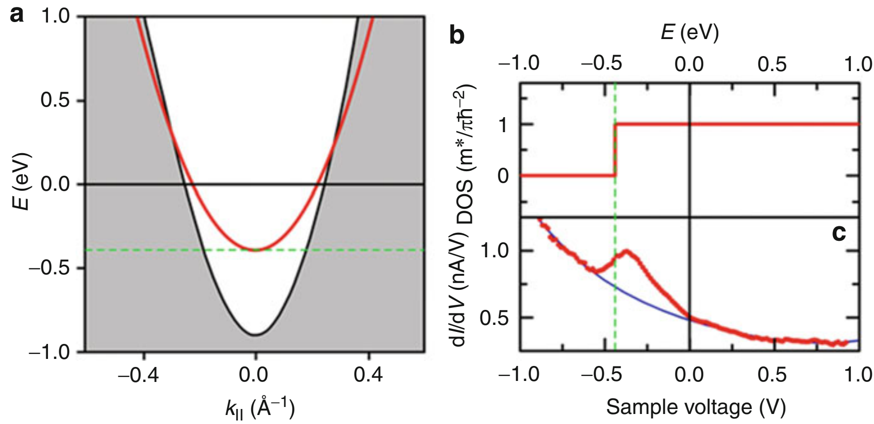

Scanning Tunneling Spectroscopy, Fig. 2 (**a**) Shows the bulk band projection of Cu(111) along the $\overline{\Gamma M}$ direction of the surface Brillouin zone. Bulk bands are represented in *gray*, and in *white* the projectional bandgap. The *gray line* corresponds to the dispersion relation of surface state of Cu(111). (**b**) Expected density of states for a two-dimensional electron gas. (**c**) An STS spectrum taken on the surface Cu(111). The experimental data correspond to the dots

Experimentally in order to record I-V curves, the distance between tip and sample has to be kept constant during the measurement time. This can be done in different ways. In one of them the tip is placed at a desired position on the surface and at the desired distance from the surface. The distance between tip and sample is dictated by the values of the tunneling current and the bias voltage used in the topographic image. The feedback circuit, that keeps the tunneling current constant adjusting the tip sample distance, is disconnected and then the voltage V is ramped and the tunneling current is recorded over the desired bias voltage range. The dI/dV values are obtained by numerical differentiation of the I-V curves. If the measurement is repeated in every pixel of a topographic image, the method is called *current imaging tunneling spectroscopy* (CITS) and provides with a map of the spatial distribution of the LDOS on the surface.

Another method is to detect directly the dI/dV signal using a lock-in amplifier. In order to do that, a small high-frequency sinusoidal signal, $V_{mod}\ \sin(\omega t)$, is superimposed on the bias voltage between tip and sample. The modulation causes a sinusoidal response in the tunneling current and the amplitude of the modulated current is sensitive to dI/dV. For a small applied sinusoidal signal, the modulated current can be Fourier decomposed on the applied modulation frequency ω:

$$I(V_{\text{bias}}, t) = I(V_{\text{bias}}) + \frac{dI(V_{\text{bias}})}{dV} V_{\text{mod}} \sin(\omega t) + \frac{d^2 I(V_{\text{bias}})}{dV^2} \frac{V_{\text{mod}}^2}{4} \sin(2\omega t) + \cdots \quad (2)$$

The first harmonic, which is proportional to the differential conductance (dI/dV), can be extracted by means of lock-in detection and the spatial variation of the dI/dV signal can be mapped in certain area of the surface. During a constant current topographic image, the dI/dV signal is simultaneously recorded in each point of the image at a certain bias voltage. The result is a map that reflects the LDOS of a surface area at a defined energy eV. Since the feedback loop is connected during the topographic image, the frequency of the modulated signal needs to be higher than the cutoff frequency of the feedback loop response in order to keep the tip distance constant during the acquisition of the data.

I-Z Curves

In the simplest theoretical treatment of the tunneling process for a metal-vacuum-metal tunnel junction [7] where the bias voltage is much smaller than the work function (assumed to be the same for both metals), the problem is reduced to a square potential barrier as shown in Fig. 3. The wave function that describes an electron in the tunneling barrier is given by:

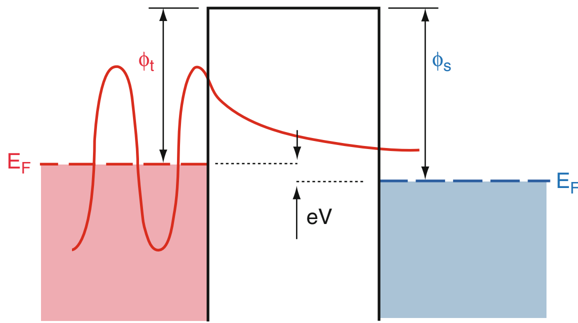

Scanning Tunneling Spectroscopy, Fig. 3 One dimensional metal-vacuum-metal tunnel junction. Both the sample, in *red*, and the tip, in *blue*, are modeled as semi-infinite pieces of free electron metals. The tunneling probability depends on the exponential decay of the electrons wave function into the vacuum barrier. The bias voltage is small enough to consider a square barrier

$$\psi(z) = \psi(0)e^{-\kappa z}$$

where

$$\kappa = \frac{\sqrt{2m(\phi)}}{\hbar}$$

is the decay constant that describes the probability of finding the electron along the +z direction and depends on the surface work function (Φ). The tunneling probability for a given distance, d, between tip and sample is:

$$P \propto |\psi(0)|^2 e^{-2\kappa d}$$

and the tunneling current is proportional to the number of occupied states available in the energy interval defined by the bias voltage applied between tip and sample, and therefore the tunneling current can be written as follows:

$$I \propto \sum_{E_n=E_F-eV}^{E_F} |\psi_n(0)|^2 e^{-2\kappa d}$$

If the bias voltage is small enough to consider the density of states constant, the equation can be written in terms of the Local Density of States (LDOS) at the Fermi level. At a position d and energy E, the LDOS of the sample can be expressed as:

$$\rho_s(d,E) \equiv \frac{1}{\varepsilon} \sum_{E_n=E-\varepsilon}^{E} |\psi_n|^2$$

for small enough ε. The tunneling current in terms of the surface LDOS at the Fermi level is:

$$I \propto V\rho_s(0,E_F)e^{-2\kappa d}$$

Assuming a typical value of 4 eV for the work function, $\kappa = 1.025$ Å^{-1}. From the expression above, the dependence of the logarithm of the tunneling current with respect to distance is a measure of the work function, or more precisely, of the tunneling barrier height. The corresponding expression is:

$$\phi \approx 0.95\left(\frac{d\ln I}{dz}\right)^2$$

The measurement of the apparent barrier height can be carried out by approaching or retracting the tip from the sample and recording the tunneling current. In order to measure the spatial change in apparent barrier height, a small modulation in the separation between the tip and the sample is introduced at high frequency and the modulated tunneling current is measured using a lock-in amplifier. This type of measurement gives the apparent barrier height at certain bias voltage and at certain distance from the surface. Measurements performed with different bias voltages or different tip sample distance may give different values for the apparent barrier height [7]. It is important to realize that the apparent barrier height is different from the work function in traditional surface science but is closely related; the apparent barrier height measures the spatial correlation of the overlap between the wave functions of the tip and the sample.

Z-V Curves

In Z-V measurements the bias voltage is ramped at a fixed tunneling current, and the tip-sample separation is constantly adjusted. When the applied voltage exceeds the sample or tip work function (depending on the sign of the bias voltage), there is a transition from the vacuum tunneling regime to the field emission regime. In the field emission regime, a triangular potential well is formed between tip and sample due to the bias voltage applied in the tunneling junction. In this triangular potential well, the existence of quantum well states leads to resonances in the electron transmission at certain energies, as illustrated in Fig. 4.

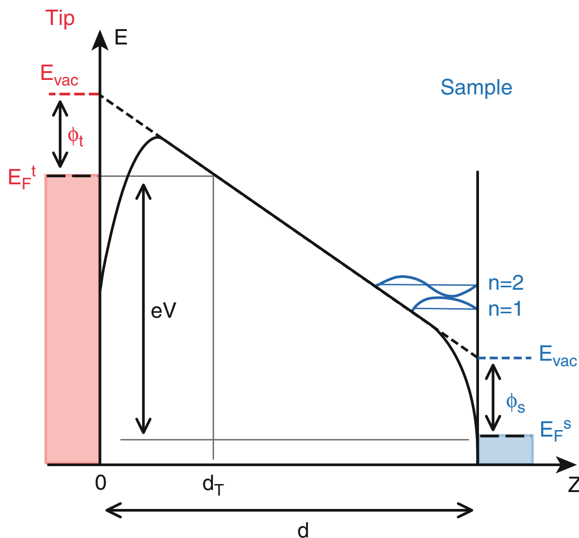

Scanning Tunneling Spectroscopy, Fig. 4 Diagram of the tunnel junction when the positive bias voltage (eV) is larger than the work function of the sample. The electrons from the tip tunnel through a narrow (d_T) triangular potential barrier to be afterward trapped in a triangular potential well. The first two quantum well states are shown

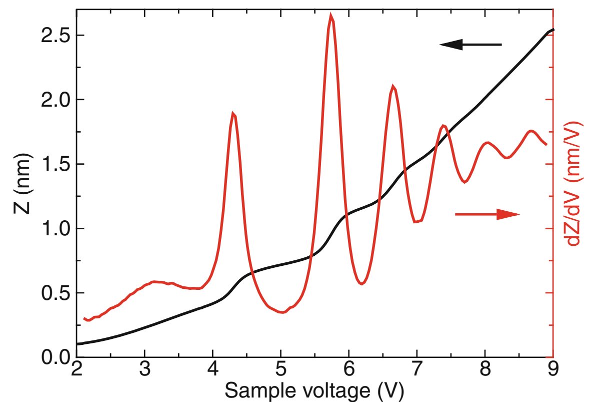

Scanning Tunneling Spectroscopy, Fig. 5 *Black curve*, tip displacement as function of the tunneling bias voltage. The field emission resonances appear as wiggles on the curve. *Gray curve*, dZ/dV, the field emission resonances appear as well-defined peaks that allow a precise determination of the energy

These transmission resonances show up as wiggles in the Z-V data (black curve in Fig. 5) and are closely related to the image states. Image states are unoccupied states bound by the classical image-charge response of metallic surfaces and have a free-electron-like dispersion parallel to the surface. The inverse dependence on distance from the surface of the image potential leads to a Rydberg-like series of states that converges to the continuum at the vacuum level (E_{vac}). Inverse photoemission studies of the image potential states have shown experimentally that the energy position of the Rydberg series is tied to the local surface potential of the material. In STM the electric field across the tunnel junction causes a Stark shift of these states, expanding the image state spectrum into a resonance spectrum associated with the triangular potential well (Fig. 5). Following the analysis performed by Gundlach in the 1960s [9], the resulting energy spectrum can be written as follows:

$$E_n = \phi + \alpha(n - 0.25)^{2/3} F^{2/3}$$

where ϕ is the surface work function, α is a constant, F is the electric field between tip and sample, and n is the quantum number of the states. These field emission resonances (FERs) were experimentally observed in field ion microscopy (FIM) by Jason [10] and with an STM by Binnig et al. [11] and since then have been used to chemically identify different transition metals on surfaces, to obtain atomic resolution on insulating surfaces (e.g., diamond), or to study local changes in the surface work function [12].

The experiments are typically performed with the feedback loop on to keep the current constant. The tip movement is recorded as a function of the bias voltage and afterward the curves are numerically differentiated to obtain the energy position of the field emission resonances, as shown in the Fig. 5 (red curve).

Spin Polarized Tunneling Spectroscopy

In 1975 Julliére [13] discovered spin-dependent tunneling between two planar ferromagnetic electrodes separated by an insulating tunnel barrier, which has become the basis for the development of magnetic random access memories and the spin polarized version of the STM. In fact, the tunneling current between a magnetic sample and an STM tip (covered with a magnetic thin film) shows an asymmetry in the spin population. The magnitude of the tunneling conductance between two magnetic electrodes with directions of the respective magnetization differing by a certain angle depends on the cosine of this angle. Spin polarized tunneling with an STM was observed in 1990s by Wiesendanger [16]. The spectroscopic mode of spin polarized STM is based on using the different intensity of certain features in differential

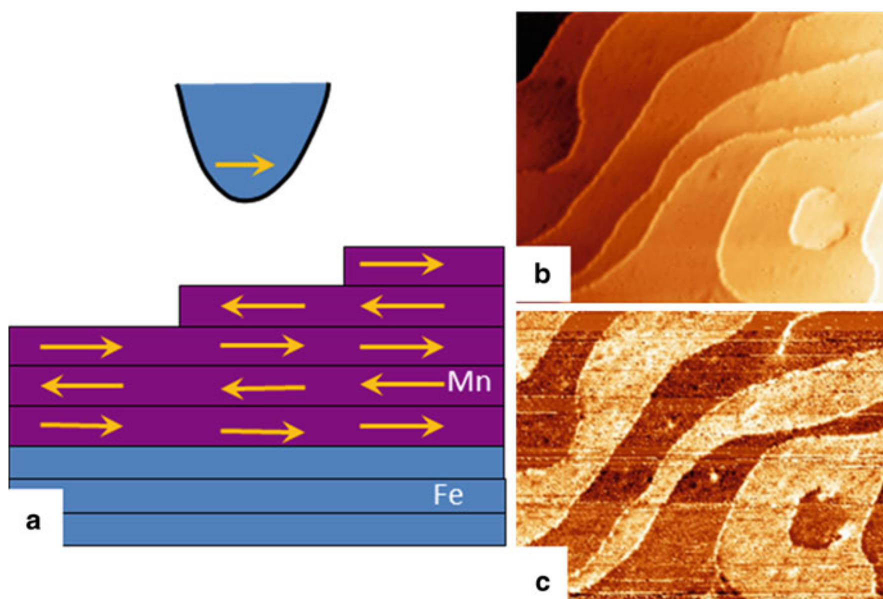

Scanning Tunneling Spectroscopy, Fig. 6 (**a**) Model showing the layered antiferromagnetic structure of Mn films grown on Fe(001). (**b**) STM topographic (100 × 78 nm) image of 6.5 mL of Mn grown on Fe(001). (**c**) Spatially resolved spectroscopic image measured simultaneously with the topography shown in (**b**) where the dI/dV signal shows low and high levels depending on the relative directions of magnetization of tip and surface terrace revealing the topological antiferromagnetic order of the Mn(001) surface

conductance spectra as source of contrast to image magnetic domains and domain walls with atomic resolution [16].

Magnetic domain observations in antiferromagnetic materials have been difficult in the past due to the limited number of experimental techniques that are sensitive to domain states in antiferromagnetic crystals. Another aspect that hampered the studies of antiferromagnetic materials was the limited spatial resolution of the available techniques. Mn and Cr crystals or thin films of these materials exhibit quite complex spin structures. The crystallographic structure of Mn thin films grown on Fe(001) is body-centered tetragonal. In this crystallographic structure, the Mn magnetic structure is layered antiferromagnetic. These means that the magnetization orientation rotates by 180° in every layer, as can be seen in Fig. 6a. The tip magnetization direction is constant in the experiment and the magnetization direction of the sample rotates by 180° every time the tip crosses a step on the surface. The change in the magnitude of the tunneling conductance can be measured on every pixel of the topographic image and an image of the magnetic domains is obtained, as can be seen in Fig. 6b, c. In those domains where the magnetization of tip and sample are aligned, the tunneling conductance is higher (brighter color) and on those areas where are antiparallel the tunneling conductance is lower (darker colors).

Vibrational Spectroscopy (Inelastic Electron Tunneling Spectroscopy)

In the previous sections, elastic tunnel processes, where the tunneling electrons do not change their energy, have been discussed. However, in certain cases, i.e., for molecules adsorbed on surfaces or samples with easy excitation of phonons, there is a small fraction of electrons that lose energy in the tunneling process [14]. For bias voltages larger than corresponding the quantum of vibration, $\hbar\omega$, a new tunneling channel, i.e., inelastic channel, opens up (as illustrated in Fig. 7a). The inelastic channel acts in addition to the elastic channel, and increases slightly the differential conductance (dI/dV) of the junction (Fig. 7b upper panel). Although vibrations of molecules were detected in the 1960s by tunneling in extended tunneling junctions with insulating layers spray coated with molecules, the use of STM facilitates the acquisition of vibrational spectra in single molecules in well-characterized environments and was pioneered by Wilson Ho [14].

In practice the change in conductance is smaller than 10% and can be detected only under very severe conditions of stability of the tunnel junction and energy resolution (i.e., with the STM at low temperatures). The vibrational modes are detected as peaks in the second derivative of the tunneling current (Fig. 7b lower panel) measured by means of lock-in techniques. Equation 2 shows that the magnitude of the second

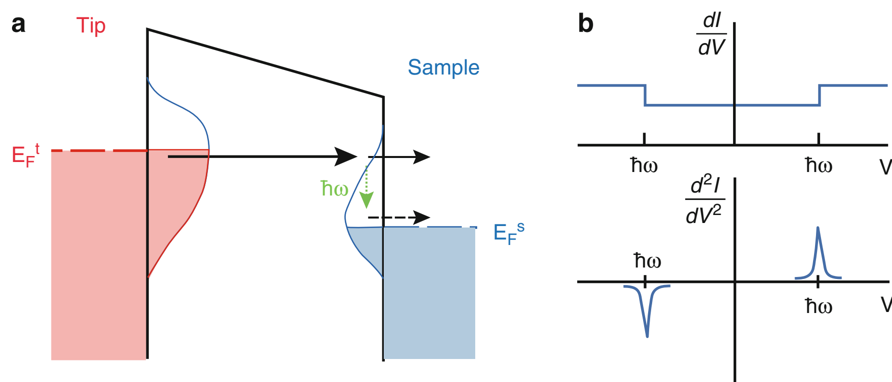

Scanning Tunneling Spectroscopy, Fig. 7 (**a**) Energy distance diagram of the tunneling processes with an applied bias voltage V. When eV is larger than the energy of the molecular vibration (ħω), empty final states at the Fermi level of the sample become accessible and the inelastic channel opens up. (**b**) The opening of the inelastic channel causes a sharp increase in the tunneling conductance (*upper panel*) or peaks in the second derivative (*lower panel*). The activation channel is symmetric with respect to the Fermi level

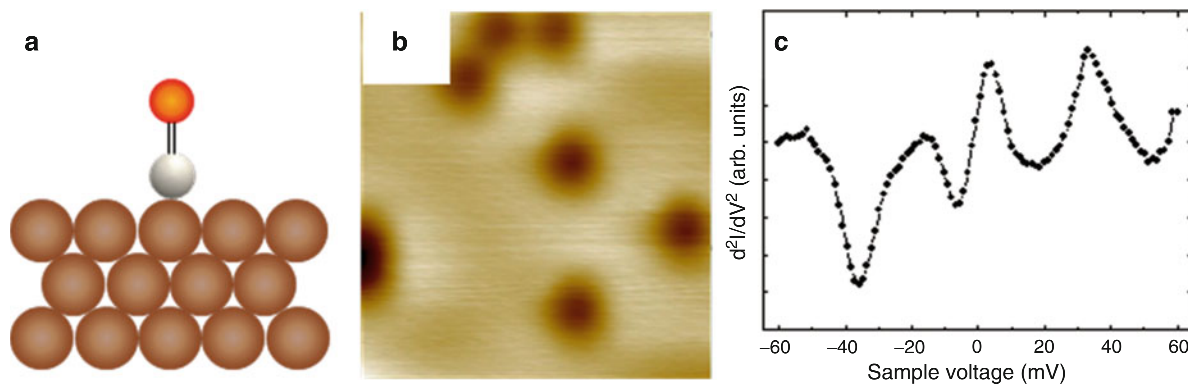

Scanning Tunneling Spectroscopy, Fig. 8 (**a**) Model of the adsorption of CO molecules on Cu(111). The molecule adsorbs perpendicular to the surface with the carbon (in *gray*) chemically bonded to the surface copper atoms. (**b**) STM topographic image measured using a tunneling current of 1 nA and a sample bias voltage of 0.25 V. (**c**) Vibrational spectra of CO on Cu(111): the peaks at ±5 mV and ±35 mV are due to excitation of the CO frustrated rotation and translation with respect to the Cu(111) surface

harmonic of the tunneling current is proportional to d^2I/dV^2. In practice, a small (≈3 mV) ac component is added to the bias voltage, the dc component of the bias voltage is scanned across the selected energy range, and the variations in d^2I/dV^2 are recorded. The width of the peaks is given by the Fermi energy distribution, i.e., the FWHM is $3.5k_BT$ (1.2 mV at 4 K).

A common observation in IETS spectra is that peaks at certain values of positive voltages appear as *dips* at opposite polarity. The symmetry position with respect to the zero bias of the features observed is a fingerprint of their inelastic origin. Differences in the density of states of the electrodes, however, may change the peak intensity. The observed symmetry implies that the inelastic processes are accessible for electrons tunneling on both directions. Selection rules for which modes are detectable, unlike Raman or infrared spectroscopy, seems to depend on the symmetry of the molecular state involved in the tunneling process.

A well-studied system are CO molecules adsorbed on Cu(111). It is known that the CO molecules adsorb on the surface on top of the copper atoms with the oxygen pointing toward the vacuum and the carbon chemically bonded to the copper surface, as shown in Fig. 8a. Figure 8b shows a topographic STM image of

several CO molecules adsorbed on Cu(111) at 4.6 K measured with a tunneling current of 1 nA and a bias voltage of −0.25 V. With these values the CO molecules are imaged as a round depression because the chemical bond between the molecule and the Cu(111) surface reduces the electron density around the Fermi level. In order to measure the vibrational spectra, the tip is positioned over the center of the CO molecule. With the feedback off, the sample bias voltage is ramped over the range of the vibrational peaks while a sinusoidal bias modulation is superimposed. The derivative of the conductance exhibits peaks at the molecular vibration energy. For CO on Cu(111) the vibration spectra are characterized by two features at about 5 and 35 meV, as can be seen in Fig. 8c. These peaks are assigned to the two degenerated transverse vibration modes: the frustrated translation and the frustrated rotation, respectively.

Cross-References

▶ AFM
▶ Field Electron Emission from Nanomaterials
▶ Scanning Tunneling Microscopy
▶ Surface Electronic Structure

References

1. Binnig, G., Rohrer, H.: Scanning tunneling microscopy. Helv. Phys. Acta **55**, 726 (1982)
2. Müller, E.W.: Das Feldionenmikroskop. Z. Physik **31**, 136 (1951)
3. Bardeen, J.: Tunneling from many particle point of view. Phys. Rev. Lett. **6**, 57 (1961)
4. Tersoff, J., Hamann, D.R.: Theory and application for the scanning tunneling microscope. Phys. Rev. Lett. **50**, 1998 (1983)
5. Tersoff, J., Hamann, D.R.: Theory of the Scanning tunneling microscope. Phys. Rev. B **31**, 805 (1985)
6. Lang, N.D.: Spectroscopy of single atoms in the Scanning tunneling microscope. Phys. Rev. B **34**, 5947 (1986)
7. Chen, C.J.: Introduction to Scanning Tunneling Microscopy. Oxford University Press, New York (1993)
8. Vázquez de Parga, A.L., Hernán, O.S., Miranda, R., Levi Yeyati, A., Mingo, N., Martín-Rodero, A., Flores, F.: Electron resonances in sharp tips and their role in tunneling spectroscopy. Phys. Rev. Lett. **80**, 357 (1998)
9. Gundlach, K.H.: Zu berechnung des tunnelstroms durch eine trapezförmige potentialstufe. Solid State Electron. **9**, 949 (1966)
10. Jason, A.J.: Field induced resonance states at a surface. Phys. Rev **156**, 266 (1966)
11. Binnig, G., Frank, K.H., Fuchs, H., Garcia, N., Reihl, B., Rohrer, H., Salvan, F., Williams, A.R.: Tunneling spectroscopy and inverse photoemission: image and field states. Phys. Rev. Lett. **55**, 991 (1985)
12. Borca, B., Barja, S., Garnica, M., Sánchez-Portal, D., Silkin, V.M., Chulkov, E.V., Hermanns, C.F., Hinarejos, J.-J., Vázquez de Parga, A.L., Arnau, A., Echenique, P.M., Miranda, R.: Potential energy landscape for hot electrons in periodically nanostructured graphene. Phys. Rev. Lett. **105**, 036804 (2010)
13. Person, B.N.J., Baratoff, A.: Inelastic electron tunneling from a metal tip: the contribution from resonant processes. Phys. Rev. Lett. **59**, 339 (1987)
14. Stipe, B.C., Rezaei, M.A., Ho, W.: Single molecule vibrational spectroscopy and microscopy. Science **280**, 1732 (1998)
15. Julliere, M.: Tunneling between ferromagnetic films. Phys. Lett. **54A**, 225 (1971)
16. Wiesendanger, R.: Soin mapping at the nanoscale and atomic scale. Rev. Modern Phys. **81**, 1495 (2009)

Scanning X-Ray Diffraction Microscopy (SXDM)

▶ Selected Synchrotron Radiation Techniques

Scanning-Probe Lithography

▶ Dip-Pen Nanolithography

Scincus officinalis

▶ Friction-Reducing Sandfish Skin

Scincus scincus

▶ Friction-Reducing Sandfish Skin

Scrolled Nanostructure

▶ Nanorobotics for NEMS Using Helical Nanostructures